# Charging strategy considering subzero temperature based on electrochemical-thermal life model for lithium-ion batteries

by

Minseok Song

A dissertation submitted to the Graduate Faculty of
Auburn University
in partial fulfillment of the
requirements for the Degree of
Doctor of Philosophy

Auburn, Alabama
December 11, 2021

Keywords: Cold start, lithium-ion battery, thermal behavior, electrochemical-thermal life model, experimental characterization.

Approved by

Song-Yul Choe, Chair, Professor of Mechanical Engineering
Jeffrey Fergus, Professor of Materials Engineering
Roy W. Knight, Associate Professor of Mechanical Engineering
Robert Dean, Professor of Electrical Engineering

# Abstract

In order to overcome range anxiety of electric vehicles (EVs) powered by lithium-ion batteries, more batteries are installed to increase battery capacity, which results in a long charging time that is one of the most challenging issues for EVs to be commercialized. The charging time can be reduced simply by increasing current rates, which can adversely accelerate battery degradation. Especially at low temperatures, fast charging leads to rapid degradation due to reduced ionic diffusivity and increased charge transfer resistance. Therefore, design of a charging strategy considering operating temperature for lithium-ion batteries is one of the most important issues that affect the overall performance of the batteries.

In the first part of the dissertation, a charging algorithm considering degradation is designed for room temperature. For the algorithm, an accurate reduced-order electrochemical model (ROM) considering side reaction, lithium plating, and lithium stripping is developed and experimentally validated. Afterward, the charging algorithm is designed, and the cycling results by the algorithm are further compared with those by normal charging methods, which has shown that the battery can be charged faster with less degradation using the proposed charging algorithm. However, this charging algorithm does not consider any effect of the battery heat generation and temperature.

Accordingly, a thermal model based on the ROM is developed as the second part of this dissertation. For the accurate estimation of the battery heat generation rate during operations, the detailed heat source terms considering internal processes inside the battery are mathematically formulated. The model is further validated with respect to measured heat generation rate profiles under a wide range of current rates and temperatures. In addition, further detailed analysis for heat source terms, including parameter sensitivity analysis, is conducted. The analysis results have shown that the parameters have different tendencies of sensitivity because each heat source term is affected by different parameters. Accordingly, the parameters are clustered into their sensitive SOC ranges, and as a result, a new parameter identification procedure is developed based on a three-stage stepwise identification procedure. The identified parameters are further validated, which has shown that the proposed method is able to estimate the parameters accurately with less experiment set.

In the third part, the charging algorithm is extended by considering subzero temperatures, where mechanical degradation is also considered. The model is further experimentally validated at subzero temperature, showing that a steep concentration gradient affects the mechanical degradation at the cathode electrode. Finally, a charging algorithm at subzero temperature is designed, where nonlinear model predictive control and genetic algorithm are applied to optimize charging profile and start-up heating strategy. The cycling results by the algorithm are further compared with those by normal charging methods, which has shown that the proposed algorithm is able to charge the battery faster with higher charging capacity than those using normal charging methods. In addition, the degradation rate by the proposed algorithm is comparable to the normal charging methods.

As a closing work to the dissertation, we further propose an implementation of various optimization techniques that can be applied to the ROM. Since the current optimization techniques still have some drawbacks such as long calculation time or additional tasks of finding optimal weighting factor for a trade-off between different objective functions, a comparison of various online or offline optimization techniques may bring a solution for future direction for the optimization of the parameter identification or charging algorithm under a wide range of temperatures.

# Acknowledgments

I would first like to extend my sincere appreciation to my advisor, Dr. Song-Yul Choe, whose insightful expertise and guidance were invaluable for me to sharpen my scientific mindset and bring my work to a higher level. My appreciation also extends to the committee members and the university reader: Dr. Jeffrey Fergus, Dr. Roy Knight, Dr. Robert Dean, and Dr. Yanzhao Cao, for their consistent encouragement, constructive comments, and valuable suggestions during the completion of the dissertation. In addition, I would like to acknowledge my colleagues: Dr. Xinchen Zhao, Dr. Yilin Yin, Dr. Yalan Bi, Dr. Yang Hu, Ms. Kyungjin Yu, Mr. Xiaoniu Du, Ms. Munnyeong Choi, Mr. Junbeom Park, and Mr. James Choi for the intense discussions and their support to my work. Finally, I would like to thank my family and friends for their wise counsel and sympathetic ear.

# Table of Contents

# List of Tables

# List of Figures

# List of Symbols

| | |
|---|---|
| $A$ | Sandwich area of the cell (cm$^2$) / contact area (cm$^2$) / surface area of active material (cm$^2$) |
| $a_s$ | Specific surface area of electrode (cm$^{-1}$) |
| $c$ | Ion concentration (mol m$^{-3}$ ) |
| $c_{s,ave}$ | Volume-averaged concentration of lithium ion in solid phase (mol cm$^{-3}$) |
| $c_{s,max}$ | Maximum concentration of lithium ion in solid phase (mol cm$^{-3}$) |
| $c_{s,surf}$ | Surface concentration of lithium ion in solid phase (mol cm$^{-3}$) |
| $c_e$ | Concentration of lithium ion in electrolyte phase (mol cm$^{-3}$) |
| $D$ | Diffusivity (cm$^2$ s$^{-1}$) |
| $D_s$ | Diffusivity of lithium ion in solid phase (cm$^2$ s$^{-1}$) |
| $D_e^{eff}$ | Effective diffusivity of lithium ion in electrolyte phase (cm$^2$ s$^{-1}$) |
| $E$ | Open circuit voltage (V) |
| $E_{elec}$ | Electric energy (J) |
| $F$ | Faraday constant (96,487 C mol$^{-1}$) |
| $f$ | Frequency (Hz) |
| $I$ | Applied current (A) |
| $i_0$ | Exchange current density (A cm$^{-2}$) |

| | |
|---|---|
| $j^{Li}$ | Reaction rate (A cm$^{-3}$) |
| $K$ | Thermal conductance (WK$^{-1}$) |
| $k$ | Thermal conductivity (Wm$^{-1}$K$^{-1}$) / kinetic rate constant (A cm$^{-2}$)(cm$^{3}$mol$^{-1}$)$^{1.5}$ |
| $k_0$ | Isolation coefficient due to SEI |
| $L$ | Thickness of cell unit (cm) |
| $l$ | Thickness of the micro cell (m) |
| $Q$ | Capacity of the cell (Ah) / Heat energy (J) |
| $\dot{Q}$ | Heat generation rate (W) |
| $q$ | Amount of ion loss (Ah) |
| $q_{ave}$ | Volume-averaged concentration flux of lithium ion in solid phase (mol cm$^{-4}$) |
| $R$ | Resistance (Ω) / universal gas constant (8.314 J mol$^{-1}$ K$^{-1}$) |
| $R_s$ | Radius of spherical electrode particle (cm) |
| $r$ | Coordinate along the radius of electrode particle (cm) |
| $T$ | Cell temperature (K) |
| $t$ | Time (s) |
| $U$ | Equilibrium potential (V) |
| $U_{OC}$ | Open circuit voltage (V) |
| $V$ | Voltage (V) or volume of the composite electrode (m$^{3}$) |

| | |
|---|---|
| $\tilde{V}$ | Molar volume (m$^3$ mol$^{-1}$) |
| $x$ | Stoichiometric number of the anode / Cartesian coordinate |
| $y$ | Stoichiometric number of the cathode |
| $z$ | Output state of the nonlinear state-space model |

Greek symbols

| | |
|---|---|
| $\alpha$ | Transfer coefficient for an electrode reaction / Thermal diffusivity (m$^2$s$^{-1}$) |
| $\delta$ | Thickness (cm) / Dirac delta function |
| $\varepsilon$ | Volume fraction of a porous medium |
| $\phi$ | Potential (V) |
| $\eta$ | Overpotential of electrode reaction (V) |
| $\theta$ | Aging parameters |
| $\kappa$ | Ionic conductivity (S m$^{-1}$) |
| $\sigma$ | Conductivity (S m$^{-1}$) |
| $\lambda$ | Fraction of plated lithium to form secondary SEI |

Subscripts and Superscripts

| | |
|---|---|
| $act$ | Actual |

| | |
|---|---|
| *amb* | Ambient |
| *ch* | Charge |
| *dch* | Discharge |
| *elec* | Electric |
| *irr* | Irreversible |
| *n* | Negative electrode |
| *p* | Positive electrode |
| *ref* | Reference |
| *rev* | Reversible |
| *s* | Separator |

# List of Abbreviations

| | |
|---|---|
| BV | Butler-Volmer equation |
| CC | Constant current |
| CP | Constant power |
| CV | Constant voltage |
| DAQ | Data acquisition |
| DC | Direct current |
| ECM | Equivalent circuit model |
| EIS | Electrochemical impedance spectroscopy |
| EKF | Extended Kalman filter |
| EV | Electric vehicle |
| FOM | Full order model |
| HGR | Heat generation rate |
| MCC | Multistage constant current |
| ODE | Ordinary differential equation |
| PDE | Partial differential equation |
| ROM | Reduced-order model |
| SEI | Solid electrolyte interphase |

| | |
|---|---|
| SOC | State of charge |
| TEA | Thermoelectric assembly |
| TEM | Thermoelectric module |
| TMS | Thermal management system |

# Chapter 1. Introduction

## 1.1 Background

Electric vehicles (EVs) have become one of the most sustainable solutions for future transport, considering the depletion of fuel sources, which brings lithium-ion battery (LiB) to be focused as a state-of-the-art energy source considering high power and energy densities. However, compared to internal combustion engine vehicles, driving range of EVs is still relatively short. Accordingly, more batteries are installed to increase capacity of battery pack, which results in a long charging time. The charging time can be reduced simply by increasing current rates (C-rates), which adversely reduce battery lifetime, which presents one of the major barriers to overcome for the rapid commercialization of EVs. The lifetime of the LiBs used for the EVs is generally expected as approximately from 8 to 10 years when the EVs can travel from 120,000 to 240,000 km [1]. The LiB is continuously aged during the lifetime, and efficiency is reduced due to various degradation sources that can be accelerated by the increased C-rates. Another technical barrier is vulnerability to the operating temperatures. Charging and discharging LiBs involve many complex processes such as charge transport, chemical reactions, and intercalation or deintercalation. Those processes are significantly affected by operating temperature, which directly leads to the efficiency, cycle life, and robustness of the battery. Especially at low operating temperatures, due to increased charge transfer resistance and decreased ionic diffusivity, the charging time and capacity become significantly reduced, and fast charging with an inappropriate current profile can cause severe degradation with safety issues, such as internal short circuit, thermal runaway, and fire accident. In addition, the price of core materials for lithium-ion batteries, such as lithium or nickel, is rapidly increasing [2]. Accordingly, the development of a proper charging algorithm that can extend the lifetime of the LiBs under a wide range of operating temperatures has become a crucial factor, considering all features such as environmental and economical aspects.

## 1.2 Motivation and objectives

There have been many studies focusing on the optimization of charging algorithms, where a battery model is used to consider the degradation of the battery. The fundamental understanding of the battery degradation under a wide range of temperatures is a crucial factor for the proper design of the charging algorithm. The degradation of LiB is a complicated process, including various mechanisms that are significantly affected by operating temperature and occur interactively in all cell components, where chemical and mechanical degradation have been commonly reported as the major degradation sources [1][3]. Recently, several attempts have been made to consider both degradation sources [9], but those models can be only applicable to Full-Order electrochemical Models (FOMs) that solve complex governing equations for charge transport and reactions, including Partial Differential Equations (PDEs) and nonlinear equations. The high complexity of the model requires enormous computational time, which cannot be applied to control-oriented real-time applications. In addition, none of the research has been conducted to develop the charging algorithm at subzero temperature using the model.

Therefore, this dissertation aims to design a fast and safe charging algorithm considering subzero temperatures, where a reduced-order electrochemical-thermal life model with high fidelity is also required to estimate the battery characteristics and degradation accurately.

## 1.3 Scholarly contributions and dissertation structure

In this work, the development of a fast and safe charging algorithm considering subzero temperature could make certain scholarly contributions since it provides comprehensive and systematic guidelines for the charging algorithm of LiBs. In particular, the contributions are:

- Development of degradation model that is able to estimate the growth of SEI layer, lithium plating, and lithium stripping and experimental validation at room temperatures,
- Design of a fast and safe charging algorithm considering side reaction, lithium plating, and lithium stripping at room temperature,
- Development of a reduced-order electrochemical-thermal model that is validated from -30°C to 45°C with detailed analysis on heat source terms,
- Design of a new parameter identification method based on parameter sensitivity analysis with respect to the battery heat generation rate,
- Extension of the degradation by considering a reduced-order mechanical degradation model and experimental validation at subzero temperatures,
- Extension of the fast charging algorithm at subzero temperatures considering a start-up strategy to warm up the battery.

This dissertation is organized as follows.

- Chapter 1 introduces the research background, motivation and objectives, and scholarly contributions.

- Chapter 2 propose a fast and safe charging algorithm that limits side reaction and lithium plating at room temperatures. In addition, negative pulse currents are applied to recover lithium ions out of metallic lithium, particularly at the low SOC range.

- Chapter 3 describes a reduced-order electrochemical-thermal model and its validation against the experimental data under a wide range of temperatures and current rates. Further analysis of the battery heat source terms is also conducted, and the model is extended into a 1-dimensional model considering each component in a single cell. In addition, a sensitivity analysis is conducted for the battery design parameters with respect to the heat generation rate. Based on the results, a new parameter identification procedure is proposed that requires fewer experiment data than conventional parameter identification methods.

- Chapter 4 extends the charging algorithm proposed in Chapter 2 by considering a start-up strategy at subzero temperatures. A degradation model considering side reaction, lithium plating, and mechanical degradation is developed based on the reduced-order electrochemical-thermal model and validated at subzero temperatures. The extended algorithm is experimentally verified by comparing results with conventional charging methods.

- Chapter 5 concludes the dissertation.

# Chapter 2. Design of fast and safe charging method considering degradation at room temperature

## 2.1 Literature review

### 2.1.1 Review of current charging strategies

There are many suggestions on the design of charging methods that reduce charging time and degradation. A study conducted by the U.S. Army research laboratory stated that charging algorithms for lithium-ion batteries, such as constant current (CC) charging, constant power (CP) charging, and multistage constant current (MCC) charging, have a significant impact on their cycle life [11]. One of the most commonly used charging algorithms is the constant current and constant voltage (CC/CV) charging because of its simple and easy implementation to chargers. During the constant current charging, a cell is charged with a preset current amplitude until the terminal voltage reaches a cutoff voltage set. Once the voltage reaches the cutoff voltage, the applied voltage is kept constant, and then the charging current decreases as the state of charge (SOC) increases. The charging time cannot be significantly reduced by increased constant current because the cutoff voltage is reached earlier, and correspondingly an extra time is required during the following CV charging. Other options are constant power and constant voltage charging (CP/CV) or multistage constant current and constant voltage charging (MCC/CV), where the amplitude of the charging current and its duration is hard to determine. A new design of protocols is approached using electric equivalent circuit models or neural network models constructed using experimental data [12] in conjunction with an extended Kalman filter (EKF) [13]. However, empirical models do not provide internal physical variables and cannot fully consider battery degradation. Therefore, the variables need to be extracted from an electrochemical model. According to the previous studies on fast charging methods based on the electrochemical model [14], there are several limitations for charging current rates at a given SOC that include side reaction rate, terminal cutoff voltage, and lithium-ion surface concentration. In addition, resting pulses are added to decrease the surface concentration of lithium ions. However, these methods do not consider the degradation caused by lithium plating that is the most dominant cause at high current charging. Further studies have been focused on the understanding of the effects of charging currents on lithium plating so that a charging algorithm can be designed that suppresses the lithium plating.

### 2.1.2 Review of aging mechanisms

The degradation of LiB is a complicated process, including various mechanisms that occur interactively in all cell components, where chemical and mechanical degradation have been commonly reported as the major degradation sources. Chemical degradation is generally identified as the most dominant degradation source, where two widely known reactions are a formation of an insoluble passivation layer and metallic lithium. The insoluble passivation layer is called a Solid-Electrolyte-Interphase (SEI), and it is generated at the surface of anode active material particles while consuming lithium ions and electrolyte solvents during charging [4], which is called a side reaction. In fact, an initial SEI is artificially created to protect the active material particles from further reaction with the electrolyte due to its permeability to lithium ions but impermeability to electrons [3]. However, as the cell is cycled, the SEI is continuously generated and deposited, consuming lithium ions, which leads to the capacity fade. In addition, the electrolyte is dried because of the consumption of the electrolyte solvents, and the active area of the particles is reduced because of the accumulation of the deposited layers covering pores and the surface of the particles. As a result, the power is faded [15][16]. Secondly, the metallic lithium is formed as the precipitation of the lithium ions on the surface of the particles when overpotential at the surface of the particles is smaller than equilibrium potential of lithium deposition [17], which is called lithium plating. When the lithium plating takes place, the lithium ions are consumed while producing a metallic plate that covers the pores and the surface of the anode particles, which leads to the capacity and power fade, respectively. The lithium plating tends to happen only in extreme conditions, especially for charging under low temperatures and high C-rates [1][4]. However, due to its high degradation rate, once the lithium plating happens, it can rapidly increase further degradations. In addition, it can cause the growth of dendrites that can penetrate the separator and reach the positive electrode, which causes an internal shorting of the cell and poses a potential safety risk [9].

On the other hand, the fundamental mechanism of mechanical degradation is a crack and fracture of active material particles under internal stress that is called diffusion-induced stress (DIS). During the cycling, a steep lithium-ion concentration gradient is developed, and the displacement is caused by the intercalation of lithium ions inside the active material particles, leading to stress and strain. Consequently, the particles can be cracked, isolated from the main structure, and become inactive [9], leading to a loss of active materials. Therefore, the capacity and power are also faded.

The degradation of LiBs is dependent upon many factors, such as the chemistry of electrodes, operating temperature, C-rate, and SOC. The chemistry of the electrodes generally determines the general mechanism of the degradation, where the main degradation source of the anode and cathode electrodes is different because of the different chemistries. In case of the anode electrode, most of the currently commercialized LiBs use carbonaceous, generally graphite-based, materials because of their high capacity, low cost, long cycle life, and low volume expansion [18][19][20]. Despite those advantages, the graphite anode can be unstable because the operating potential of the graphite anode is approximately 0.05V [21][22], which is outside of the stabilized potential window of conventional organic electrolyte that is around 1V ~ 4.5V [23][24]. As a result, during charging, the potential difference between the anode active material particle and the electrolyte can become smaller than the equilibrium potentials of the side reaction and the lithium plating, which leads to a favorable condition for the reactions. On the other hand, it has been reported that the effect of the mechanical degradation on the anode electrode is not significant compared to that on the cathode electrode [1][25][26].

In case of the cathode electrode, currently, the most commonly used material for the cathode electrode is $Li[Ni_xCo_yMn_x]O_2$ that partially replaces Co in lithium cobalt oxide ($LiCoO_2$) by Ni and Mn to achieve improved electrochemical performance while reducing the material cost. Since each material provides different characteristics, the proportion of the materials can influence the performance of the battery. For example, Ni can offer high capacity but poor cycle life and thermal stability, while Mn can provide good cycle life and safety, and Co can increase the electronic conductivity, resulting in lower resistance and excellent power performance [26]. The first commercialized and widely used ratio of NMC is $Li[Ni_{1/3}Co_{1/3}Mn_{1/3}]O_2$. For the next-generation LiBs, in order to achieve a larger capacity, the proportion of Ni is increased to $Li[Ni_{0.6}Co_{0.2}Mn_{0.2}]O_2$ or even $Li[Ni_{0.8}Co_{0.1}Mn_{0.1}]O_2$ [27][28]. Despite those advantages, the cathode active material has a weakness of the mechanical degradation [25][26]. Compared with the anode electrode, recent experiments have shown that only 5% of volume change of the particles by the intercalation of the lithium ions can lead to a heavy structural disintegration and mechanical failure over cycle life for the class of NMC [29][30][31].

Temperature is also one of the major factors affecting the degradation as well as the performance of the battery. At high temperatures, the rate of electrochemical reactions becomes higher, leading to increased cell efficiency. However, the rate of the side reaction also becomes higher, which leads to the acceleration of the chemical degradation. On the other hand, at low temperatures, the diffusivity of lithium ions becomes sluggish, which leads to an increase in internal resistance and a decrease in cell efficiency. The rate of the side reaction becomes smaller as well, however, due to the reduced electrochemical reaction rate, the ions are accumulated at the surface of the anode active material particles during charging. Then, the potential at the surface of the particles is decreased, which leads to the lithium plating. In addition, due to reduced diffusivity, the gradient of ion concentration within the active material particles becomes sharp at high C-rates, which leads to a higher mechanical strain, and consequently, a formation of fractures and cracks [32][33][34].

In this chapter, a charging algorithm that reduces the charging time and minimizes the degradation at room temperature is proposed. Since the chemical degradation is generally identified as the most dominant degradation source at high temperatures, the mechanical degradation is not considered. The development of the mechanical degradation model will be discussed in Chapter 4.

The most dominant chemical degradation sources are a side reaction and lithium plating. In this study, two reactions are considered as the side reactions as follows [35];

$$\mathrm{2Li^{+}+2e^{-}+EC \rightarrow CH2{=}{=}CH2+Li_2CO_3} \downarrow \tag{1}$$

$$\mathrm{2Li^{+}+2e^{-}+2EC \rightarrow CH2{=}{=}CH2+\left(CH_2OCO_2Li\right)_2} \downarrow \tag{2}$$

Main products are $\mathrm{Li_2CO_3}$ and $\mathrm{\left(CH_2OCO_2Li\right)_2}$ that form the compounds of a thin passive layer on anode particle surface that is the main components of the SEI. An initial SEI is artificially created to protect the electrode from further reaction with the electrolyte because of its permeability to lithium ions but impermeability to electrons [15]. However, as cycled, side reaction takes place continuously and produces the SEI layer that covers pores of the electrode [16]. As a result, electrode porosity gets decreased, and internal impedance gets increased. Consequently, power gets faded. In addition, the lithium ions consumed by the side reaction and isolated particles completely covered by SEI layers lead to capacity fade.

Lithium plating forms metallic solid lithium from the lithium ions and electrons, which can be expressed as follows;

$$\mathrm{Li^{+}+e \rightarrow Li(s)} \tag{3}$$

The lithium plating consumes lithium ions, while the metallic plate covers the surface of particles on the anode electrode and reduces an active area. In addition, some plated lithium metal reacts with the electrolyte and becomes insoluble products such as $\mathrm{Li_2CO_3}$ and $\mathrm{(CH_2OCO_2Li)_2}$, which is called secondary SEI [36]. The products can block the pores, reduce ionic kinetics [37] and active anode material [38], which also leads to power and capacity fade. Due to both reactions, the thickness of SEI grows, conductivity of electrolytes decreases, and a layer is formed by a new SEI and the secondary SEI at an interface between anode and separator that is called a deposited layer. All of the depositions are summarized with two impedances, SEI, and deposited layer. The decrease of the active area and the increases of the two resistances are the main causes of degradation. On the other hand, there is a reverse reaction of lithium plating, which is called lithium stripping. A certain amount of the plated lithium can be dissolved during discharge, and this reaction promotes recovering ions that are lost during lithium plating [39]. For modeling of side reaction and lithium plating effects, the following assumptions have been made;

- Chemical degradation takes place only on the anode electrode, and depositions on the anode particles are a mixture of primary and secondary SEI layer and plated lithium,
- Products of the primary and secondary SEI layer is composed of $\mathrm{Li_2CO_3}$ and $\mathrm{(CH_2OCO_2Li)_2}$,

- Decrease of active area and porosity is calculated from the average thickness of the deposits, and
- Mechanical failure, gas generation, and the effect of dendrite are not considered.

A schematic diagram of the mechanism of chemical degradation on the anode particle is depicted in Figure 1, where arrows indicate the path of participating charges, which includes lithium ions, EC, and electrons, and the location where reactions take place. Since the SEI layer is ionic conductive but isolative to electrons [15], all reactions that include the main reaction, side reaction, and lithium plating take place at the interface between the SEI layer and the particle. On the other hand, once lithium metal is deposited on the particle surface, no ion can be transported through plated lithium because of its permeability to ions but impermeability to ions. As a result, no further main reaction is possible. However, electrons in the particles can flow through plated lithium and participate in the side reaction or lithium plating on the surface of the plated lithium. Even if the SEI layer or secondary SEI layer on the plated lithium already exists, it is still possible for an additional SEI layer or secondary SEI layer to build at the interface of the plated lithium and SEI layer.

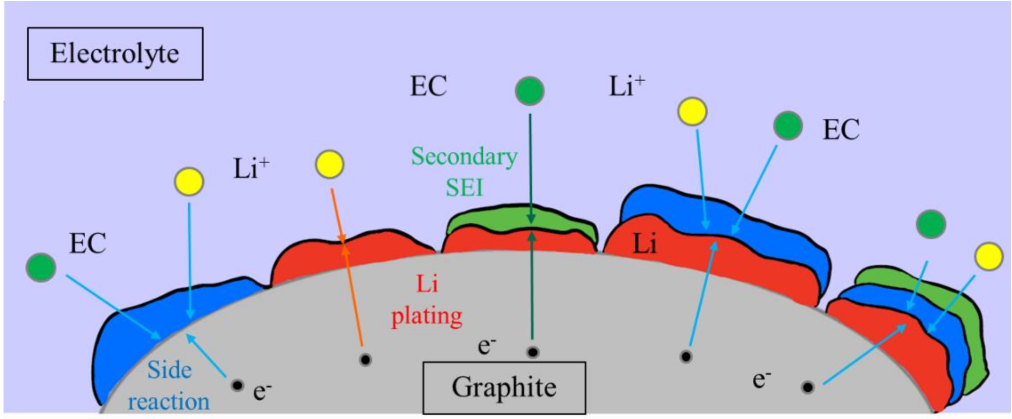

Figure 1. Schematic diagram of different types of depositions on a graphite particle.

## 2.2 Modeling of chemical degradation

### 2.2.1 Main reaction

The reaction rate produced by a main chemical reaction taking place at the interface between electrode and electrolyte is governed by Butler-Volmer (BV) equation [40].

$$j_{int}^{Li} = a_{s,int} i_{0,int} \left[ \exp\left( \frac{\alpha_a F}{RT} \eta_{int} \right) - \exp\left( -\frac{\alpha_c F}{RT} \eta_{int} \right) \right] \tag{4}$$

, where $a_{s,int}$ is the specific reaction area of intercalation, $\eta_{int}$ is the surface overpotential, and $i_{0,int}$ is the exchange current density of the intercalation that can be expressed as follows;

$$i_{0,int} = k_{i0} \left( c_e \right)^{\alpha_a} \left( c_{s,\max} - c_{s,surf} \right)^{\alpha_a} \left( c_{s,surf} \right)^{\alpha_c} \tag{5}$$

, where $k_{i0}$ is the kinetic rate constant, $c_{s,\max}$ and $c_{s,surf}$ are the maximum ion concentration and surface ion concentration of the particles, respectively. $\alpha_a$ and $\alpha_c$ are constants that represent anodic and cathodic intercalation, which are symmetric in the main reaction and set as 0.5 for each value. The overpotential for the main intercalation is given as follows;

$$\eta_{int} = \varphi_s - \varphi_e - U_{eq,int} - V_{SEI,int} \tag{6}$$

$$V_{SEI,int} = \frac{R_{SEI,total}}{a_{s,int}} j_{total}^{Li} \tag{7}$$

, where $\varphi_s$ and $\varphi_e$ are electric potentials of the surface of the anode electrode particle and the electrolyte, respectively. $U_{eq,int}$ is the equilibrium potential for the intercalation. $j_{total}^{Li}$ is the total reaction rate that includes the main reaction, the side reaction, and the lithium plating or the lithium stripping;

$$j_{total}^{Li} = j_{int}^{Li} + j_{side}^{Li} + j_{Li}^{Li} \tag{8}$$

$R_{SEI,total}$ is the sum of the SEI and the secondary SEI resistance. $R_{SEI,0}$ is the SEI resistance formed at the initial cycle, which is measured by electrochemical impedance spectroscopy (EIS) equipment.

$$R_{SEI,total}\left(\tau\right) = R_{SEI,0} + R_{SEI}\left(\tau\right) + R_{SEI,sec}\left(\tau\right) \tag{9}$$

### 2.2.2 Modeling of side reaction

The rate of side reaction can be also expressed using the BV equation.

$$j_{side}^{Li} = a_s i_{0,side}\left[\exp\left(\frac{\alpha_{a,side} n_{side} F}{RT}\eta_{side}\right) - \exp\left(-\frac{\alpha_{c,side} n_{side} F}{RT}\eta_{side}\right)\right] \tag{10}$$

, where $i_{0,side}$ is the exchange current density of the side reaction that is a function of reactants of the side reaction, lithium ions, and ethylene carbonate (EC) molecules.

$$i_{0,side} = k_{side}\sqrt{c_{s,surf}c_{EC,R_s}} \tag{11}$$

, where $k_{side}$ is the kinetic rate constant for the side reaction. $c_{EC,R_s}$ is the concentration of EC molecules at the surface of anode particles.

$n_{side}$ is the number of ions involved in the side reaction that is equal to 2. $\eta_{side}$ is the surface overpotential of the side reaction defined as follows;

$$\eta_{side} = \varphi_s - \varphi_e - U_{eq,side} - \frac{R_{SEI,total}}{a_{s,side}} j_{total}^{Li} \tag{12}$$

, where $a_{s,side}$ is the specific reaction area of the side reaction and $U_{eq,side}$ is the equilibrium potential for the side reaction.

Since the side reaction is irreversible and dominated by the reduction process rather than the oxidation process, (10) can be simplified as follows;

$$j_{side}^{Li} = -a_{s,side} i_{0,side} \exp\left(-\frac{\alpha_{c,side} n_{side} F}{RT}\eta_{side}\right) \tag{13}$$

The total number of the consumed lithium ions is obtained by integration of the side reaction rate over the composite anode and cycling time.

$$q_{\mathrm{loss}}^{SR}(\tau) = \int_{x=0}^{\delta_-}\left\{\int_{t=0}^{\tau} j_{side}^{Li}(x,t)dt\right\} A dx \tag{14}$$

, where $q_{loss}^{SR}$ is the consumed lithium ions, $\delta_{-}$ is the thickness of the composite anode, and $A$ is the cross-section area of the cell.

On the other hand, the amount of consumed solvents of the electrolyte is reflected with the volume fraction rate of the electrolyte as follows;

$$\Delta\varepsilon_{e,side}\left(\tau\right)=-\frac{\alpha\tilde{V}_{e}q_{\mathrm{loss}}^{SR}\left(\tau\right)}{A\delta\_F} \tag{15}$$

, where $\tilde{V}_{e}$ is the molar volume of the electrolyte and $\alpha$ is the reaction coefficient of the EC. Under the assumption that the products from side reaction have the same reaction rate, the average value of the consumed solvents of the electrolyte that are 0.5 for $\mathrm{Li_2CO_3}$ and 1 for $\left(\mathrm{CH_2OCO_2Li}\right)_2$ when one mole of lithium ion is consumed is used for the reaction coefficient of the EC.

Subsequently, the effective diffusivity of the lithium ion in the electrolyte is affected by the change of the electrolyte volume fraction affects as follows;

$$D_{e}^{eff}=D_{e}\cdot\varepsilon_{e} \tag{16}$$

, where $\varepsilon_{e}$ is the porosity that indicates a volume fraction of electrolyte that decreases as degraded.

Similarly, the change of the volume fraction of the active material caused by the deposition of the SEI layer can be described as follows;

$$\Delta\varepsilon_{s,side}\left(x,\tau\right)=-\frac{\tilde{V}_{SEI}}{n_{side}F}\int_{t=0}^{\tau}j_{side}^{Li}\left(x,t\right)dt \tag{17}$$

The change of the average thickness of the SEI layer at different locations and deposited layer can be expressed as;

$$\Delta\delta_{SEI}\left(x,\tau\right)=\frac{\tilde{V}_{SEI}}{a_s n_{side}F}\int_{t=0}^{\tau} j_{side}^{Li}\left(x,t\right)dt \tag{18}$$

$$\Delta\delta_{DL,side}\left(\tau\right)=\frac{\tilde{V}_{SEI}R_s}{n_{side}F}\int_{t=0}^{\tau} j_{side}^{Li}\left(\delta_{-},t\right)dt \tag{19}$$

, where $\tilde{V}_{SEI}$ is the molar volume of the SEI layer and $R_s$ is the radius of the anode particle.

The corresponding increase of the resistances for the SEI and deposited layer can be obtained using the ionic conductivity of the SEI and the deposited layer as follows;

$$\Delta R_{SEI}\left(x,\tau\right)=\Delta\delta_{SEI}\left(x,\tau\right)/\kappa_{SEI} \tag{20}$$

$$\Delta R_{DL}\left(\tau\right)=\Delta\delta_{DL,side}\left(\tau\right)/\kappa_{DL} \tag{21}$$

### 2.2.3 Modeling of lithium plating and stripping

#### 2.2.3.1 Introduction

Lithium plating and stripping are reduction and oxidation reaction processes. The rate of lithium plating or stripping can be also expressed using the BV equation

$$j_{LiP/S}^{Li}=a_{s,Li}i_{0,Li}\left[\exp\left(\frac{\alpha_{a,Li}F}{RT}\eta_{LiP/S}\right)-\exp\left(-\frac{\alpha_{c,Li}F}{RT}\eta_{LiP/S}\right)\right] \tag{22}$$

, where $i_{0,Li}$ is the exchange current density of the reaction.

In fact, because the secondary SEI is insoluble, the lithium plating and stripping are semi-reversible. Therefore, $\alpha_{c,Li}$ and $\alpha_{a,Li}$ are set to be 0.3 and 0.7 [36].

The lithium plating occurs during charging the local lithium plating overpotential against a reference of Li/Li+ is less than 0V, which makes the kinetics of lithium plating higher than that of the main reaction [41].

Conversely, the lithium stripping takes place during discharging. When the short discharging currents are applied during charging (pulse charging), not only concentration of lithium ions are decreased but also plated lithium metal is dissolved and lithium ions are released [42]. If the plated lithium has already reacted with EC and becomes the secondary SEI, the plated lithium cannot be dissolved. If the plated lithium is completely covered by the primary or secondary SEI layer, the lithium is no longer dissolved and becomes dead lithium.

A model for the lithium stripping is developed under the following assumptions;

- Lithium stripping takes place only when plated lithium is already generated.
- If the plated lithium is completely dissolved, no more lithium stripping exists.
- Once the plated lithium reacts with EC and generates the secondary SEI, lithium stripping cannot take place.
- The rate of secondary SEI formation from lithium plating is constant.

#### 2.2.3.2 Lithium plating

The overpotential of the lithium plating is expressed by [43]

$$\eta_{Li} = \varphi_s - \varphi_e - U_{eq,Li} - \frac{R_{SEI,total}}{a_{s,Li}} j_{total}^{Li} \tag{23}$$

$$\eta_{LiP} = \begin{cases} 0 & for\, \eta_{Li} \geq 0 \\ \eta_{Li} & for\, \eta_{Li} < 0 \end{cases} \qquad \text{for lithium plating}$$

, where $a_{s,Li}$ is the specific active area of the lithium plating that is the same as $a_{s,side}$. $U_{eq,Li}$ is the equilibrium potential for lithium plating and stripping and is assumed to be zero because the potential is measured with respect to a lithium metal reference [36].

The total number of ion loss consumed by the lithium plating and the secondary SEI is obtained by integration of the reaction rate over the composite anode during a given time.

$$q_{\text{loss}}^{LiP}(\tau) = \int_{x=0}^{\delta_-} \left\{ \int_{t=0}^{\tau} (1-\lambda)\, j_{LiP}^{Li}(x,t) dt \right\} A dx \tag{24}$$

$$q_{\text{loss}}^{SEI,\text{sec}}(\tau) = \int_{x=0}^{\delta_-} \left\{ \int_{\tau=0}^{t} \lambda\, j_{LiP}^{Li}(x,\tau) d\tau \right\} A dx \tag{25}$$

, where $\lambda$ is the ratio for the amount between the plated lithium and the secondary SEI layer formed from the plated lithium.

The consumed electrolyte by the secondary SEI can be expressed as follows;

$$\Delta\varepsilon_{e,SEI,sec}(\tau) = -\frac{\alpha \tilde{V}_e q_{loss}^{SEI,\text{sec}}(\tau)}{A\delta\_F} \tag{26}$$

, where $\alpha$ is assumed to be the same as that of the side reaction. It also changes the effective diffusivity of the lithium ion from the equation (16).

A volume fraction of active material induced by the plated lithium and the secondary SEI layer is expressed as follows;

$$\Delta\varepsilon_{s,LiP}\left(x,\tau\right)=-\frac{\tilde{V}_{Li}}{n_{LiP}F}\int_{t=0}^{\tau}\left(1-\lambda\right)j_{LiP}^{Li}\left(x,t\right)dt \tag{27}$$

$$\Delta\varepsilon_{s,SEI,sec}\left(x,\tau\right)=-\frac{\tilde{V}_{SEI}}{n_{side}F}\int_{t=0}^{\tau}\lambda\, j_{LiP}^{Li}\left(x,t\right)dt \tag{28}$$

, where $n_{LiP}$ is the number of ions involved in the lithium plating that is equal to 1 and $\tilde{V}_{Li}$ is the molar volume of the plated lithium.

Increase of thickness of the secondary SEI layer from the plated lithium can be expressed as;

$$\Delta\delta_{SEI,sec}\left(x,\tau\right)=\frac{\tilde{V}_{SEI}}{a_s n_{side}F}\int_{t=0}^{\tau}\lambda\, j_{LiP}^{Li}\left(x,t\right)dt \tag{29}$$

The corresponding increase of the SEI resistance, including the SEI and the secondary SEI layer, can be expressed from the equation (20).

An increase of thickness of the deposited layer from the plated lithium and the secondary SEI layer can be expressed as follows;

$$\Delta\delta_{DL,LiP}\left(\tau\right)=\frac{\tilde{V}_{LiP}R_s}{F}\int_{t=0}^{\tau}\left(1-\lambda\right)j_{LiP}^{Li}\left(\delta_{-},t\right)dt \tag{30}$$

$$\Delta\delta_{DL,SEI,sec}\left(\tau\right)=\frac{\tilde{V}_{SEI}R_s}{n_{side}F}\int_{t=0}^{\tau}\lambda\, j_{LiP}^{Li}\left(\delta_{-},t\right)dt \tag{31}$$

The corresponding increase of the deposited layer resistances, including the SEI, the secondary SEI layer, and the plated lithium, can be expressed from the equation (21).

### 2.2.3.3 Lithium stripping

Likewise, the overpotential for the lithium stripping is defined by

$$\eta_{LiS} = \begin{cases} \eta_{Li} & for\, \eta_{Li} \geq 0 \\ 0 & for\, \eta_{Li} < 0 \end{cases} \qquad \text{for lithium stripping}$$

, where $\eta_{Li}$ is calculated according to the equation (23). Because of the lithium stripping, the total amount of recovered lithium ions can be obtained by integration of reaction rate over the composite anode and time.

$$q_{\text{recovery}}^{LiS}(\tau) = \int_{x=0}^{\delta_-} \left\{ \int_{\tau=0}^{t} j_{LiS}^{Li}(x,\tau) d\tau \right\} A dx \tag{32}$$

Finally, the total ion loss by the lithium plating and stripping is the sum of individual loss and recovery that is given by the equations (24), (25), and (32);

$$q_{\text{loss}}^{Li}(\tau) = q_{\text{loss}}^{LiP}(\tau) + q_{\text{loss}}^{SEI,\text{sec}}(\tau) + q_{\text{recovery}}^{LiS}(\tau) \tag{33}$$

## 2.3 Model validation

Analysis and design of a charging algorithm considering the degradation require information of internal variables in real-time such as ion concentrations, side reaction rate, and anode potential that cannot be measured from the terminal of a battery cell. These variables can be estimated only using a validated electrochemical model. Charging or discharging of lithium-ion batteries involves several processes that include ion transport and reactions. They are migration, diffusion, and intercalation or deintercalacation. The processes are governed by nonlinear or PDE that describe physical laws, which can be solved by applying the FOM that is computationally expensive. Thus, the FOM is inappropriate for control purposes in real-time, even with high accuracy. A possible approach is to reduce the order of the FOM by converting PDEs into ordinary differential equations (ODEs) and linearizing the nonlinear equations, which is called a reduced-order electrochemical model (ROM). Details of the equations are summarized in Table 1. The constructed ROM embedding side reaction and lithium plating model is validated using a large format of lithium-ion pouch cell that has a nominal capacity of 39Ah.

Table 1. Summary of FOM and ROM.

| Cell dynamics | FOM | ROM |
|---|---|---|
| Ion concentration in electrode | $\frac{\partial c_s}{\partial t}=\frac{D_s}{r^2}\frac{\partial}{\partial r}\left(r^2\frac{\partial c_s}{\partial r}\right)$<br>$\frac{1}{r}\frac{\partial c_s}{\partial r}\Big\rvert_{r=0}=0 \;\; and \;\; D_s\frac{\partial c_s}{\partial r}\Big\rvert_{r=R_s}=\frac{-j^{Li}}{a_s F}$ | $\frac{d}{dt}c_{s,ave}+3\frac{j^{Li}}{R_s a_s F}=0$<br>$\frac{d}{dt}q_{ave}+30\frac{D_s}{R_s^2}q_{ave}+\frac{45}{2}\frac{j^{Li}}{R_s^2 a_s F}=0$<br>$35\frac{D_s}{R_s}\left(c_{s,surf}-c_{s,ave}\right)-8D_s q_{ave}=-\frac{j^{Li}}{a_s F}$ |
| Ion concentration in electrolyte | $\frac{\partial(\varepsilon_e c_e)}{\partial t}=\frac{\partial}{\partial x}\left(D_e^{eff}\frac{\partial}{\partial x}c_e\right)+\frac{1-t_+^0}{F}j^{Li}$<br>$\frac{\partial c_e}{\partial x}\Big\rvert_{x=0}=\frac{\partial c_e}{\partial x}\Big\rvert_{x=L}=0$ | $\dot{\mathbf{c}}_{\mathbf{e}}=\mathbf{A}^*\cdot\mathbf{c}_{\mathbf{e}}+\mathbf{B}^*\cdot I$<br>$\mathrm{y}=\mathbf{C}^*\cdot\mathbf{c}_{\mathbf{e}}+\mathbf{D}^*\cdot I$ |
| Ohm's law in electrode | $\frac{\partial}{\partial x}\left(\sigma^{eff}\frac{\partial}{\partial x}\varphi_s\right)-j^{Li}=0$<br>$-\sigma^{eff}\frac{\partial}{\partial x}\varphi_s\Big\rvert_{x=0}=-\sigma^{eff}\frac{\partial}{\partial x}\varphi_s\Big\rvert_{x=L}=\frac{I}{A}$<br>$\frac{\partial}{\partial x}\varphi_s\Big\rvert_{x=\delta_-}=\frac{\partial}{\partial x}\varphi_s\Big\rvert_{x=\delta_-+\delta_{sep}}=0$ | $\frac{\partial}{\partial x}\left(\frac{\partial}{\partial x}\varphi_s\right)=\frac{j^{Li}}{\sigma^{eff}}$<br>$-\sigma^{eff}\frac{\partial}{\partial x}\varphi_s\Big\rvert_{x=0}=-\sigma^{eff}\frac{\partial}{\partial x}\varphi_s\Big\rvert_{x=L}=\frac{I}{A}$<br>$\frac{\partial}{\partial x}\varphi_s\Big\rvert_{x=\delta_-}=\frac{\partial}{\partial x}\varphi_s\Big\rvert_{x=\delta_-+\delta_{sep}}=0$ |
| Ohm's law in electrolyte | $\frac{\partial}{\partial x}\left(\kappa^{eff}\frac{\partial}{\partial x}\varphi_e\right)+\frac{\partial}{\partial x}\left(\kappa_D^{eff}\frac{\partial}{\partial x}\ln c_e\right)+j^{Li}=0$<br>$\frac{\partial}{\partial x}\varphi_e\Big\rvert_{x=0}=\frac{\partial}{\partial x}\varphi_e\Big\rvert_{x=L}=0$ | $\frac{\partial}{\partial x}\left(\frac{\partial}{\partial x}\varphi_e\right)+\frac{j^{Li}}{\kappa^{eff}}=0$<br>$\frac{\partial}{\partial x}\varphi_e\Big\rvert_{x=0}=\frac{\partial}{\partial x}\varphi_e\Big\rvert_{x=L}=0$ |
| Electrochemical Kinetics | $j^{Li}=a_s i_0\left\{\exp\left[\frac{\alpha_a nF}{RT}\eta\right]-\exp\left[-\frac{\alpha_c nF}{RT}\eta\right]\right\}$ | $j^{Li}=a_s i_0\frac{n(\alpha_a+\alpha_c)F}{RT}\eta$ |
| SOC | $SOC=\frac{1}{\delta_-}\int_0^{\delta_-}\frac{\left(c_{s,ave}-c_{s,\max}Stoi_{100}\right)}{c_{s,\max}\left(Stoi_{100}-Stoi_0\right)}dx$ | |

Firstly, the cell is cycled with 2C CC/CV charging until the terminal voltage reaches the cutoff voltage of 4.2V, where the cutoff current becomes 1/40C, and then discharged with 1C until the terminal voltage reaches 3.0V. The capacity is measured as a function of cycle numbers, and the results of capacity and discharge characteristics of terminal voltages from 0 to 320 cycles in every 40 cycles are plotted in Figure 2. The prediction error of the capacity by the ROM is less than 1%, while the voltage is accurately tracked. The capacity drops almost linear until 300 cycles because no lithium plating takes place, which is explored in detail later.

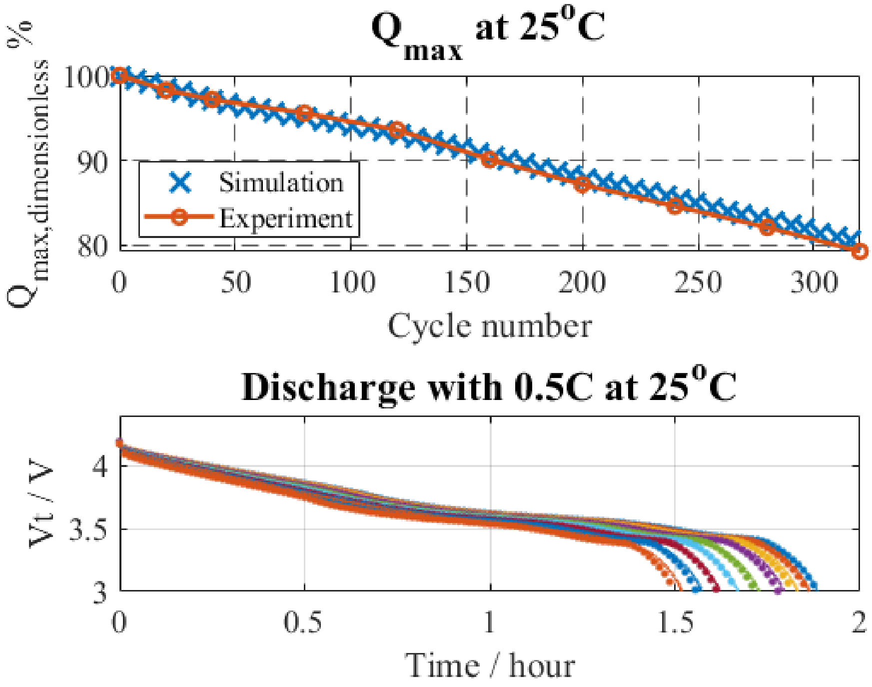

Figure 2. Experimental and simulated results by 2C CC/CV; capacity fade and terminal voltage when discharged with 0.5C CC.

With the degradation model, ion loss is calculated from the side reaction rate. Ion loss from 2C CC/CV charging as a function of cycle number is plotted on the top in Figure 3. Ion loss increases linearly because lithium plating does not occur until 300 cycles, and correspondingly, capacity decreases linearly, as shown in Figure 2. Side reaction rates rate at the particle closely located to the separator during one cycling with different cycle number are plotted on the bottom in Figure 3. Side reaction rate decreases in CV mode as the charging current decreases.

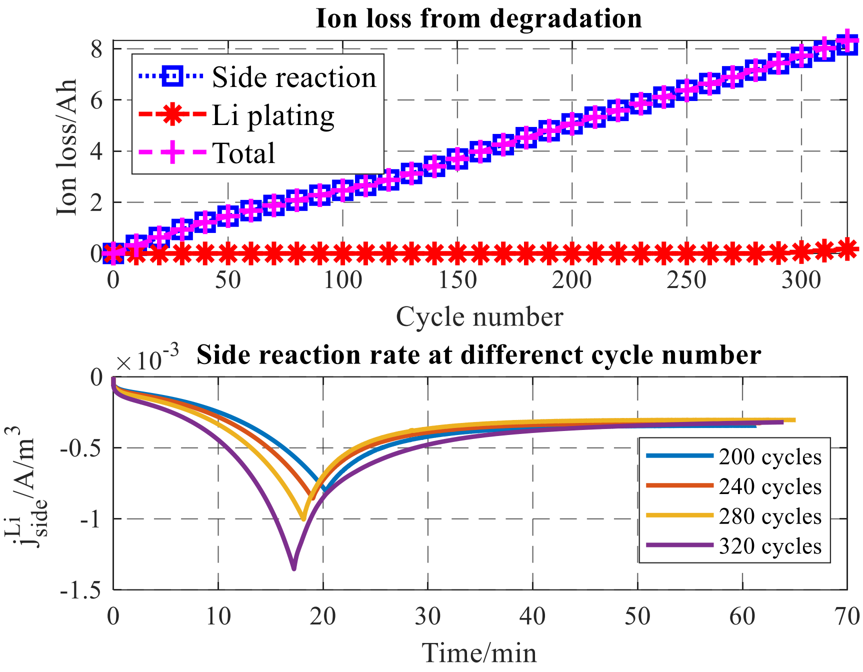

Figure 3. Ion loss calculated using degradation model and side reaction rate with 2C CC/CV charging.

In fact, high current rates during the charging process are one of the favorable conditions for the formation of lithium plating, and thus another cycling test is conducted with 5C CC charging until 40% of SOC for 100 cycles with the same discharge condition. The experimental data of the capacity is compared with that by simulation using the degradation model, and ion loss from side reaction and lithium plating are plotted, as shown in Figure 4, where the model can predict the capacity fade well. In addition, there is a transition from a linear to a nonlinear range caused by the lithium plating. At the beginning of cycling, ion loss is mainly caused by the side reaction. After 60 cycles, the lithium plating starts to occur and then increases rapidly, which results in the nonlinear and rapid increase of the capacity loss and a transition from the linear to the nonlinear increase.

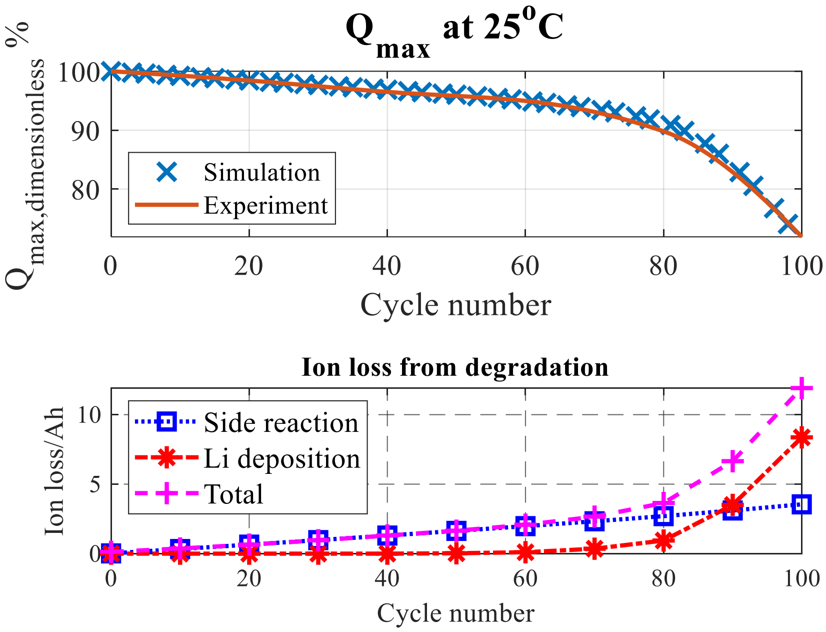

Figure 4. Capacity fade and ion loss at 5C CC charging by side reaction and lithium plating.

This nonlinear transition can be better explained with lithium deposition overpotential during the charging process that is the primary factor for the formation of the lithium plating according to the BV equation. The lithium plating overpotential and lithium plating reaction rate at the particle closely located to the separator as a function of time with different cycle number is plotted in Figure 5 (a) and (b). When cells are getting aged, the overpotential decreases and becomes negative from 60 cycles, which represents the condition for the formation of lithium plating, consequently lithium plating reaction rate decreases. As the cycle number increases, more lithium plating takes place, which results in a rapid and nonlinear drop of the capacity. Particularly, the increase of the overpotential and the decrease of the reaction rate at 100 cycles shortly after 250 seconds is caused by a change of the charging mode from CC to CV because of the degradation and the associated reduced time to reach the cutoff voltage. In addition, because the overpotential is dependent upon the location, the lithium deposition overpotential and the reaction rate at the end of the charging as a function of a location of the particle in the composite anode with different cycle number is plotted in Figure 5 (c) and (d). The closer the location of particles to the separator is, the lower becomes the overpotential, which causes local lithium plating. Moreover, when lithium deposition takes place, deposited metallic lithium covers the surface and pores of particles, so the volume fraction of the active material decreases, especially severely near the separator. As a result, the closer the location of particles to the separator is, the less is the available active area, which increases the magnitude of the overpotential and accelerates the lithium plate as positive feedback. Therefore lithium plating area extends to the opposite direction of the separator.

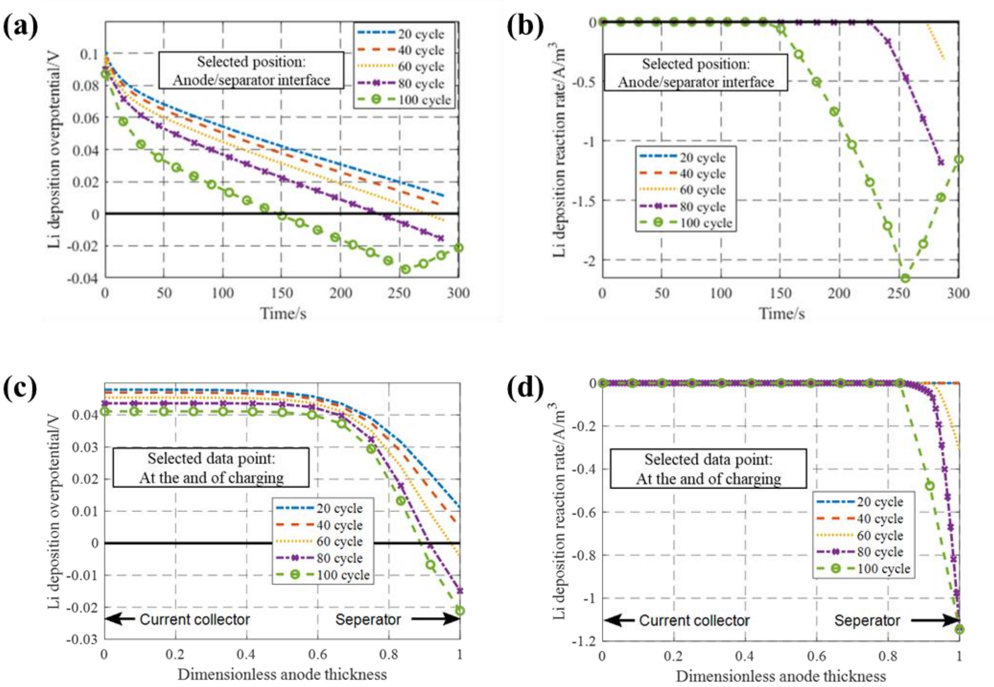

Figure 5. Lithium deposition overpotential and reaction rate during charging as a function of charging time (a), (b), and location in the anode (c) and (d).

In short, the design objective of a charging algorithm should be the reduction of the side reaction rate and prevention of lithium plating so that few ions can be lost, and finally, a capacity fade can be minimized. The preventive measure against the lithium plating inhibits the growth of dendrites, so safer operation can be ensured. Therefore, design objectives have been set to develop a charging algorithm that suppresses the side reaction and prevents the lithium plating.

## 2.4 Design of a new charging method at room temperature

### 2.4.1 Design of a charging algorithm considering side reaction and lithium plating

The limitations of the previously introduced charging method are the side reaction rate and cutoff voltage to minimize the ion loss caused by side reaction [14]. One of the other major causes for degradation is lithium plating directly related to negative lithium deposition overpotential, given by equation (23), which presents a favorable condition for the formation of lithium plating, leading to the loss of ions. In this research, anode potential, which is $\varphi_s - \varphi_e$, used for simplification purposes. In fact, considering anode potential is a more conservative limitation than lithium plating overpotential to reduce degradation comprehensively.

The overall charging process and three limitations for C-rates as a function of SOC are calculated using ROM are plotted in Figure 6 (a), which should minimize the degradation of the cell. The charging starts with the maximum C rate. At every incremented SOC, the designed algorithm checks if the applying C rates cause any variables to reach the three limitations above, which is repeated until a required SOC or a certain preset stop condition, such as cutoff current, are reached. The cutoff current is set as 1/40C.

When charged from 0% SOC with 8C charging current, the first limitation during the low SOC is the anode potential that should not be lower than the zero voltage, and others are the side reaction rate and the terminal cutoff voltage that is 4.2V. Because the high charging current induces extreme heat and hot spots locally that could destroy the thin material in the cell, the maximum charging current is set as 5C. Then at the beginning of life, limitation of anode potential is not considered because limitation of side reaction can always prevent that of anode potential. Based on these constraints, a schematic block diagram of a new fast charging method is depicted in Figure

6 (b). The ROM continuously compares the simulated voltage with that from measurement to follow the internal physical variables of the battery. Any errors caused by the inaccuracy of the ROM and measurements are further improved by a feedback loop with a correction using the EKF. The corrected model is used to estimate surface ion concentrations and anode potentials to estimate SOC, side reaction rate, and lithium plating rate, respectively. In addition, a degradation model is incorporated into the ROM, and its aging parameters are updated as cycled.

As the cycle number increases, the cell gets aged. The aged cell has a decreased volume fraction of electrode and electrolyte that decreases the overpotential, enhancing lithium plating and side reaction. Thus, the side reaction rate increases, and the anode potential becomes negative, which produces more depositions. Consequently, the Ohmic and SEI resistance increase, which causes a fast increase of the terminal voltage that reaches the cutoff voltage of the cell earlier. Therefore, the charging algorithm should be updated as a cell gets aged. Change of allowable C-rate at given SOC by cycle number and the updated relationship between SOC and C-rate after 160 cycles are plotted in Figure 6 (c), where the limitation for anode potential changes more than other limitations as aging progresses. The charging current is primarily limited by the anode potential rather than that of the side reaction rate. Therefore, the anode potential is considered at a low SOC range. Consequently, the limitation for the charging current is divided into three regions, low SOC range by anode potential, middle SOC range by side reaction rate, and high SOC range by the terminal cutoff voltage.

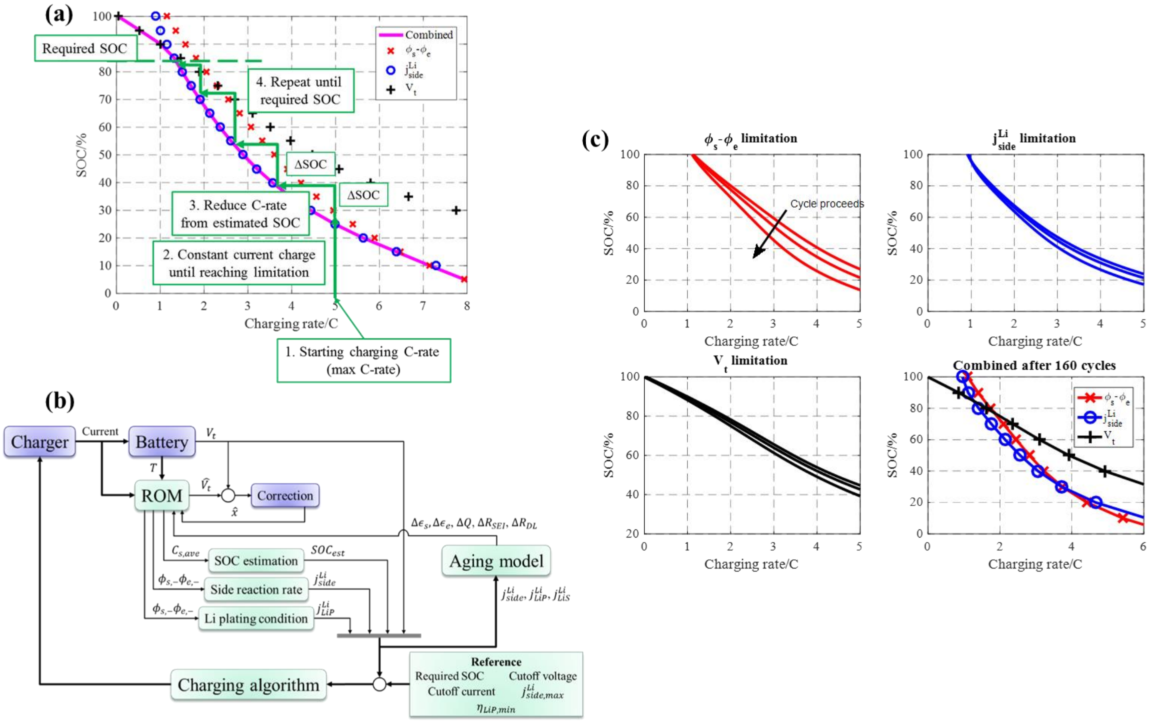

Figure 6. (a) Different limitations for charging C-rates as a function of SOC; (b) Schematic block diagram of fast charging method; (c) Change of SOC and C-rate relationship with aging and updated SOC and C-rate relationship after 160 cycles.

### 2.4.2 Design of a charging algorithm considering lithium stripping

Theoretically, no lithium plating should be formed if the anode potential is larger than 0V. In reality, lithium plating could have been formed from the previous cycling or can be formed from any unknown reasons. For such cases, ideally, lithium stripping enables recovery ions out of plated lithium, which discharge pulse currents can carry out. In order to study the effects of the discharging current, cycling tests with 5C CC, 5C CC, 2C negative pulses (NP) with 20mHz of frequency [44], and 4.3 CC that is the average current of the pulse current are conducted. The current and voltage profile during charging is plotted in Figure 7 (a), where the charging times of

5C CC charging with 2C NP and CC charging with average current are almost identical. The capacity of the three charging methods is measured experimentally and compared with the simulation results from the model, as shown in Figure 7 (b), where simulation results match experimental results well. Because 5C CC charging can charge the battery faster than the other two methods, degradation speed is the fastest. Up to 60 cycles, the capacity loss is dominantly caused by side reaction, and then capacity decreases rapidly because of lithium plating. Comparison between CC charging that has the same average current of the pulse currents and 5C CC with 2C NP has shown that effects of negative pulses are not significant until 100 cycles because lithium plating in the battery charged with average CC charging is not formed yet. When the cycle number is larger than 100 cycles, lithium plating starts to form heavily, and then the negative pulse currents take more effect in recovering ions. At the 160 cycles, the charging algorithm employing negative pulses has accomplished 14% less capacity fade than that by CC charging.

Since the rate of the lithium plating is a function of the lithium deposition overpotential according to the BV equation, the lithium deposition overpotentials from the pulse charging are calculated and plotted over time as a function of cycles in Figure 7 (c). When negative pulses are applied, the overpotentials tend to follow the pulse form of the current profiles and become positive. At the end of 20 cycles, there is a short period of time where the potential becomes negative, where lithium plating starts to form. As cycle number increases, the formation becomes more frequent, but the positive potentials produced by the negative pulse currents promote lithium stripping. The more lithium plating is formed, the more effective becomes the positive pulse that recovers ions. In addition, the stripping takes more effective at low SOC because the overpotential decreases when SOC becomes high.

Ion loss caused by the side reaction and the lithium plating and ion recovery caused by the lithium stripping are calculated using the validated model and plotted in Figure 7 (d). Note that the negative value of the ion loss means ions are recovered. The blue line with square symbols indicates ion loss caused by side reaction, the red line with star symbols is that by lithium plating, the green line with circle symbols is ion recovery by lithium stripping, and the pink line with plus sign symbols is a total sum of ion loss by all reactions. Even though a large number of ions are lost by the lithium plating, negative pulses enable to recover most of them, so the total ion loss using negative pulses is much smaller than that by CC charging with the same average current.

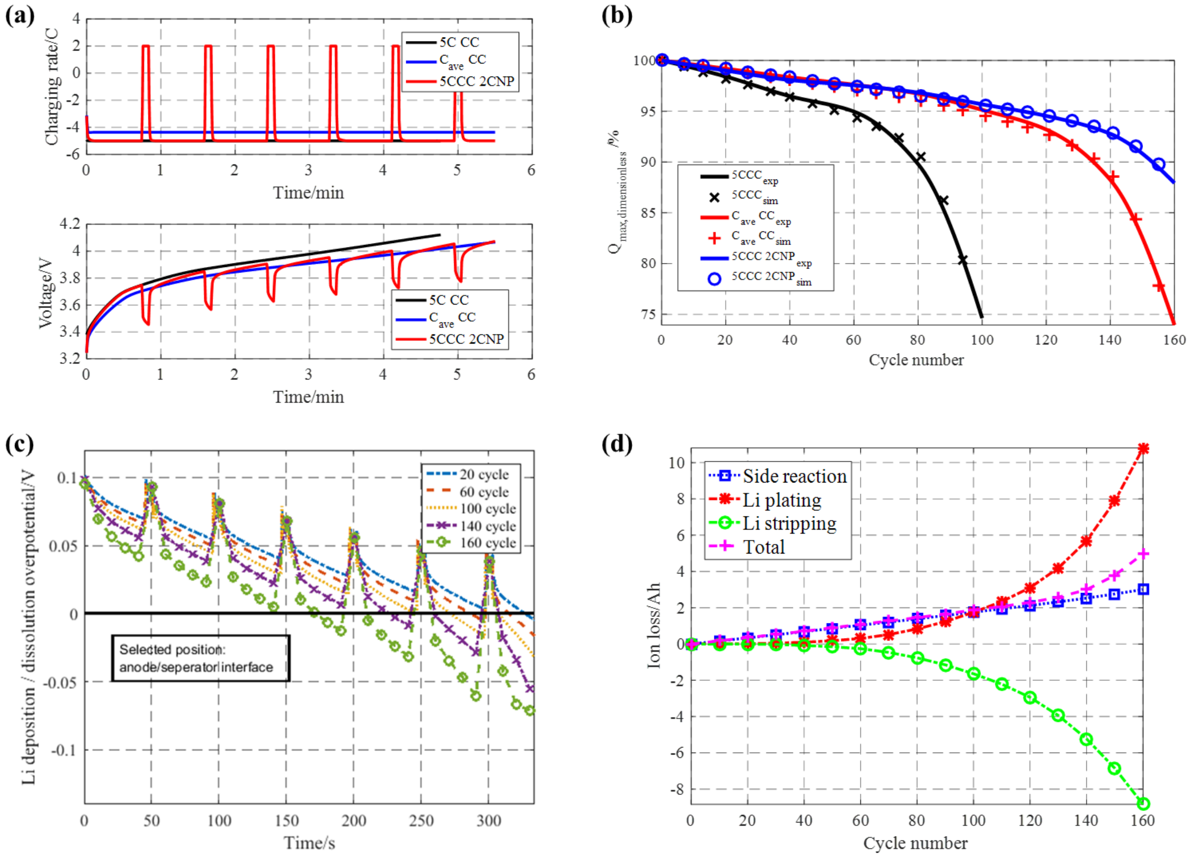

Figure 7. (a) Comparison of charging current and voltage using 5C CC, average CC and 5C CC with 2C negative pulse charging; (b) Experimental and simulated capacity fade with 5C CC, average CC and 5C CC with 2C negative pulse charging; (c) Lithium deposition and dissolution

reaction overpotential during charging 5C CC with 2C negative pulse charging; (d) Ion loss and recovery from side reaction and lithium plating and stripping.

Therefore, adding negative pulses during CC charging reduces degradation using lithium stripping effects without increasing extra charging time. Afterward, a new charging algorithm that combines FC and negative pulse, which is called fast charging with a negative pulse (FCNP), is then designed. The FCNP is implemented in BIL, and its charging time and capacity fade are compared with those of 2C CC/CV and 3C CC/CV charging. The three current profiles and SOC until a cell is fully charged and the measured and simulated capacity loss are plotted in Figure 8 (a) and (b). From the beginning of cycling, the capacity loss by 3C CC/CV charging is always greater than that by FCNP and 2C CC/CV charging and decreases rapidly after 30 cycles, when the lithium plating starts. The proposed FCNP has shown significant improvements. The capacity loss is almost the same as that by 2C CC/CV charging and approximately 23% less than that by 3C CC/CV charging at 60 cycles.

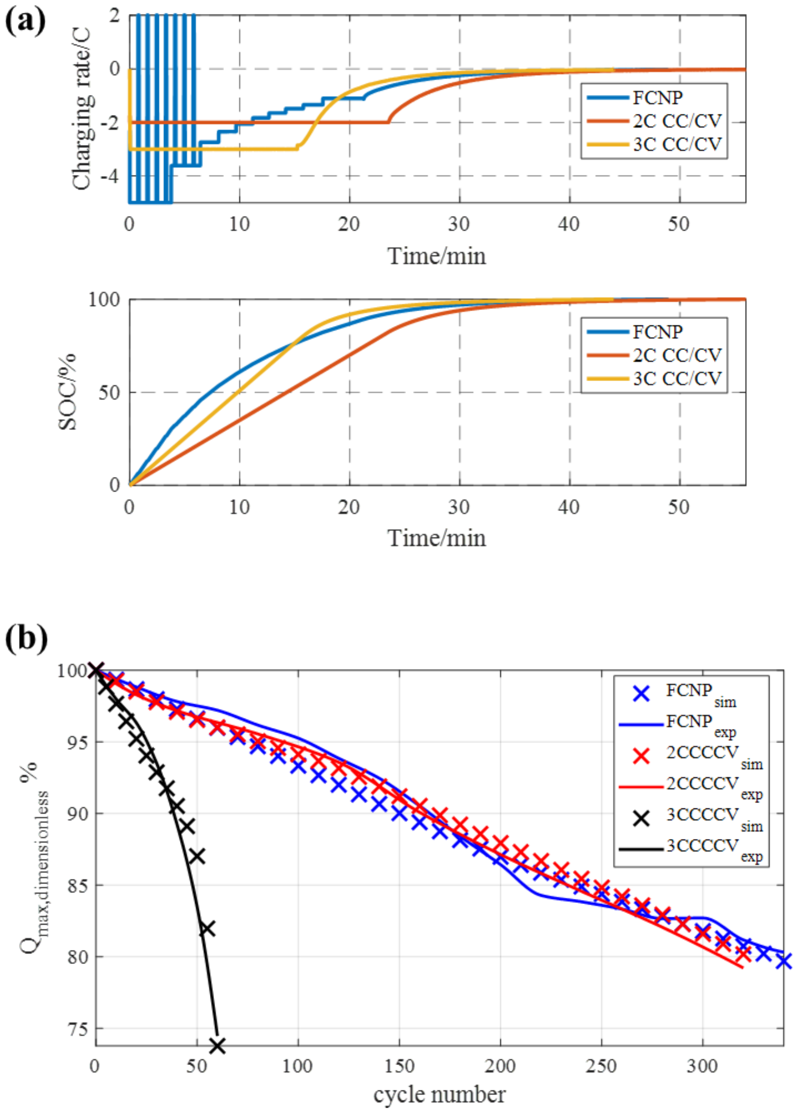

Figure 8. (a) Charging response using FCNP, 2C CC/CV, and 3C CC/CV; (b) Capacity loss by FCNP, 2C CC/CV, and 3C CC/CV.

Analysis of the charging time at different SOC intervals summarized in Table 2 has shown that the charging time by FCNP up to 40% SOC becomes 50% less than that by 2C CC/CV and 31% less than that by 3C CC/CV because of the high charging current at low SOC range, as shown in Figure 8 (a). When charged up to 60% SOC, the charging time by FCNP becomes 43% less than that by 2C CC/CV and 18% less than that by 3C CC/CV. However, because of the low charging current at a high SOC range, the charging time after 80% SOC by FCNP takes longer than that by 3C CC/CV.

Table 2. Charging time at different SOC intervals using FCNP, 2C CC/CV, and 3C CC/CV.

| | 40% SOC | 60% SOC | 80% SOC | 100% SOC |
|---|---|---|---|---|
| FCNP | 5.5 min | 9.7 min | 16.6 min | 49.0 min |
| 3C CC/CV | 7.9 min | 11.8 min | 15.7 min | 44.0 min |
| 2C CC/CV | 11.4 min | 17.1 min | 22.8 min | 56.0 min |

In fact, the charging time by FCNP up to 100% SOC is longer than 3C CC/CV charging at the beginning of life. However, the 3C CC/CV charging exceeds the limitations of charging currents set for lithium plating and side reaction, so degradation is accelerated, and the loss of the capacity becomes larger as the cycle number increases. Since the charging time is affected by the aging process, the charging time up to 100% of SOC by three charging methods is measured and compared in Table 3. As expected, the charging time by 3C CC/CV charging is the shortest at BOL but becomes longer because of fast progress in aging. After 40 cycles, the charging time by FCNP is shorter than two others, while capacity fade can be maintained as that by 2C CC/CV charging.

Table 3. Charing time up to 100% SOC as a function of cycle number.

| | Fresh cell | 20 cycles | 40 cycles | 60 cycles |
|---|---|---|---|---|
| FCNP | 49.0 min | 51.1 min | 51.1 min | 52.0 min |
| 3C CC/CV | 44.0 min | 47.3 min | 53.7 min | 55.2 min |
| 2C CC/CV | 56.0 min | 56.1 min | 56.7 min | 59.2 min |

## 2.5 Summary

In this section, a ROM that embeds both the side reaction and the lithium plating model is developed and validated against experimental data obtained from a large-format pouch-type of lithium-ion battery. The model is used to analyze the mechanism of the cycle life of the lithium-ion battery. In the early stage of cycling, the side reaction is the dominant cause for capacity loss that linearly increases. As the number of cycles increases, the lithium plating takes place, which is the dominant cause for the capacity loss that rapidly increases. Thus, there is a transition of the capacity loss from a linear to a nonlinear range. Therefore, based on the validated degradation model, a charging algorithm is devised to suppress both reactions by limiting side reaction rate and anode potential. In addition, the effect of discharging pulses on capacity loss is experimentally and numerically analyzed. The added negative pulses on the CC charging algorithm promote lithium stripping, which allows for recovering lithium ions from plated lithium. Consequently, the capacity loss can be decreased, and cycle life is extended compared with the classical CC charging algorithm with the same average current as of the pulse current. The negative pulse is particularly effective at the low SOC range, where the amount of ions recovered from plated lithium is large due to the high lithium stripping overpotential. Therefore, fast charging with a negative pulse (FCNP) is developed that minimizes the degradation and increases the safety of a battery system in operation. The algorithm is verified by comparing the cycling results with those from 2C and 3C CC/CV methods. The results have shown that the charging time by FCNP is approximately 50% less than 2C CC/CV charging for the interval from 0% to 40% SOC and 43% for the interval 0% to 60% SOC, while 31% and 18% less than that 3C CC/CV charging for the interval from 0% to 40% SOC and 60% SOC, respectively. Even though the charging time up to 100% of SOC by FCNP is longer than that by 3C CC/CV charging at BOL, it becomes shorter as degradation is in progress, particularly after 40 cycles. On the other hand, the capacity loss by FCNP is comparable to that by 2C CC/CV charging, which is approximately 23% less than that by 3C CC/CV charging after 60 cycles.

# Chapter 3. Development of an accurate electrochemical-thermal model for lithium-ion battery

In the previous chapter, a fast and safe charging algorithm is designed based on the ROM considering degradations. However, the charging algorithm is aimed at only upper temperature, and any heat generated by the battery is not considered. Therefore, in this chapter, an accurate reduced-order electrochemical-thermal model is developed and experimentally validated under a wide range of temperature and current rates. In addition, a detailed analysis of each heat source term is followed.

## 3.1 Literature review of the principle of heat generation

There are various thermal models published. One of the most conventional and straightforward equations to calculate the heat generation rate (HGR) of a battery is as follows [45];

$$\dot{Q} = I \cdot \left(U_{OC} - V_t\right) - I \cdot T \cdot \frac{dU_{OC}}{dT} \tag{34}$$

, where $dU_{OC}/dT$ is an entropy coefficient. The equation has two terms that represent irreversible and reversible heat sources. It allows for the estimation of the HGR based on only three inputs: terminal voltage, current, and open-circuit voltage (OCV). Due to its simplicity and low computation costs, the model is generally preferred for most applications. However, the accuracy of the model is low, and a lumped thermal output does not provide any detailed information relating to the HGR, particularly when considering the location of cell components, heat generation distribution along the thickness direction of the battery cell, and effects of material or internal design changes on the HGR.

The heat generation in a battery can be explained by the first law of thermodynamics. Any differential change of internal energy in a closed system is equal to the sum of heat gained or lost and the work done by the system. The first law can be expressed as follows;

$$dU = dQ - dW \tag{35}$$

, where $dU$ is a change of the internal energy, $dQ$ is a change of the heat that can be added to the system (positive) or given off by the system (negative), and $dW$ is the work done by the system. If some of the reactions induce any pressure or volume changes, the amount of heat exchange is no longer equal to the change of the internal energy because some of the heat is converted into work. Hence, enthalpy as a new property is introduced due to the limitation above, which is defined as the sum of the internal energy and the product of pressure and volume of the system.

$$H = U + PV \tag{36}$$

At a constant temperature, pressure, and volume, the change of the internal energy can be replaced by the change of enthalpy. The change of enthalpy can be further expressed via several terms that are related to enthalpy of reaction, phase change, heat capacity, and enthalpy of mixing [45]. By neglecting the phase change and enthalpy of mixing, the change of enthalpy in a single phase is expressed as follows;

$$\frac{dH}{dt} = IT^2 \frac{d}{dT}\left(\frac{U_{OC}}{T}\right) + mc_p \frac{dT}{dt} \tag{37}$$

The first and second terms on the right side of the equation above represent the change of enthalpy caused by reaction and the change of heat energy of the battery by the change of temperature, respectively. Combining Equation (37) with the first law yields the equation as follows;

$$\frac{dQ}{dt} = \frac{dW}{dt} - IU_{OC} + IT\frac{dU_{OC}}{dT} + mc_p\frac{dT}{dt} \tag{38}$$

, where *dQ/dt* is the heat transfer rate with the surroundings, and *dW/dt* is the electric power of the battery that is generally expressed as the product of terminal voltage and current. Under the assumption that the process is isothermal, the HGR given off to the system is the same as that from the battery. Therefore, the equation above becomes the same as Equation (34), where the sign of the heat transfer rate switches to express the heat released from the battery is positive.

## 3.2 Coupled electrochemical and thermal model

The electric power of the battery in the conventional thermal model is determined only by the product of terminal current and voltage, which does not consider internal chemical reaction processes and detailed prediction of heat distribution in components and the tabs or welds of a cell. Therefore, a detailed formulation is derived.

The internal processes during charging are summarized as a schematic diagram in Figure 9. In this study, only heat generated inside the cell is considered. During charging and discharging, oxidation and reduction processes take place when electrons and ions are involved. Those charges are transported via migration and diffusion that are driven by gradients in potential and concentration, respectively. During charge transport, some of the power from the charger is dissipated due to internal resistances of the battery, and the remaining power is converted to increase or decrease chemical energy of the battery by changing ion concentration in the active materials, which is the actual realized power to the particles.

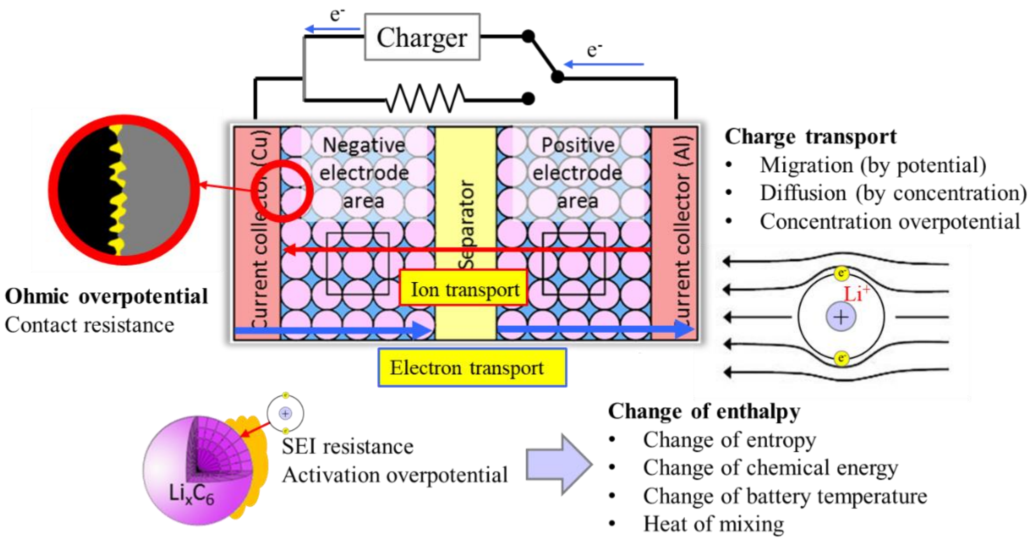

Figure 9. Schematic view of the charging process considering the internal behavior of a cell.

The HGR from the migration of the electrons in the solid phase can be expressed as [46];

$$\dot{Q}_s = \int -i_s \nabla \phi_s dv \tag{39}$$

, where $i_s$ is an averaged current density through the solid phase as expressed [47];

$$i_s = -\sigma^{eff} \nabla \phi_s \tag{40}$$

, where $\sigma^{eff}$ is effective conductivity of active material.

Due to the high mobility of the electrons, the overall magnitude of the HGR is relatively small. However, when the currents flow through interfaces between the current collectors and active material particles in composite electrodes, the current can be concentrated at the area of microcontact spots, where the real contact area is reduced to only a small portion of the nominal contact area. Accordingly, the reduced area increases contact resistance, and the generated heat is expressed as;

$$\dot{Q}_{CR} = I^2 R_{CR} \tag{41}$$

, where $R_{CR}$ is the contact resistance that is experimentally determined from the Ohmic voltage drop during charging and discharging operations [40][48][49].

Similarly, the HGR by ion migration in the electrolyte phase is expressed as;

$$\dot{Q}_e = \int -i_e \nabla \phi_e dv \tag{42}$$

, where $i_e$ is an averaged current density through the electrolyte phase. Due to the lower mobility of the ions, the HGR by electrolyte is relatively large compared to that of the electrode.

On the other hand, most of the charge transport is determined by migration, and as a result, the heat generation from diffusion is negligible. However, the gradient of the ion concentration in the electrolyte induces a concentration overpotential, which decreases the potential across the electrolyte and consequently the current density through the electrolyte phase as follows;

$$i_e = -\kappa^{eff} \nabla \phi_e + \kappa^{eff} \frac{2RT}{F}\left(1 - t_+^0\right) \nabla \ln c_e \tag{43}$$

, where $\kappa^{eff}$ is effective ionic conductivity and $t_+^0$ is transference number. The first and the second terms represent the current density from the potential gradient and that from the concentration overpotential, respectively.

At the surface of the active material, the SEI layer deposited on the active materials of the anode electrode acts as an additional ionic resistance prior to intercalation. The associated HGR is expressed as follows;

$$\dot{Q}_{SEI} = \int j^{Li} V_{SEI} dv \tag{44}$$

, where $V_{SEI}$ is a potential drop across the SEI layer and expressed as;

$$V_{SEI} = \frac{R_{SEI}}{a_s} j^{Li} \tag{45}$$

During the reaction, the activation overpotential generates heat expressed as;

$$\dot{Q}_{act} = \int j^{Li} \eta dv \tag{46}$$

, where $j^{Li}$ is a reaction rate and $\eta$ is the activation overpotential.

Since all reactions take place at the surface of the active materials, the amount of the actual power applied to the active material particle can be expressed using the change of surface ion concentration of the active materials as follows;

$$\dot{W}_{act} = \int j^{Li} U_{eq} \left( c_{s,surf} \right) dv \tag{47}$$

The sum of all equations from (39) to (47) results in the electric power of the battery.

The internal energy of the battery can be rewritten considering reaction rate and heat of mixing, as expressed below;

$$\frac{dU}{dt} = C_p \frac{dT}{dt} - \int j^{Li} T \frac{dU_{OC}}{dT} dv + \int j^{Li} U_{eq} \left( c_{s,ave} \right) dv - \int \left( \overline{H} - \overline{H}^{ave} \right) \frac{\partial c}{\partial t} dv \tag{48}$$

The difference between the actual power and the change of the internal energy based on equations (47) and (48) represents an additional heat generated in the active materials, which yields a new term that expresses the difference of the lithium-ion concentration at the surface of the particle and averaged ion concentration in the particle as follows;

$$\dot{Q}_{concentration} = \int j^{Li} \left[ U_{eq} \left( c_{s,surf} \right) - U_{eq} \left( c_{s,ave} \right) \right] dv \tag{49}$$

Lastly, there is a resistance to mass transport in the battery, which leads to the formation of the concentration gradient as ions are transported. When the current is turned off, the concentration gradients relax, which results in the heat of mixing. Most researchers do not consider the heat of mixing because the magnitude of the heat of mixing is minimal [50]. However, if the heat of mixing is not considered, it is not possible to model the heat that is generated after the current is turned off. For example, when using (34), the HGR becomes zero if the current is zero. In order to derive an equation for the heat of mixing, it is assumed that there are two components in the system and the total enthalpy is a sum of enthalpies of each component as follows [51];

$$H = \int \left( c_A \bar{H}_A + c_B \bar{H}_B \right) dv \tag{50}$$

, where $c$ and $\bar{H}$ are ion concentration and partial molar enthalpy of the components A and B. Partial molar enthalpy is a function of temperature, pressure, and concentration. Then the partial molar enthalpy can be expanded from the 2nd order Taylor series.

$$\begin{aligned} \bar{H}_A &= \bar{H}_{A,ave} + \left.\frac{\partial \bar{H}_A}{\partial c_A}\right|_{ave} \left( c_A - c_{A,ave} \right) + \frac{1}{2} \left.\frac{\partial^2 \bar{H}_A}{\partial {c_A}^2}\right|_{ave} \left( c_A - c_{A,ave} \right)^2 + \left.\frac{\partial \bar{H}_A}{\partial T}\right|_{ave} \left( T - T_{ave} \right) + \left.\frac{\partial \bar{H}_A}{\partial P}\right|_{ave} \left( P - P_{ave} \right) + E\left( \Delta c^3 \right) \\ \bar{H}_B &= \bar{H}_{B,ave} + \left.\frac{\partial \bar{H}_B}{\partial c_A}\right|_{ave} \left( c_A - c_{A,ave} \right) + \frac{1}{2} \left.\frac{\partial^2 \bar{H}_B}{\partial {c_A}^2}\right|_{ave} \left( c_A - c_{A,ave} \right)^2 + \left.\frac{\partial \bar{H}_B}{\partial T}\right|_{ave} \left( T - T_{ave} \right) + \left.\frac{\partial \bar{H}_B}{\partial P}\right|_{ave} \left( P - P_{ave} \right) + E\left( \Delta c^3 \right) \end{aligned} \tag{51}$$

Under the assumptions of constant temperature and pressure, the equations above can be simplified to an equation for the heat of mixing in a single component as follows [52];

$$\dot{Q}_{mix} = \frac{\partial}{\partial t} \left[ \frac{1}{2} \frac{\partial \bar{H}_s}{\partial c_s} \right] \int \left( c_s - c_{s,ave} \right)^2 dv \tag{52}$$

Using the derivative of the partial molar enthalpy, the ion concentration can be rewritten from an enthalpy potential that is defined as the voltage corresponding to reaction [53] and is expressed as enthalpy per the unit of charge, $\partial \bar{H}_s / \partial c_s = -F \, \partial U_H / \partial c_s$ . The enthalpy voltage is further expressed from the Gibbs-Helmholz equation [52].

$$U_H = -\Delta H / nF = U_{OC} - T \frac{\partial U_{OC}}{\partial T} \tag{53}$$

Therefore, the heat of mixing can be calculated from the entropy coefficient and ion concentration as shown;

$$\dot{Q}_{mix} = -\frac{\partial}{\partial t}\left[\frac{1}{2}F\,\frac{\partial\left(U_{OC} - T\,{}^{dU_{OC}}\!\big/_{dT}\right)}{\partial c_s}\right]\int\left(c_s - c_{s,ave}\right)^2 dv \qquad (54)$$

The theoretical calculation of the HGR of a battery requires information on internal variables and parameters of the battery. The internal variables are calculated from a physics-based electrochemical model, and the parameter set for the thermal model is obtained by comparing the electrochemical model prediction to the experimental voltage profiles [54].

### 3.2.1 Measurement of entropy coefficient of pouch-type lithium-ion battery

#### 3.2.1.1 Estimation of Reversible Heat Generation Rate Based on an Empirical Method

Estimation of the reversible HGR requires prior measurement of the entropy coefficient. A battery consists of two electrodes that have different chemistry. Therefore, the entropy coefficient needs to be measured in both electrodes, respectively. However, in commercial cells, it is not always possible to measure a change of potential of each electrode separately. Therefore, in this study, a combined entropy coefficient is measured. There are two major experimental methods to find the entropy coefficient. The first one is a calorimetric method that calculates the difference between total heat generated during charging and discharging [55], which results in a constant value regardless of state-of-charge. Since the entropy of reaction varies significantly with SOC [52], an experiment considering the effect of SOC needs to be conducted. The other experimental method commonly seen is the potentiometric method, which is more accurate but more time-consuming because of the time needed to reach equilibrium.

In this study, an empirical method is applied to estimate the entropy coefficient. The method assumes that the total HGR consists of only reversible and irreversible contributions, while the heat of mixing is neglected. Measurement of the total HGR is carried out in real-time using a calorimeter during charging and discharging at various C-rates. Then, the irreversible HGR is calculated using (34), where the reversible HGR is obtained by subtracting the calculated irreversible HGR from the measured total HGR. The coefficient is then calculated by dividing the reversible HGR by the current and absolute temperature. In this study, the data is collected from 1C, 1.5C, and 2C charging and discharging, and the empirical coefficient is obtained from their averaged results. The result is then compared with the measured entropy coefficient.

#### 3.2.1.2 Measurement of the entropy coefficient

There are two methods to measure the entropy coefficient experimentally depending upon if the battery temperature or SOC is kept constant. The first method involves keeping the temperature constant and measuring voltage by varying SOC at different temperatures. The other method requires keeping SOC constant while varying temperature [50][55][52][56]. Since OCV varies linearly with temperature within the reference temperature of 25°C [55][57] but nonlinearly with SOC, the second method is preferred due to its high accuracy.

The procedure for the measurement of the entropy coefficient is summarized in Figure 10 (a). Initially, a battery is charged or discharged to a target SOC point, which is repeated for 21 points from 0% to 100 SOC with a 5% interval. Then, the battery is rested for at least 10 hours until an equilibrium state is reached. At the equilibrium state, the temperature of the battery is changed using the calorimeter. Figure 10 (b) shows the change of the battery temperature with ±10°C over time, at the temperature change rate of 0.5°C/min. At the same time, the change of terminal voltage due to the temperature change is measured as shown in Figure 10 (c), where the voltage is measured at the 25% SOC point. Then, the entropy coefficient at given SOC can be obtained by linearly fitting the slope of the voltage to the temperature.

The entropy coefficients obtained from two different methods are compared in Figure 10 (d). The blue line is the empirical coefficient, and the red dots and lines are the measured data and fitted curve. The two results show a good agreement except at 0% and 100% SOC. In case of empirical calculation, CC charging and discharging are applied, and the cutoff voltage is reached earlier than 0% and 100% SOC, which results in the inaccuracy of the measurement. Therefore, the measured coefficient is used for the thermal model. It can be assumed that one fitted curve can be used for the other temperature ranges because the slope of the voltage is constant as a function of temperature, as shown in Figure 10 (c). On the other hand, the coefficient is highly dependent on the SOC, and especially at low SOC, it has a high negative value that can cause the reversible HGR to be endothermal and exothermal during charging and discharging, respectively.

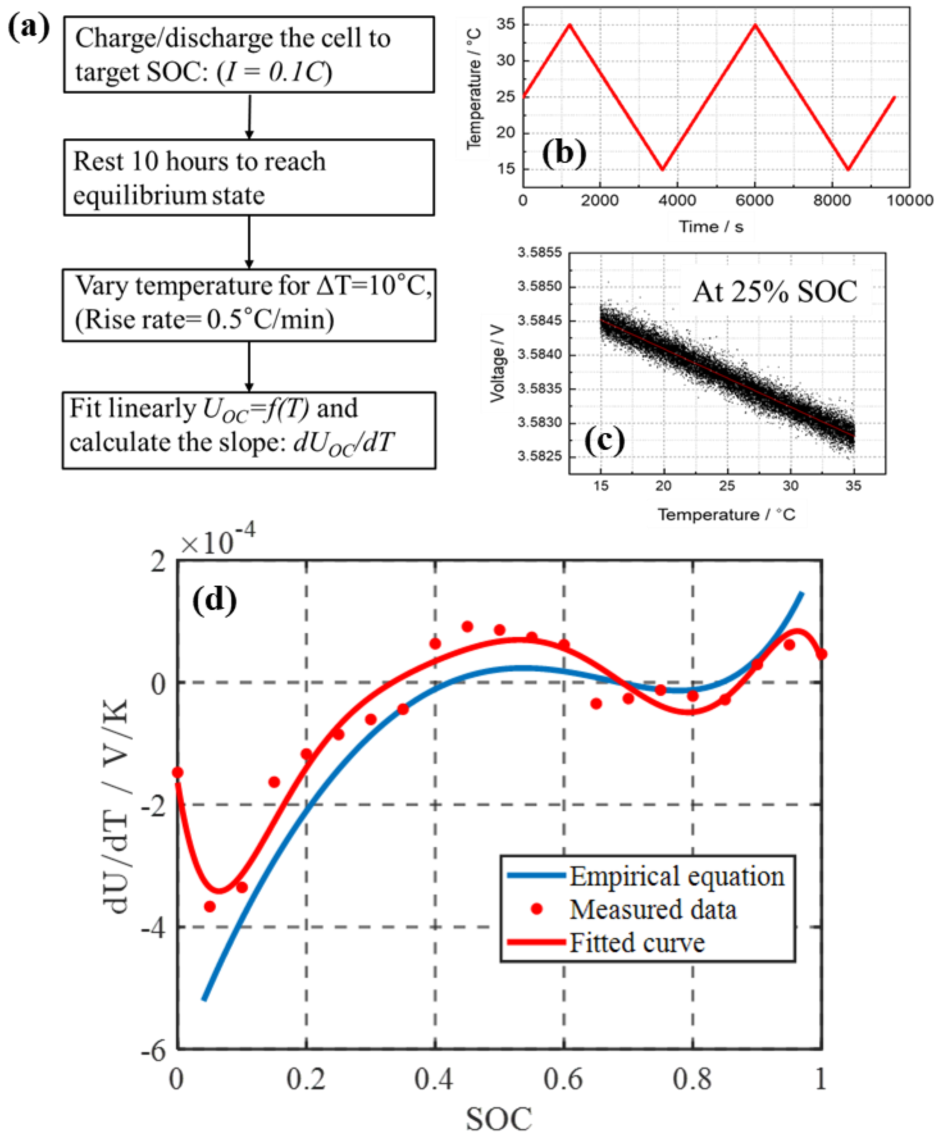

Figure 10. (a) Procedure for the measurement of the entropy coefficient; (b) Change of battery temperature as a function of time; (c) Measured voltage as a function of temperature; (d) comparison of entropy coefficients from the empirical equation and measured data.

### 3.3 Measurement and model validation

Battery temperature is changed by the heat generated and the heat transferred to the surroundings according to the energy equation, which is expressed as;

$$mc_p \frac{dT}{dt} = \dot{Q}_{gen} - \dot{Q}_{transfer} \tag{55}$$

If the battery is operated in an adiabatic condition, the heat transferred to the environment is zero, and all heat generated directly leads to an increase in the battery temperature. If the battery is under isothermal operation, the change of the battery temperature is zero, and all heat generated is transferred to the environment. Therefore, a calorimeter that maintains the surface temperature of the testing cell as constant is required for the measurement of the HGR. The calorimeter is developed using thermal electric modules (TEM) that work as a heat pump and a thermostat at the same time. A testing cell is placed between two TEMs, and its surface temperatures are measured using thermocouples. When the battery generates heat during charging or discharging, the battery generates or absorbs heat, and the battery temperature is changed. Then, the TEM absorbs or releases heat to control the battery temperature to a preset reference in a feedback loop [58]. In this work, it is assumed that the effects of a cross-plane temperature gradient are negligible.

Theoretical calculation of the HGR of a battery requires knowledge of internal variables such as the ion concentration, the potentials in solid and electrolyte phase, or activation overpotential that are immeasurable at the terminal of the battery. For the development of an accurate thermal model, a pseudo-2-dimensional (P2D) ROM is used in this study because a single-particle model (SPM) cannot calculate the gradients of potential and concentration, which is necessary for the study of the heat generation behavior along the thickness direction.

The thermal model including ROM is experimentally validated with respect to HGR using pouch-type LMO (30%) – NMC (70%) / Graphite cell with a capacity of 26Ah under various C-rates and temperatures. The HGRs from experiments and simulations at 25°C during charging and discharging with different C-rates are compared in Figure 11 (a) and (b), and those during 1C discharging at different temperatures are compared in Figure 11 (c) and (d). Generally, the HGRs during charging are smaller than those during discharging at the same C-rate. Besides, the profiles of the HGR from 15°C to 45°C are similar but rapidly increase when the temperature is below 0°C. A detailed analysis of the effect of C-rate and temperature will be discussed in the next section.

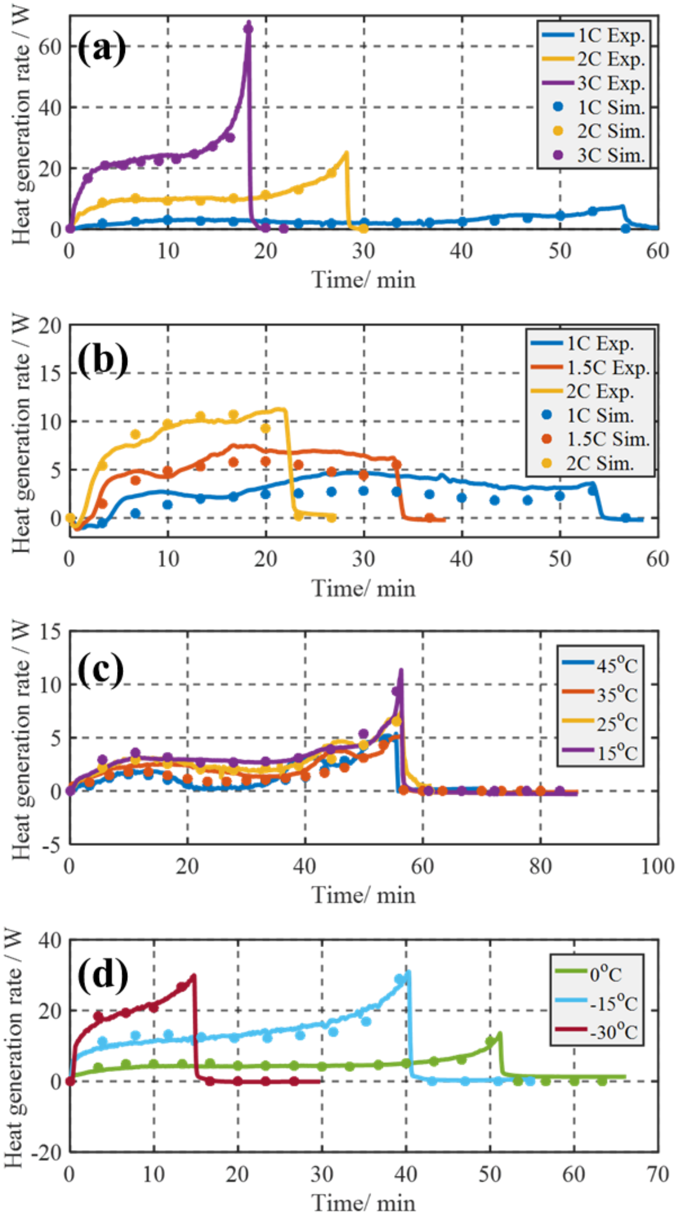

Figure 11. Heat generation rate from experiments and simulation; (a) from 1C to 3C discharging at 25°C; (b) from 1C to 2C charging at 25°C; (c) from 45°C to 15°C during 1C discharging; (d) from 0°C to -30°C during 1C discharging.

The corresponding root-mean-square (RMS) errors of the simulation data are calculated and summarized in Table 4 and Table 5. The overall profiles of the HGR from the simulation are in good agreement with those from experiments. However, the difference between the simulated and measured heat generation rate tends to increase at high C-rates or low temperatures, which can be caused by the neglected cross-plane temperature gradient from the measurements and the assumptions of the model. In addition, another reason for the difference at low temperatures is the neglected temperature dependency of the entropy coefficient.

Table 4. RMS errors of heat generation rates at 25°C.

| C-rate (1/h) | 1C Disch. | 2C Disch. | 3C Disch. | 1C Ch. | 1.5C Ch. | 2C Ch. |
|---|---|---|---|---|---|---|
| RMSE (W) | 0.74 | 1.52 | 3.87 | 1.30 | 0.74 | 1.39 |

Table 5. RMS errors of heat generation rates at 1C discharging.

| Temp. (°C) | 45 | 35 | 25 | 15 | 0 | -15 | -30 |
|---|---|---|---|---|---|---|---|
| RMSE (W) | 0.59 | 0.71 | 0.74 | 0.70 | 1.12 | 2.28 | 2.99 |

### 3.4 Analysis of heat source terms under various conditions

The detailed heat sources, including the heat from charge transport, overpotentials, and reversible entropic heat, are compared during both charging and discharging. The profiles of the HGR from each heat source during 2C CC charging and discharging at 25°C are plotted in Figure 12 as a function of time and SOC. The most significant heat sources are; 1) change of the entropy, 2) migration from the electrolyte phase, 3) contact resistance, and 4) difference of surface and averaged ion concentration within particles. Each heat source has a different magnitude and tendency as a function of SOC.

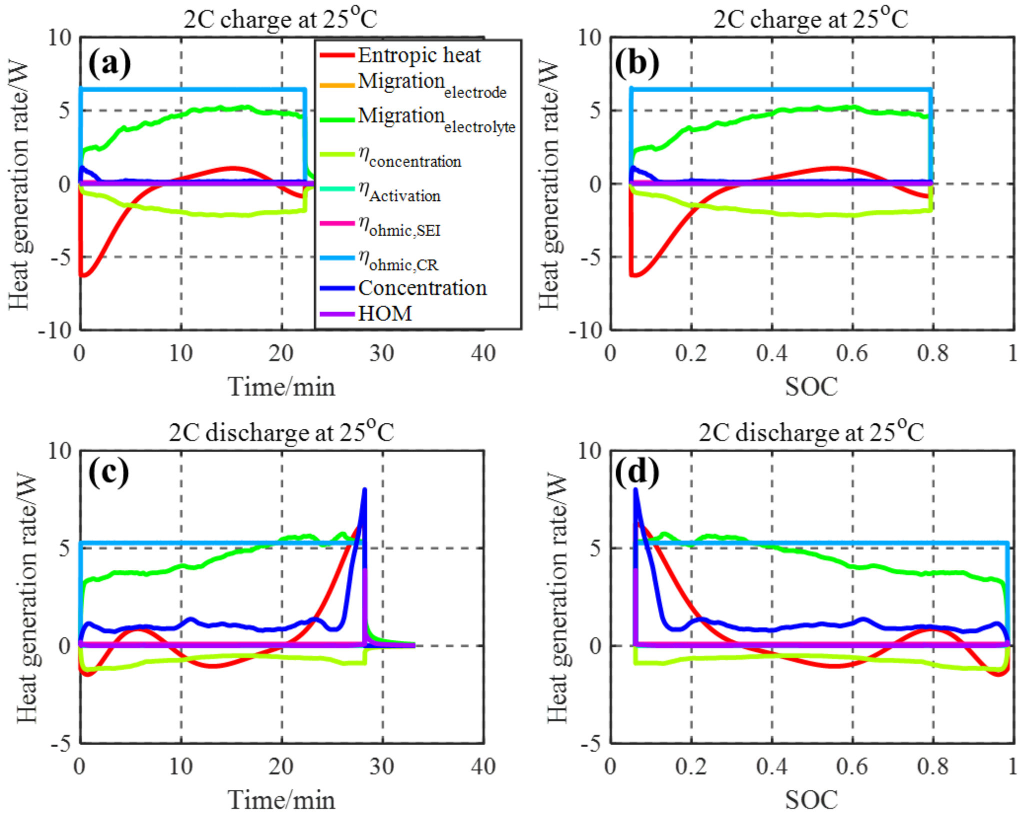

Figure 12. Heat sources during 2C CC at 25°C; (a) charge as a function of time; (b) charge as a function of SOC; (c) discharge as a function of time; (d) discharge as a function of SOC.

As seen in Figure 12, the entropic HGR is highly dependent on SOC and mirrored at charging and discharging because of its reversible nature. Additionally, the HGR from the electrolyte phase is much larger than that from the electrode phase because of the different mobility of charges. However, it is reduced by the concentration overpotential, and accordingly, the sign of the HGR resulting from the concentration overpotential is negative. Due to different chemistries composing the anode and cathode active materials, the magnitudes of the HGR by migration during charging and discharging are different at a given C-rate. The HGR by the contact resistance has the same profile as that of the current, which dominantly contributes to the total HGR. Lastly, the HGR by the difference of ion concentration within particles is also dependent on SOC, and its magnitude is seen to be the largest, especially at low SOC during discharging. In fact, impedances measured by EIS have shown that the charge transfer resistance of the cell is the largest when the voltage is at 0% SOC [59]. In addition, the internal cell resistance is dependent upon charging and discharging, and the resistance during discharging is larger than that during charging [60]. There are other negligible heat sources such as the activation overpotential, SEI resistance at the Beginning of Life (BoL), and the heat of mixing.

The total irreversible HGRs during 1C charging and discharging for each component are plotted in Figure 13 (a) and (b) under the assumption that the contact resistance at the interface of the anode electrode and current collector is the same as that of the cathode electrode and current collector. The magnitude of the HGR from the cathode electrode for both charging and discharging has a peak at a low SOC where the difference of ion concentration within particles is larger, which leads to a large potential difference. At the anode electrode, the potential does not significantly change with the ion concentration. At the separator, the SOC dependency of the HGR is similar, and the magnitude is small because the only heat generated is due to ion transport. The ratio of the magnitude of each heat source to the total heat at the anode and cathode is compared in Figure 13 (c) and (d), where the heat from concentration overpotential (yellow) is negative. At the anode electrode, the heat from the contact resistance is dominant with the addition of the heat from SEI resistance, which is unique to the anode electrode. In addition, the heat from the difference in ion concentration within particles is not significant. However, at the cathode electrode in Figure 13 (d), the heat from the difference in ion concentration is a significant heat source. The migration heat at the electrolyte phase is also a dominant heat source, although some amount of heat is reduced by the concentration overpotential. Other heat sources, such as migration from the electrode, activation overpotential, and heat of mixing, are small enough to neglect.

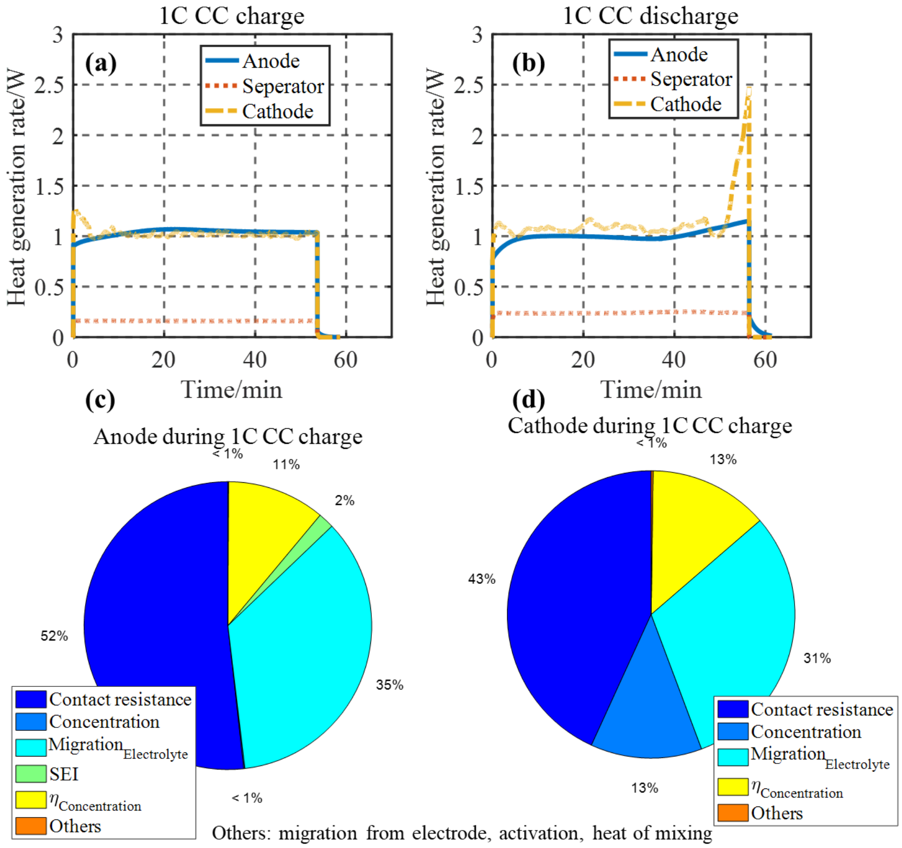

Others: migration from electrode, activation, heat of mixing

Figure 13. Irreversible heat generation rates at each component; (a) during charging; (b) during discharging; the ratio between heat sources and the total heat during 1C CC charge; (c) at anode electrode; (d) at cathode electrode.

### 3.4.1 Effect of the C-rates on the heat generation rates

In order to analyze the effects of C-rates, the total heat is calculated, which provides a reference for the calculation of efficiency during operations. The total heat during charging and discharging at 35°C is plotted as a function of C-rates in Figure 14 (a). When the C-rate increases, Joule heating, which is the main heat source in the battery, increases proportionally to the square of applied current, but the charging or discharging time decreases. As a result, the total heat increases almost linearly as the C-rate increases. In addition, the total heat at charging is always smaller than that at discharging at the given C-rate because of the contribution of the reversible heat. In Figure 14 (b), the ratio of the heat from each source to the total heat during charging and discharging is compared as a function of C-rates. The entropic heat is seen to be the largest at a low C-rate but rapidly decreases as the C-rate increases. In addition, the profiles at charging and discharging are similar but mirrored because of the reversible process, which is the reason for higher heat during discharging. On the other hand, the irreversible heat sources have a similar trend regardless of charging and discharging. Those heat sources are small at a low C-rate but become dominant as the C-rate increases because of the overpotentials [61]. Above 1.5C, the ratio of irreversible heat sources is seen to be relatively constant because the increasing rates of irreversible heat sources are identical.

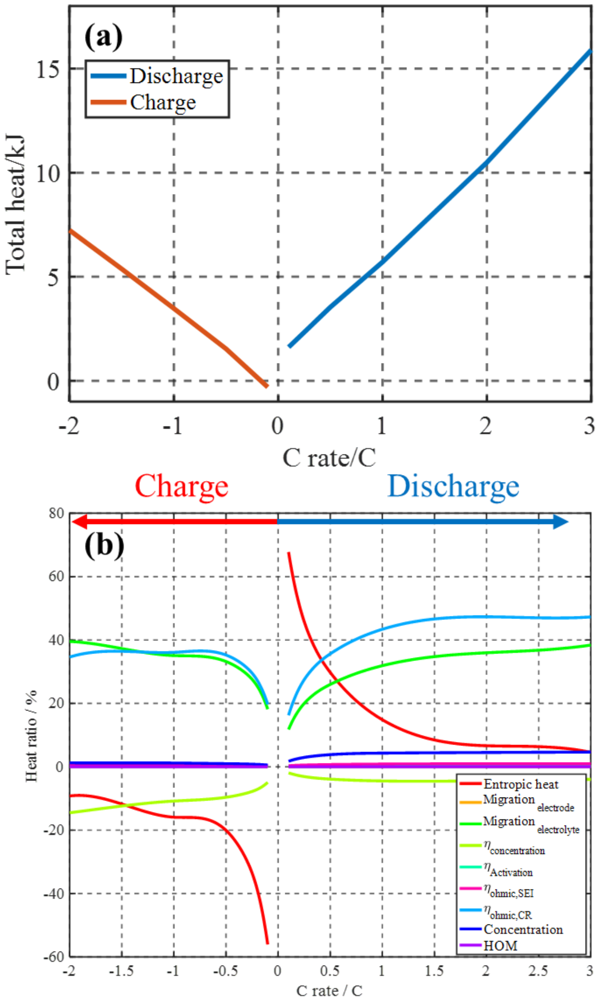

Figure 14 (a). Total heat as a function of the C-rate from both charging and discharging at 35°C; (b). The ratio of the heat of each source over the total heat as a function of the C-rate.

### 3.4.2 Effect of temperature on the heat generation rate

Since the temperature of a battery can vary during operation, the effect of the operating temperature on the HGR is analyzed with the validated model. For the analysis, the results during discharging are compared due to the higher HGR compared to charging. Different heat sources during 1C CC discharging at different temperatures are plotted in Figure 15. The results have shown that the most dominant heat source at high temperatures is the change of entropy because the battery internal resistance is small at high temperatures, which leads to a small irreversible HGR. On the other hand, the contribution of the contact resistance, ion concentration difference within particles, and ion migration to the overall heat generation rate rapidly increases at low temperatures. The area of microcontact spots of the interface between active material particles and current collectors is caused by a deformation of materials, which is directly related to the strength of the material. At low temperatures, the material strength increases, and the deformation is reduced. Accordingly, the contact area is reduced, and the contact resistance increases [62]. In addition, the gradient of ion concentrations in particles increases the charge transfer resistance at low temperatures [59]. Ion transport at low temperatures gets hindered, and the heat generation rate increases. However, some amount of heat is reduced by concentration overpotential.

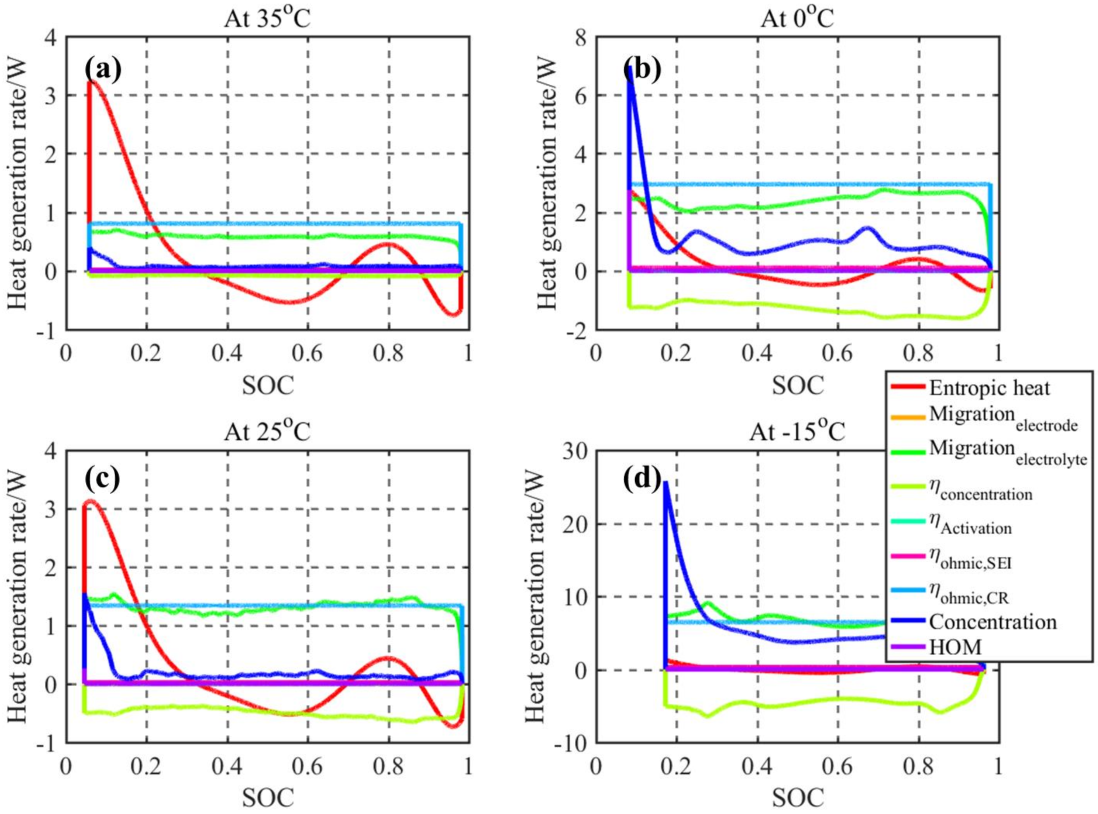

Figure 15. Heat sources during 1C CC discharge; (a) at 35°C; (b) at 0°C; (c) at 25°C; (d) at -15°C.

The two most dominant irreversible heat sources at low temperatures are plotted in Figure 16 (a) and (c). Since the HGR by the contact resistance follows the same profile as the applied current, only the magnitude of the HGR is plotted as a function of temperature. In addition, the magnitude of the HGR due to the SEI resistance is plotted in Figure 16 (b) and is seen to increase rapidly at low temperatures even though the HGR is small enough to neglect at the beginning of life. Both resistances exponentially increase at low temperatures.

The discharging time is also significantly affected by the operating temperature. Therefore, it is more effective to compare results as a function of SOC. The HGR caused by the difference in the ion concentration within the particles is plotted at various temperatures in Figure 16 (c). The overall HGR increases as temperature decreases. However, the peak HGR at -30°C is smaller than that at -15°C because the same terminal voltage cutoff occurs at a higher SOC at lower temperatures because of a larger ohmic overpotential at low temperatures, which results in the smaller peak.

The entropic HGRs at various temperatures are plotted in Figure 16 (d), where a consistent trend in the entropic HGR is seen. In this study, the entropy coefficient is measured at 25°C as a reference temperature and used for all temperature ranges. As a result, the absolute temperature does not affect the overall HGR significantly at the given C-rate. On the other hand, at low temperatures, the voltage reaches the cutoff voltage earlier due to increased ohmic overpotential. Therefore, the total heat decreases at lower temperatures due to the reduced discharging time.

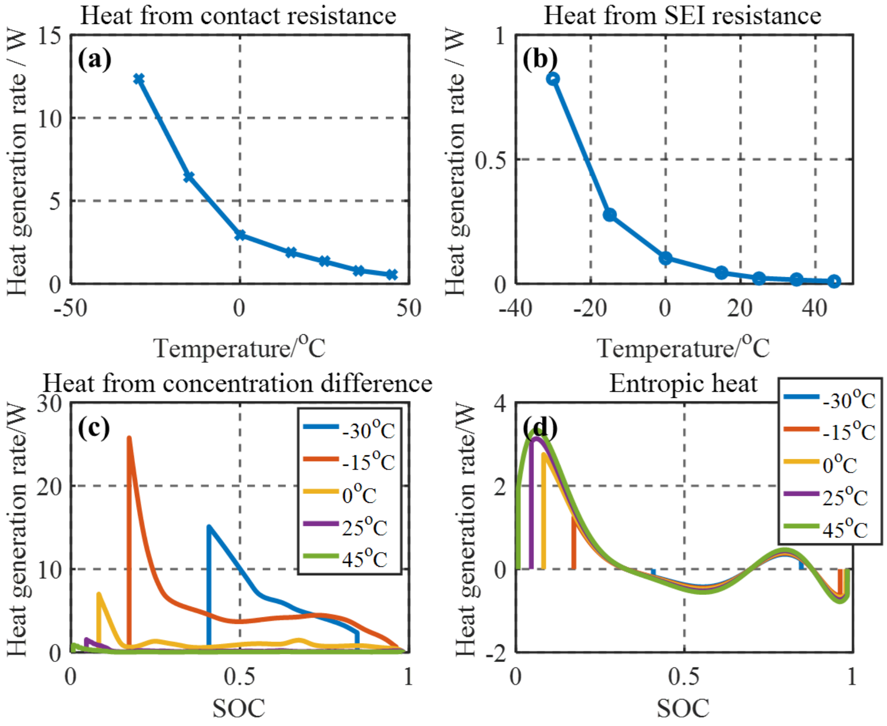

Figure 16. Heat generation rate at different temperatures (a) heat from contact resistance; (b) heat from SEI resistance; (c) heat from ion concentration difference within particles; (d) entropic heat as a function of SOC.

### 3.4.3 Temperature distribution through the plane of a single cell

The thermal model previously introduced assumed that a microcell represents a single cell. In fact, a single cell is composed of multiple microcells that are connected in parallel. Therefore, the validated thermal model for a microcell is extended to predict temperature profiles through the plane of a single cell, which schematic diagram is depicted in Figure 17. In this study, the number of anode and cathode electrodes is 20 and 19, respectively. Besides, it is assumed that the reactions taking place at all microcells are identical, and there are thermal contact resistances between separators and electrodes. The value of thermal contact resistance is assumed to be 80% of total thermal resistance in this study [63][64]. The dimensions and thermal properties of each component are summarized in Table 6.

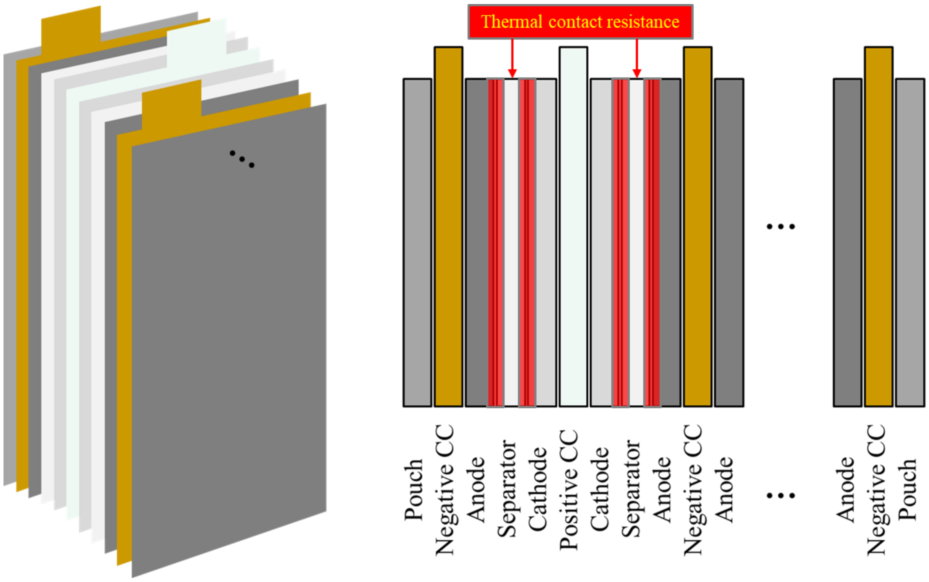

Figure 17. Schematic diagram of a single cell.

Table 6. List of model parameters.

Electrochemical parameter (a: manufacture; b: model validation).

| | Negative electrode | Separator | Positive electrode | Unit |
|---|---|---|---|---|
| Thickness[a], $\delta$ | $66 \times 10^{-6}$ | $31 \times 10^{-6}$ | $73 \times 10^{-6}$ | m |
| Particle radius [65], $R_S$ | $8 \times 10^{-6}$ | - | $9.8 \times 10^{-6}$ | m |
| Stoichiometry at 0%[b] SOC | 0.28 | - | 0.84 | |
| Stoichiometry at 100%[b] SOC | 0.92 | - | 0.46 | |
| Average electrolyte concentration, $c_e$ | $1.2 \times 10^3$ | $1.2 \times 10^3$ | $1.2 \times 10^3$ | mol $m^{-3}$ |
| Exchange current density coefficient, $i_0$ | $13.2 \times 10^4$ | - | $6.79 \times 10^4$ | A $m^{-2}$ |
| Charge transfer coefficient, $\alpha_a$, $\alpha_c$ | 0.5, 0.5 | - | 0.5, 0.5 | |
| Solid phase diffusion coefficient[b], $D_s$ | $2.28 \times 10^{-13}$ | - | $1.04 \times 10^{-13}$ | $m^2$ $s^{-1}$ |
| Solid phase conductivity, $\sigma$ | 5.4 | - | 0.2 | S $m^{-1}$ |
| Bruggeman’s porosity exponent, $p$ | 1.5 | 1.5 | 1.5 | |

| | | | | |
|---|---|---|---|---|
| Electrolyte phase ionic conductivity, $\kappa$ | $\kappa = 15.8c_e \exp(-13472c_e^{1.4})$ | | | S m$^{-1}$ |
| Li$^+$ transference number, $t_0^+$ | 0.363 | 0.363 | 0.363 | |
| Equilibrium potential of anode | $U_{eq-}(x) = 8.00229 + 5.0647x - 12.578x^{0.5} - 8.6322 \times 10^{-4}x^{-1} + 2.1765 \times 10^{-5}x^{-1.5} - 0.46016\exp\big(15 \times (0.06 - x)\big) - 0.55364\exp(-2.4326 \times (x - 0.92))$ | | | |

Thermal parameter [66].

| Components | Material | Density [g/cm$^3$] | Heat capacity [J/g K] | Conductivity [W/cm K] |
|---|---|---|---|---|
| Negative CC | Copper | 8.96 | 0.386 | 3.97 |
| Anode | Graphite | 2.1 | 0.71 | 0.1511 |
| Separator | Microporous polymer | 1.4 | 1.551 | 0.0035 |
| Cathode | LMO – NMC | 4.89 | 0.85 | 0.00687 |
| Positive CC | Aluminum | 2.7 | 0.9 | 2.3 |
| Pouch | Aluminum/PET/PPE/Nylon | 1.7 | 1.15 | 0.61 |

In addition, forced air convection is assumed at both surfaces, where the convection coefficient is set as 30W/m$^2$K [67]. Discharging current and temperature profiles for the single cell level during 2C CC discharging at 25°C are calculated and plotted in Figure 18 (a), (b), and (c). The temperature profile is symmetric due to the symmetrical structure and HGR profile. Small ripples in the profile through the plane are caused by thermal contact resistance as well as different HGR profile and thermal properties of the components.

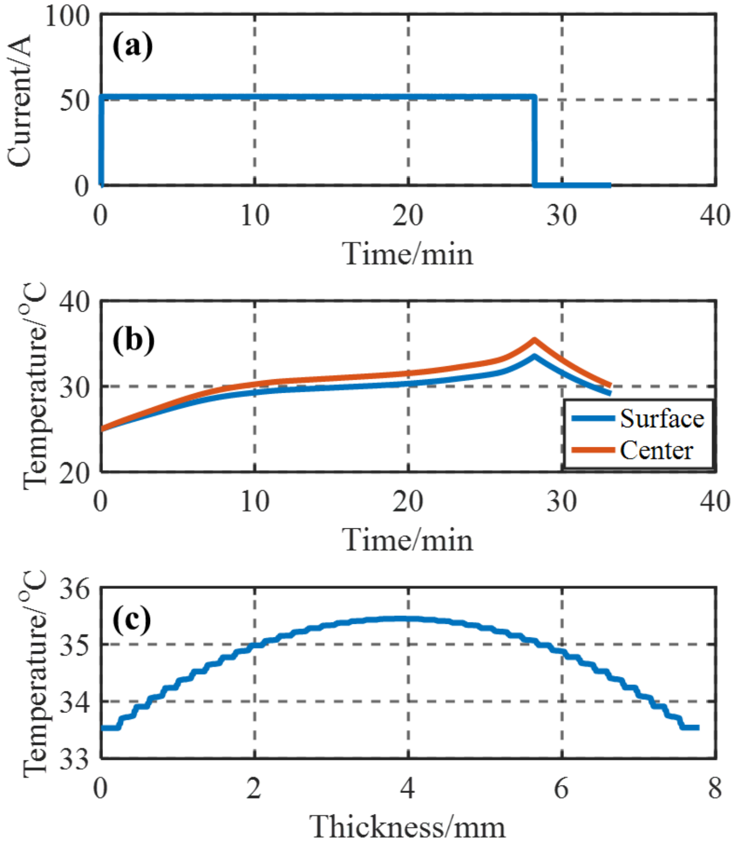

Figure 18. Simulation results at 2C CC discharging; (a) Current profile; (b) Temperature profile through the plane of the single cell vs. time; (c) Temperature profile at the end of discharging through the thickness direction.

## 3.5 Design of parameter identification procedure

### 3.5.1 Challenging issue of the electrochemical thermal model.

Even though the above results have shown accurate estimation of the heat generation rate with detailed heat source terms, one of the challenging issues for the electrochemical thermal model is a large number of parameters and complex identification procedure for the parameters. The battery parameters for the electrochemical-thermal model can be categorized into geometric and electrochemical properties. The geometric parameters consist of a thickness of electrodes, volume fraction, or particle radius that can be measured by disassembling cells. The thickness of electrodes can be measured by a micrometer screw [69] or electron microscopy [70], and the volume fraction and particle radius can be measured by mercury porosimetry [69][70]. Besides, the electrochemical parameters represent those related to ion concentration or transport properties, where coin half cells are used to investigate the individual parameters for each electrode and various techniques are applied, such as Electrochemical Impedance Spectroscopy (EIS) for battery dynamics and electrode interface information, or Galvanostatic Intermittent Titration Techniques (GITT) for diffusion coefficient [71]. The accuracy of the measurements has been validated with voltage profiles calculated by the electrochemical model [72]. However, the methods are time-consuming and require equipment for the experiment. Therefore, there is a need to develop a fast and non-destructive method for parameter identification, where the identifiability of parameters investigated by a sensitivity analysis can be advantageous for the design of the non-destructive method.

### 3.5.2 Parameter sensitivity analysis

The sensitivity analysis is a method to evaluate the influence of the variance of parameters on the model output, and a proper sensitivity analysis helps the parameter identification by excluding insensitive parameters. The sensitivity analysis can be categorized into two methods that are analytical and simulation-based. Firstly, in case of an analytical method, the partial derivative of the terminal voltage over the parameters and the Fisher information matrix (FIM) are generally used to calculate expected variances and output sensitivities, where the terminal voltage calculated by the electrochemical model, such as SPM [73] or Doyle-Fuller-Newman model [74], is utilized for the output. Since the FIM represents the identifiability and depends on an input signal, the input signal can be optimized to maximize the FIM [75]. The analytical method can offer an accurate range of parameters, but the calculation time of FIM is complicated for high-order models [77]. In addition, the model output is limited and nonlinear outputs cannot be used, such as internal variables or the HGR. Secondly, the simulation-based method utilizes simulation outputs with the change of input parameters, which enables the analysis of nonlinear outputs that cannot be conducted by the analytical method. The method can be further divided into two methods, which are local and global. In case of the local methods, one of the most commonly used methods is the one-factor-at-a-time (OFAT) method [76], where only one parameter is varied for the model output while other parameters are kept at their nominal values. This method is able to provide the impact of parameters on the model output straightforwardly.

On the other hand, the global methods, such as Monte Carlo or variance-based methods [79], consider sensitivity over the whole input space and quantify the model output variation in the entire parameter domain. Although it can comprehensively analyze individual and coupled effects of parameter variations [78], its computational load is extremely large, and parallel computing is required [80]. Therefore, in this study, the OFAT method is used because of its straightforward solution and less computational cost.

There are various studies of the OFAT-based sensitivity analysis, where various model outputs are considered, such as cell temperature [68][81], capacity [82], SOC, and anode potential [77]. However, none of the papers have conducted a sensitivity analysis with respect to the HGR of the battery. Since the temperature is affected by the ambient environment and the analysis using the temperature cannot exclude this effect, the accuracy of the analysis is not high. Therefore, a comprehensive analysis of the HGR is conducted to achieve higher accuracy.

For the sensitivity analysis, parameters that can contribute to the internal processes of the battery are surveyed, and 23 parameters are selected. The parameters are listed in Table 7, where they are categorized into four groups based on geometry, concentration, transport, and kinetic properties. The geometric parameters are the thickness of electrodes, volume fraction, and particle radius, while the concentration parameters consist of the maximum ion concentration within active material particles. The transport parameters are related to the charge transfer, such as conduction coefficient, diffusion coefficient, Bruggeman coefficient, transference number, and exchange current density coefficient. Lastly, the kinetic parameters consist of resistance sources, such as the contact resistance and the SEI resistance. Based on the data given by the literature, reasonable boundaries of each parameter are determined, where the parameters out of a normal value are dropped, and relatively equivalent ranges of parameters with those of other parameters are considered in the same category in order for accurate comparison. In case of the entropy coefficient, it is not considered in the analysis and further identification because it is not constant but varies as a function of SOC.

Table 7. List of parameters and ranges for sensitivity analysis.

| Category / Parameter | | Description | | | Reference | Boundaries | Unit |
|---|---|---|---|---|---|---|---|
| Geometry | $L$ | Thickness | | Cathode | 60 [86], 70 [90], 73 [65], 74 [87], 78 [92], 79 [89] | 50 - 90 | $\mu m$ |
| | | | | Separator | 20 [86][92][93], 25 [87] [89] [91], 29 [65] | 10 - 30 | |
| | | | | Anode | 62 [87], 63 [90], 66 [65], 67 [89], 81 [92], 90 [86] | 65 - 100 | |
| | $\epsilon$ | Volume fraction | Solid | Cathode | 0.38 [87], 0.44 [88], 0.616 [65] | 0.4 - 0.65 | – |
| | | | | Anode | 0.357 [88], 0.45 [87], 0.572 [65] | 0.4 - 0.6 | |
| | | | Electrolyte | Cathode | 0.26 [65], 0.27 [93], 0.281 [92], 0.296 [69], 0.33489 [86], 0.35 [90], 0.45 [87] | 0.23 - 0.4 | |
| | | | | Separator | 0.39 [65], 0.4 [93], 0.46 [92], 0.49924 [86], 0.508 [69], 0.55 [87] | 0.4 - 0.55 | |
| | | | | Anode | 0.26 [65], 0.264 [92], 0.329 [69], 0.33 [90], 0.33438 [86], 0.34 [93], 0.5 [87] | 0.23 - 0.4 | |

| | | | | | | | |
|---|---|---|---|---|---|---|---|
| | $R$ | Particle radius | | Cathode | 1.2 [90], 5 [92] [93], 6.5 [69], 7 [89], 9.8 [65] | 1-11 | $\mu m$ |
| | | | | Anode | 5 [91], 8 [65], 8.7 [69], 10 [92] [93], 11 [89] [90] | 1-11 | |
| Concentration | $c_{s,max}$ | Maximum ion concentration | | Cathode | $4.9242\cdot10^{4}$ [89], $4.95\cdot10^{4}$ [91] [96], $5.15\cdot10^{4}$ [87] | $4.8\cdot10^{4}$-$5.2\cdot10^{4}$ | $mol\,m^{-3}$ |
| | | | | Anode | $2.9862\cdot10^{4}$ [89], $3.0555\cdot10^{4}$ [96], $3.09\cdot10^{4}$ [91], $3.137\cdot10^{4}$ [87] | $2.9\cdot10^{4}$-$3.3\cdot10^{4}$ | |
| Transport | $\sigma$ | Conductivity | | Cathode | $0.038\cdot10^{2}$ [93] [94], $0.1\cdot10^{2}$ [86] [91] | $0.05\cdot10^{2}$-$0.2\cdot10^{2}$ | $S\,m^{-1}$ |
| | | | | Anode | $1\cdot10^{2}$ [86] [91] [93] [94] | $0.5\cdot10^{2}$ - $2\cdot10^{2}$ | |
| | $D$ | Diffusion coefficient | Solid | Cathode | $2\cdot10^{-14}$ [91], $3\cdot10^{-14}$ [87] [92], $3.97\cdot10^{-14}$ [86], $4.0\cdot10^{-14}$ [65], $8\cdot10^{-14}$ [96], $1\cdot10^{-13}$ [88] | $10^{-14}$ – $10^{-13}$ | $m^2s^{-1}$ |
| | | | | Anode | $1.6\cdot10^{-14}$ [92], $2\cdot10^{-14}$ [86], $3\cdot10^{-14}$ [87], $3.9\cdot10^{-14}$ [88], $7.5\cdot10^{-14}$ [65], $8.8\cdot10^{-14}$ [96] | $10^{-14}$ – $10^{-13}$ | |
| | | | Electrolyte | | $1.5\cdot10^{-10}$ [91], $2.4\cdot10^{-10}$ [69] [86], $1.5\cdot10^{-10}$ - $7.5\cdot10^{-10}$ [99] | $1.5\cdot10^{-10}$ –$5\cdot 10^{-10}$ | |
| | $p$ | Bruggeman coefficient | | | 1.5 [86] [91] | 1.3 - 1.7 | – |
| | $t_0^+$ | Transference number | | | 0.26 [69], 0.363 [86], 0.38 [87] | 0.25 - 0.4 | – |
| | $i_0$ | Exchange current density coefficient | | Cathode | $6.28\cdot10^{4}$ [95], $6.79\cdot10^{4}$ [100] | $5\cdot10^{4}$ - $8\cdot10^{4}$ | $A\,m^{-2}$ |
| | | | | Anode | $12.9\cdot10^{4}$ [95], $12\cdot10^{4}$ [92], $13.2\cdot10^{4}$ [100] | $10\cdot10^{4}$ - $14\cdot10^{4}$ | |
| Kinetics | $R_{CT}$ | Contact resistance | | | 0.7 [98], 1.6 [101], 1.9 [40] | 0.7 - 2.0 | $m\Omega$ |
| | $R_{SEI}$ | SEI resistance | | | 0.2-0.4 [97][98] | 0.2 - 0.5 | $m\Omega$ |

The effects of the 23 parameters on the HGR profile calculated by the ROM are analyzed from the CC discharge because of the larger magnitude of the HGR and the associated higher sensitivities by discharge than those by charge. Based on the reasonable range determined from the above table, five uniformly spaced values are selected and simulated for each parameter. For the simulation profile, four C-rates of discharge are simulated to determine the relationship between C-rates and HGRs from 0.25C to 1C, where excessively high C-rates are excluded because the high overpotential completes the discharge process at a high SOC. In the simulation for the sensitivity analysis, it is assumed that the battery temperature is constant to decouple the effect of temperature on the parameters. From the change of parameters, the dispersion of the output HGR indicates the sensitivity of the parameters. Therefore, a sensitivity index (SI) [68] is introduced to express the standard deviation of the HGR at specific SOC and C-rate;

$$SI\left(SOC,C\right)=\sqrt{\frac{1}{N_s}\sum_{i=1}^{N_s}\left(\bar{\dot{Q}}-\dot{Q}_i\right)^2} \tag{56}$$

, where $N_s$ is the number of parameter states, $\dot{Q}_i$ is the HGR at the analyzed state, and $\bar{\dot{Q}}$ is the averaged HGR of the parameters. Since the HGR profiles are affected by SOC, the SI is also a function of SOC. Therefore, the averaged sensitivity index (ASI) of the parameters are calculated at five SOC regions from 0% to 100% SOC range as follows;

$$ASI\left(0\%\sim 20\%,C\right)=\frac{1}{N_{SOC20}}\sum_{j=1}^{N_{SOC20}}SI\left(SOC,C\right) \tag{57}$$

$$ASI\left(20\%\sim 40\%,C\right)=\frac{1}{N_{SOC40}}\sum_{j=1}^{N_{SOC40}}SI\left(SOC,C\right) \tag{58}$$

$$ASI\left(40\%\sim 60\%,C\right)=\frac{1}{N_{SOC60}}\sum_{j=1}^{N_{SOC60}}SI\left(SOC,C\right) \tag{59}$$

$$ASI\left(60\%\sim 80\%,C\right)=\frac{1}{N_{SOC80}}\sum_{j=1}^{N_{SOC80}}SI\left(SOC,C\right) \tag{60}$$

$$ASI\left(80\%\sim 100\%,C\right)=\frac{1}{N_{SOC100}}\sum_{j=1}^{N_{SOC100}}SI\left(SOC,C\right) \tag{61}$$

, where $N_{SOCi}$ is the number of data points in the SOC region.

Total 460 cases (23 parameters × 5 states of parameters × 4 cases of C-rates) are simulated using the ROM, and ASIs of the parameters are calculated and plotted in Figure 19, where the results are normalized for each parameter because of the various magnitudes of ASI [77]. The results have shown that the parameters have their own dependencies on SOC. On the other hand, since the HGR increases rapidly as the C-rate increases, parameters are always more sensitive at high C-rates. Therefore, the sensitivities of the parameters are further compared at the highest C-rate.

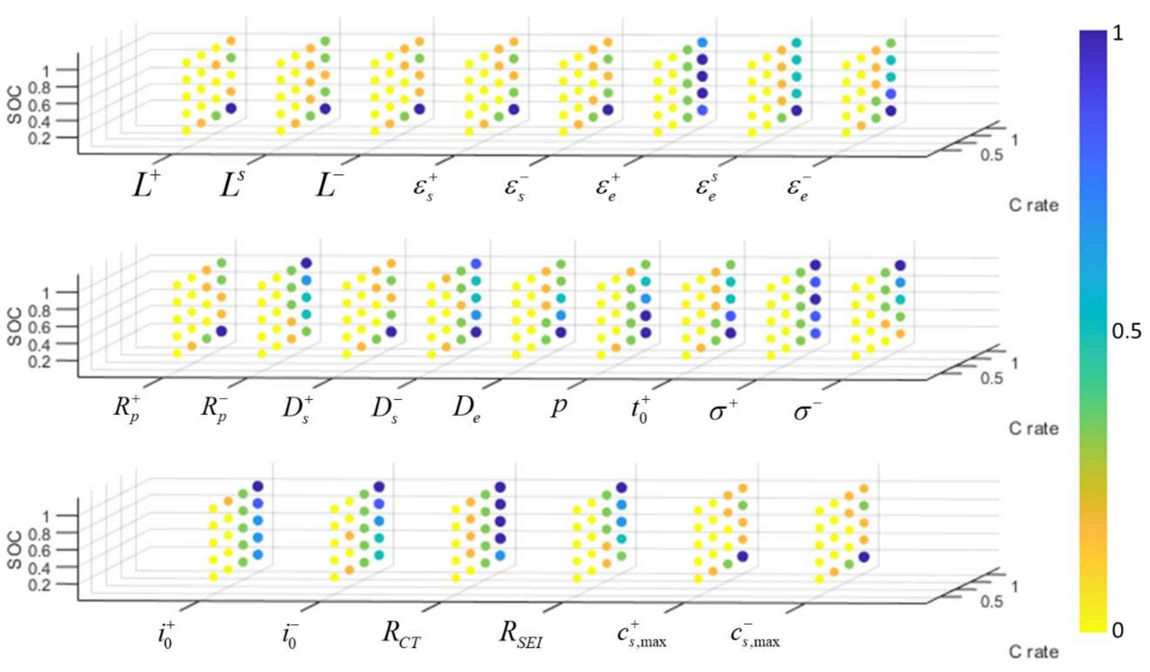

Figure 19. Normalized ASIs for 23 parameters under different C-rates and SOC ranges.

In order to compare the magnitude of each sensitivity, the highest ASIs at each of the parameters are plotted in Figure 20. The most sensitive parameters to the HGR are thickness, volume fraction, particle radius, diffusion coefficient, and contact resistance. Especially, the parameters related to the cathode electrode are more sensitive than those related to the anode electrode.

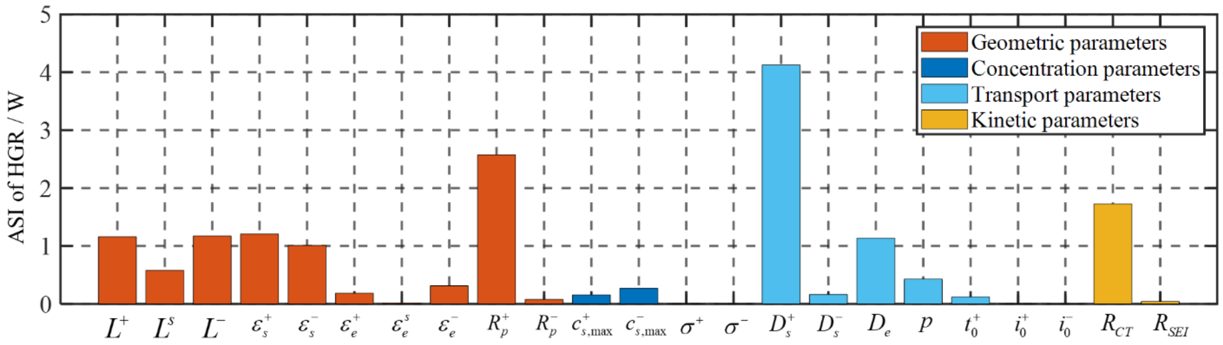

Figure 20. Highest ASIs for each parameter at 1C.

Further analysis is conducted with respect to the major heat sources generated by the contact resistance, migration of ions within the electrolyte solvents, and concentration difference within the particles, as discussed in Chapter 3. First, the ASIs of the Joule heating by the contact resistance at SOC range from 100% to 80% are plotted in Figure 21 (a). Since the Joule heating is proportional to the contact resistance and the square of the current, its profile is not affected by SOC and other parameters.

Secondly, the ASIs of the HGR by ion migration within electrolyte solvents are plotted in Figure 21 (b) as a function of SOC. In the process of the ion migration and the concentration overpotential determined by both potential and ion concentration in the electrolyte, the most closely related parameter with the two variables is the diffusion coefficient of the electrolyte solvents, and therefore the diffusion coefficient is the most sensitive to the heat. In addition, the parameters that determine the potential profile of the electrolyte, such as the volume fraction of the electrolyte solvents, the transference number, and the Bruggeman coefficient, are also sensitive because the driving force for the migration is the potential gradient. Besides, since the overpotential increases as charging or discharging proceeds [83], the heat is also affected by SOC, and therefore, the capacity-related parameters are also sensitive. There are six capacity-related parameters that are the thickness of electrodes, volume fraction, and maximum ion concentration of the active material particles, where the ASIs of the maximum ion concentration are small because of their small range compared with other parameters.

Lastly, the ASIs of the HGR by the concentration difference within the particles are plotted in Figure 21 (c). Since the heat is caused by the difference of the surface and averaged ion concentration, the parameters that determine the difference, such as the diffusion coefficient and the particle radius of active materials, are the most sensitive. Particularly, the parameters of the cathode electrode are more sensitive than those of the anode electrode. In addition, since the heat is also affected by SOC, the capacity-related parameters are also sensitive. The characteristics of the HGR are further analyzed in detail.

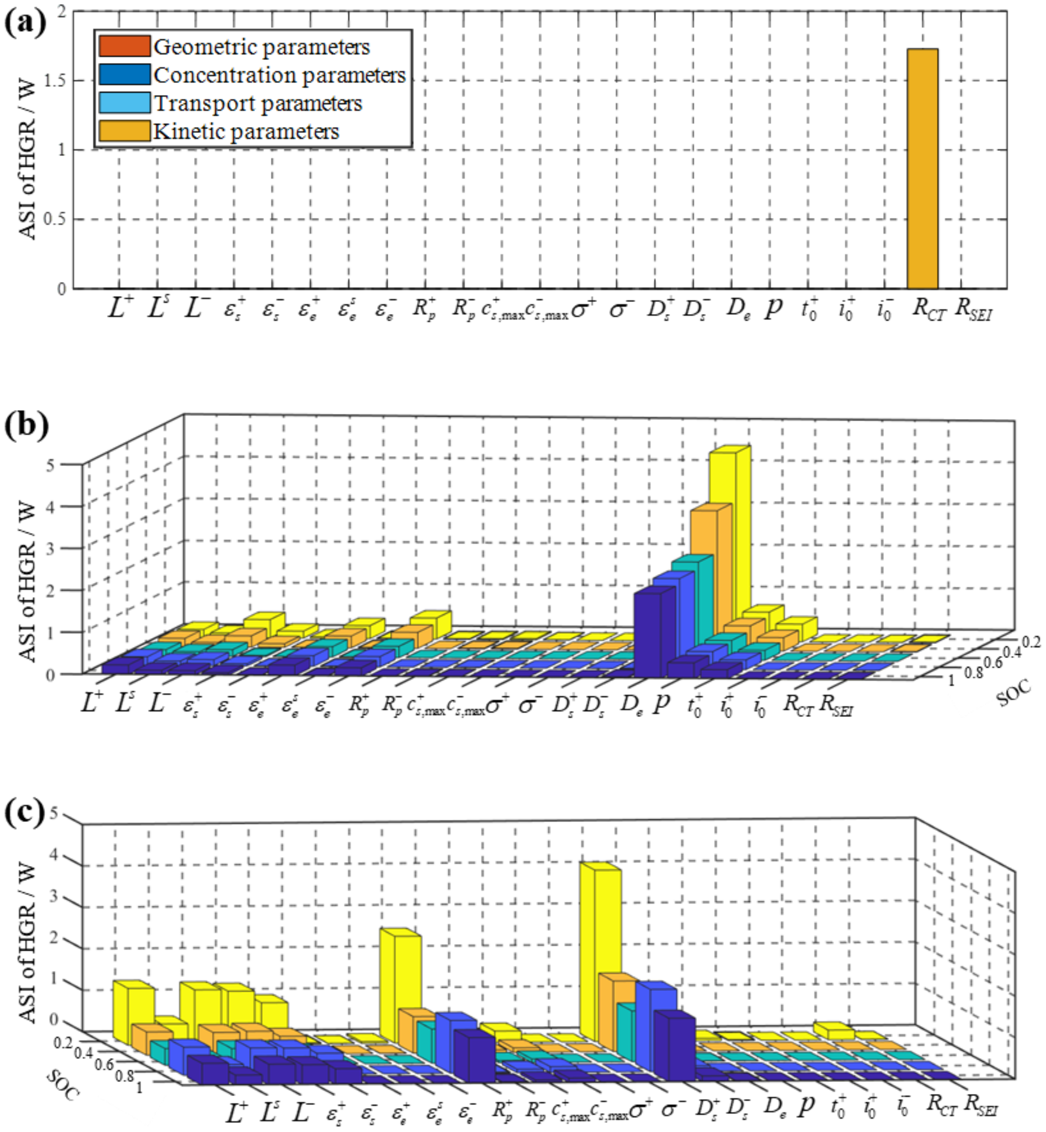

Figure 21. (a) Highest ASIs of the HGR by contact resistance; (b) ASIs of the HGR by ion migration as a function of SOC; (c) ASIs of the HGR by concentration difference within particles as a function of SOC.

In order to understand the characteristics of the parameters related to each electrode, further analysis is performed. The highest ASIs of the HGR by concentration difference within particle at each component are plotted in Figure 22 (a). The results have shown that the HGR at the cathode electrode is dominantly sensitive. In fact, as expressed in (49), the HGR is determined by the difference of the equilibrium potentials that are governed by the surface and averaged concentration. The profiles of the equilibrium potential from both electrodes are plotted in Figure 22 (b), where the equilibrium potential of the anode electrode is significantly smaller than that of the cathode electrode. Therefore, the influence of the anode parameters on the magnitude of the HGR is negligible. Besides, under the CC charge or discharge process, the difference of the ion concentration is present once the process starts but does not change significantly until the end of the process. Therefore, a similar profile of the HGR can be observed by the slope of the equilibrium potential. The slope of the equilibrium potential of the cathode electrode is plotted in Figure 22 (c). Since the potential profile of the cathode electrode has a plateau at the middle SOC and rapidly decreases at low SOC, as shown in Figure 22 (b), the corresponding sensitivity is relatively small at the middle SOC but large at the low SOC, as shown in Figure 21 (c). In addition, when the concentration difference increases at high C-rates, the profile is shifted to the higher SOC, as indicated by the red arrow.

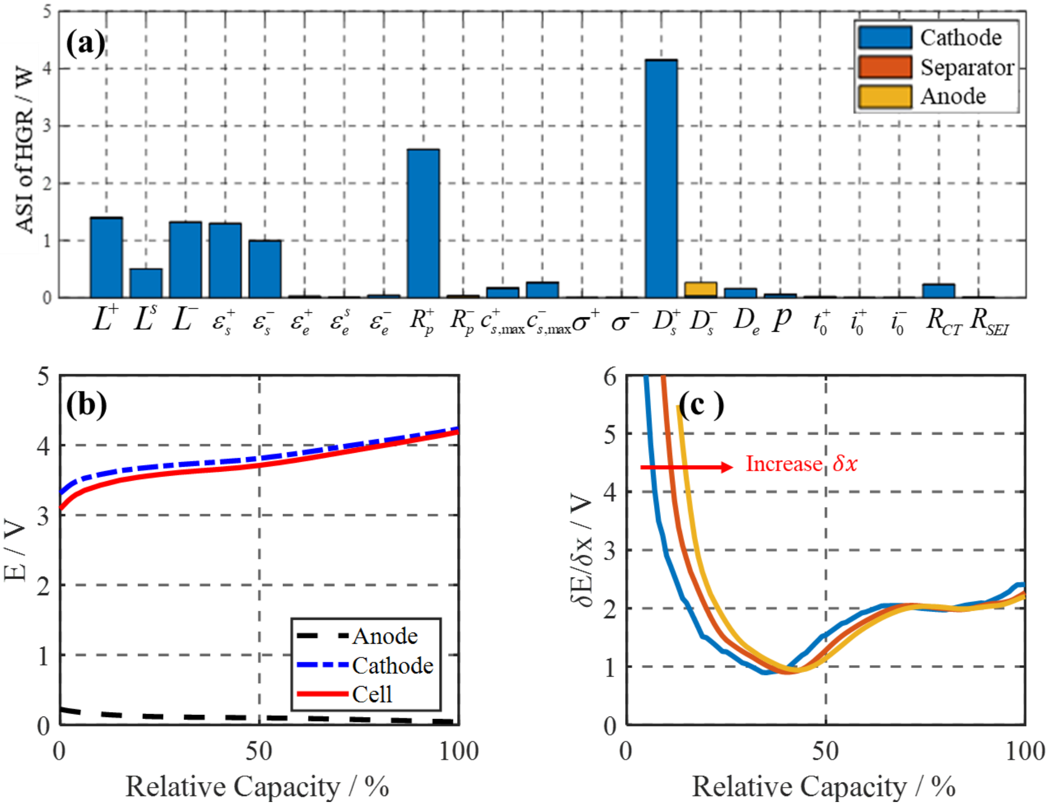

Figure 22. (a) Highest ASIs of the HGR by concentration difference within particles at each component; (b) Cell voltage and potentials of anode and cathode; (c) δE/δx of the cathode electrode, where x is $c_s/c_{s,max}$.

The analysis results have shown that the heat sources are sensitive to their individual parameters and the tendencies are also different. The HGR from the contact resistance is only sensitive to itself. The HGR by the ion migration is the most sensitive to the parameters related to the ion transport characteristics. Lastly, the HGR by the concentration difference within the particles is dominantly sensitive to diffusion coefficient and particle radius of cathode active material. The capacity-related parameters affect the overall heat sources whose profiles are a function of SOC. On the other hand, the effects of the exchange current density, the volume fraction of electrolyte at the separator, conductivity of electrodes, and the diffusion coefficient at the negative electrode on the HGR are insignificant.

### 3.5.3 Selection of parameters and procedure of identification

In the previous section, the sensitivity of the 23 parameters is analyzed, and they are classified into sensitive and insensitive parameters. Generally, in the identification process, reducing a searching space helps to find an optimal solution easier [68], which can be accomplished by reducing the number of parameters. Therefore, the insensitive parameters are not considered for identification because of their negligible effects on the HGR. Likewise, the Bruggeman coefficient and transference number have not been taken into account because of their constant value in most cases for porous structures of electrodes under the assumption of an equivalent size of particles [84]. Lastly, the thickness of the electrodes and separator are excluded so that the total heat can be calculated with a constant volume of the battery. As a result, 12 parameters are selected for the identification.

The effects of the four highest sensitive parameters, which are the contact resistance, particle radius and diffusion coefficient of the cathode active material, and diffusion coefficient of the electrolyte, are plotted as a function of SOC in Figure 23, where the red arrow indicates the trend of the HGR at increased values of the parameters. Since all parameters have their own sensitive SOC ranges, the parameters are categorized according to the degree of sensitive SOC regions based on Fuzzy C-means clustering [81] to perform the identification considering their most sensitive SOC.

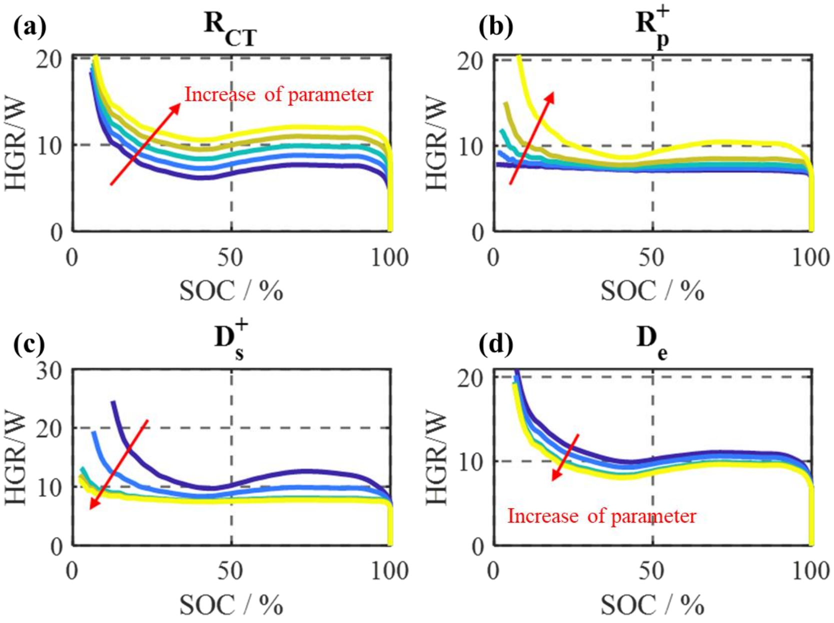

Figure 23. Comparison of the effect of parameters on the HGR; (a) Contact resistance; (b) Particle radius of active cathode material; (c) Diffusion coefficient of cathode electrode; (d) Diffusion coefficient of electrolyte.

The parameters are categorized into two groups based on their sensitivities to the SOC. The normalized ASIs of the two groups are plotted in Figure 24 (a) and (b), where the dotted lines and solid lines represent sensitivities of the parameters and clustering centers. The first group consists of only three parameters that are sensitive at high SOC, where the most sensitive parameter is the contact resistance. If the contact resistance is large, the ohmic overpotential and the Joule heating increase over the entire SOC range. However, since the discharging process is completed at higher SOC due to high overpotential, other heat sources that are large at low SOC become less. Consequently, the change of the total HGR at low SOC is smaller than that at high SOC. On the other hand, the second group includes most of the parameters that are sensitive at low SOC.

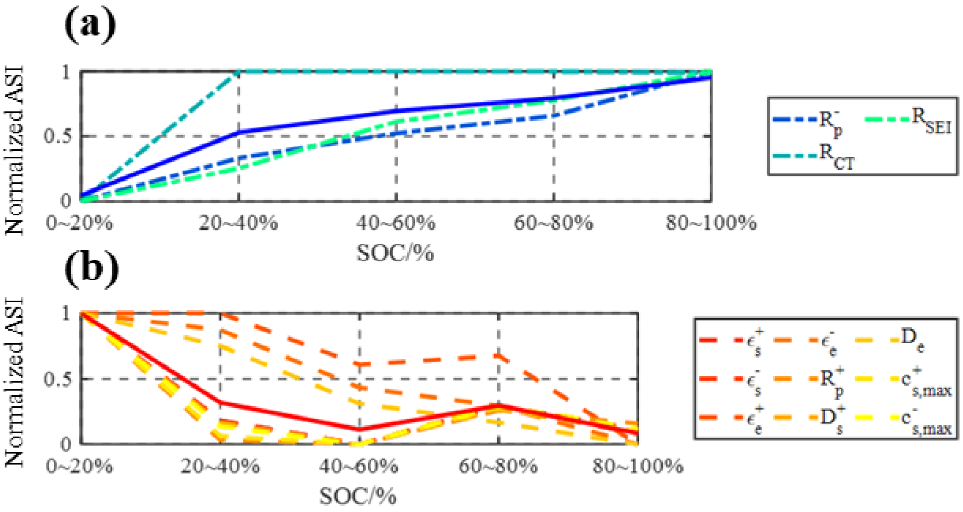

Figure 24. Results of parameter clustering; (a) Parameters sensitive at high SOC; (b) Parameters sensitive at low SOC.

Since more parameters belong to the second group, the parameters of the second group are further divided into two groups, and the new groups are plotted in Figure 25 (a) and (b), where the ASIs show a deviation with each other from 20% to 60% SOC range. The first group includes volume fraction, maximum ion concentration of electrodes, particle radius, and diffusion coefficient of the cathode active material that predominantly affect the HGR by the concentration difference within particles, as discussed in Figure 21 (c). As a result, their ASIs are small at the middle SOC but large at the low SOC. The second group includes the volume fraction and diffusion coefficient of electrolyte solvents that affect the HGR by the migration of ions, as discussed in Figure 21 (b). As a result, the ASIs become large at the middle SOC range.

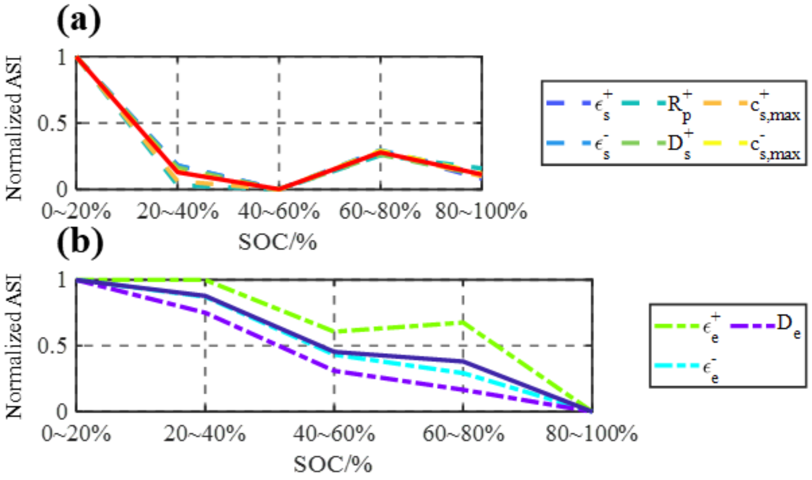

Figure 25. Results of second parameter clustering; (a) Parameters insensitive at middle SOC; (b) Parameters sensitive at middle SOC.

The clustered parameters are summarized in Table 8, where the parameters of the three groups are listed with the degree of their sensitivities using star signs. The first group consists of three parameters, and they are sensitive at high SOC but mainly determine the total heat generation because of their dominant effect on the constant Joule heating over the entire SOC range. Therefore, they need to be identified first. The second group consists of six parameters, and they are sensitive at low SOC and play an important role in forming the profile of the HGR that rapidly increases at low SOC. Lastly, the third group consists of three parameters, and they are sensitive at middle SOC, where the profile of the HGR is mainly determined by the reversible HGR, as discussed in Chapter 3. Therefore, it is more important to accurately identify parameters in the first and second groups than those in the third group. Therefore, in order to focus more on the first and second groups, two parameters with relatively low sensitivities in the second group are selected and transferred to the third group, which are the volume fraction and the maximum ion concentration of the anode electrode. As a result, only cathode parameters remain in the second group, while only anode and electrolyte parameters do in the third group.

Table 8. Modified parameter clustering results.

| Initial parameter group | | | Modified parameter group | | |
|---|---|---|---|---|---|
| Group | Parameter | Sensitivity | Group | Parameter | Sensitivity |
| First group | $R_{CT}$ | ***** | First group | $R_{CT}$ | ***** |
| | $R_{SEI}$ | * | | $R_{SEI}$ | * |
| | $R_p^-$ | * | | $R_p^-$ | * |
| Second group | $D_s^+$ | ***** | Second group | $D_s^+$ | ***** |
| | $R_p^+$ | *** | | $R_p^+$ | *** |
| | $\epsilon_s^+$ | ** | | $\epsilon_s^+$ | ** |
| | $\epsilon_s^-$ | ** | | $c_{s,max}^+$ | * |
| | $c_{s,max}^+$ | * | Third group | $D_e$ | ***** |
| | $c_{s,max}^-$ | * | | $\epsilon_s^-$ | ** |
| Third group | $D_e$ | ***** | | $\epsilon_e^+$ | * |
| | $\epsilon_e^-$ | * | | $\epsilon_e^-$ | * |
| | $\epsilon_e^+$ | * | | $c_{s,max}^-$ | * |

The clustered parameters are identified separately by a three-stage stepwise parameter identification procedure [68], as depicted in Figure 26 (a). At each stage, the parameters in each group are identified, where there exist some parameters that have not been identified initially. The unidentified parameters are temporarily set by the values available in the literature and replaced later by the identified values. For the optimization method, a genetic algorithm (GA) is applied [85], and the objective function is to minimize the error between the experimental data and the simulation results calculated by the ROM, where the battery temperature is used for comparison. The temperature profiles and the corresponding terminal voltages at each stage are plotted in Figure 26 (b). For the experiment, the battery is discharged for 20% SOC at 1C, where the initial SOCs for each group are different according to their sensitive SOC ranges. In this study, since the parameters have significantly different tendencies as a function of SOC, it does not require the experiment data under various temperatures and the current rates for the optimization. For the experiment, the battery is placed in a thermal chamber, and the temperature change is measured using four K-type thermocouples. One of the thermocouples measures the ambient temperature, while the others measure the surface temperature of the cell at the center and near the two tabs. Then, the three cell temperatures are averaged for further validation. In this study, the effect of the temperature gradient inside the cell is not considered. The cell used for the experiment is a large-format pouch-type NMC / Graphite cell with a capacity of 60Ah. For the model validation, since the cell temperature changes during operations, some parameters are affected by the change of temperatures, such as the diffusion coefficients or SEI resistance. Accordingly, the parameters are updated during simulation, according to Arrhenius law.

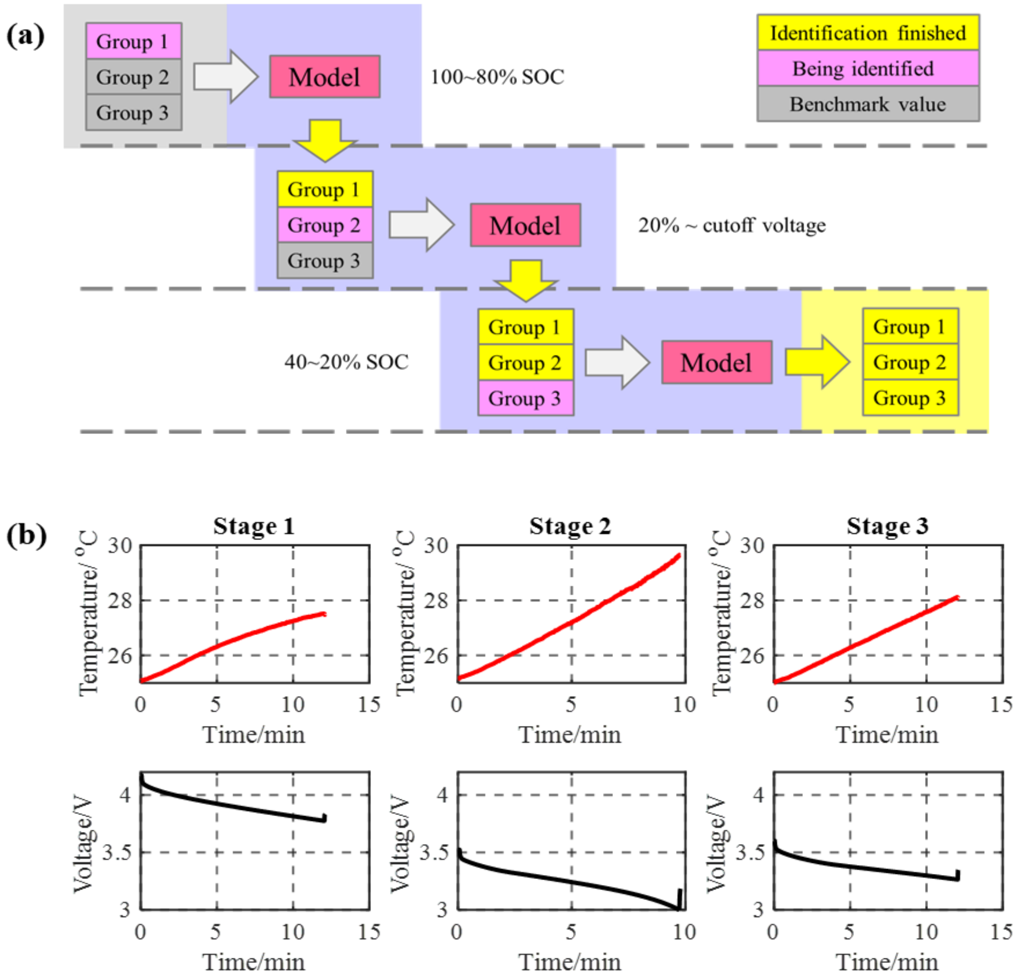

Figure 26. (a) Flowchart of parameter identification procedure; (b) Experiment data for parameter identification.

### 3.5.4 Results of parameter identification and discussion

The identification is conducted four times to ensure accuracy, and the results of the identification are summarized in Table 9. In addition, in order to visualize the results, the values of the parameters are normalized and plotted in Figure 27, where red squares indicate the averaged parameters and blue lines do the dispersion of them. The results have shown that the parameters are converged within the optimal ranges. However, some parameters with large dispersion exist, such as particle radius and the maximum ion concentration of the electrodes that are capacity-related parameters. In fact, there are several different cases of parameter sets that result in the same capacity. Therefore, the ranges of the optimal solutions of those parameters are relatively larger.

Table 9. Parameter identification results for NMC / Graphite cell.

| Parameter | Boundaries | Unit | 1st test | 2nd test | 3rd test | 4th test | Averaged |
|---|---|---|---|---|---|---|---|
| $\epsilon_s^+$ | 0.4 – 0.65 | - | 0.594 | 0.58 | 0.579 | 0.577 | 0.583 |
| $\epsilon_s^-$ | 0.4 – 0.6 | - | 0.4 | 0.406 | 0.4 | 0.401 | 0.402 |
| $\epsilon_e^+$ | 0.23 – 0.4 | - | 0.389 | 0.386 | 0.398 | 0.398 | 0.393 |
| $\epsilon_e^-$ | 0.23 – 0.4 | - | 0.399 | 0.4 | 0.4 | 0.4 | 0.4 |
| $R_p^+$ | 1 – 11 | $um$ | 8.626 | 10.993 | 9.07 | 8.121 | 9.203 |
| $R_p^-$ | 1 – 11 | $um$ | 6.637 | 5.132 | 5.002 | 5.007 | 5.444 |
| $D_s^+$ | 1 – 10 | $10^{-10} m^2 s^{-1}$ | 1.731 | 3.059 | 1.967 | 1.61 | 2.092 |
| $D_e$ | 1.5 – 5 | $10^{-6} m^2 s^{-1}$ | 4.933 | 4.94 | 4.997 | 4.894 | 4.941 |
| $R_{CT}$ | 0.7 – 2.0 | $m\Omega$ | 1.426 | 1.435 | 1.436 | 1.434 | 1.433 |
| $R_{SEI}$ | 0.2 – 0.5 | $m\Omega$ | 0.203 | 0.201 | 0.204 | 0.208 | 0.204 |
| $c_{s,max}^+$ | 4.8 – 5.2 | $10^4 mol\, m^{-3}$ | 5.074 | 5.069 | 5.189 | 5.152 | 5.121 |
| $c_{s,max}^-$ | 2.9 – 3.3 | $10^4 mol\, m^{-3}$ | 2.902 | 2.918 | 2.9 | 3.016 | 2.934 |

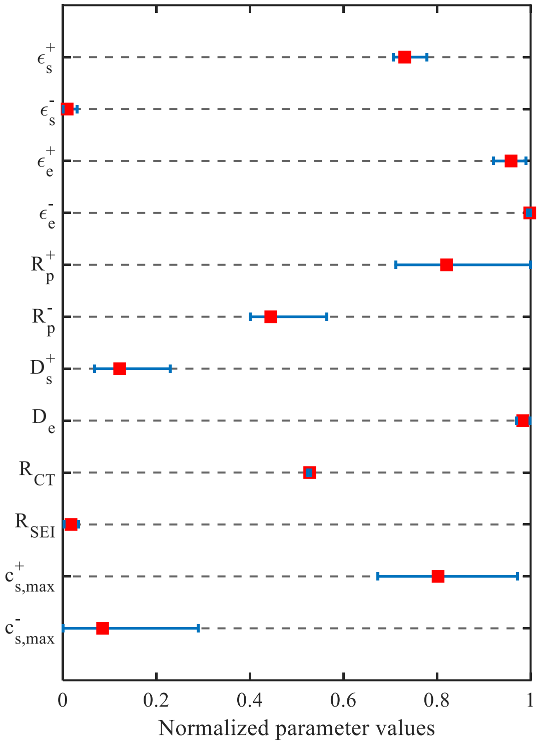

Figure 27. Normalized parameters obtained from identification – Averaged parameters and error bars.

The identified parameters incorporated into the ROM are further validated by comparing the measured cell temperature under the constant current / constant voltage (CC/CV) charge and CC discharge at various C-rates over the entire SOC range, where the convection coefficient is assumed to be 37W $m^{-2}K^{-1}$. The temperature profiles measured by experiment and calculated by the ROM using the identified parameters under 0.3C, 0.5C, and 1C CC/CV charge and CC discharge are plotted in Figure 28 (a) and (b), where a short resting period is included after discharge in order to ensure accurate results and the simulation results using the second parameter set are plotted. The results have shown that the model with the identified parameters is capable of decently predicting the overall temperature profiles. However, there are some discrepancies in the temperature profiles at the middle of charge and discharge. Since the simulation results are larger during charge but smaller during discharge than the measurement, the discrepancies could be arisen by the reversible HGR. The entropy coefficient is not considered in the identification, and therefore any errors from the coefficient can result in discrepancies. In order to evaluate the simulation results from other parameter sets, the RMS errors of the model using four sets of parameters are calculated and compared in Table 10. All of the results are able to accurately estimate the temperature profiles with the maximum RMS error of 0.22°C. In addition, in order to evaluate the performance of the model under the different current profiles, the second validation is carried out using current profiles obtained from driving cycles of an electric vehicle, where the same parameter set is used. The current profiles of the driving cycles and corresponding temperature profiles from the experiment and simulation are plotted in Figure 28 (c). The results have shown that the model has a weakness in the estimation of the abruptly changing temperatures, but the overall temperature errors still remain within the error boundary of 0.1°C.

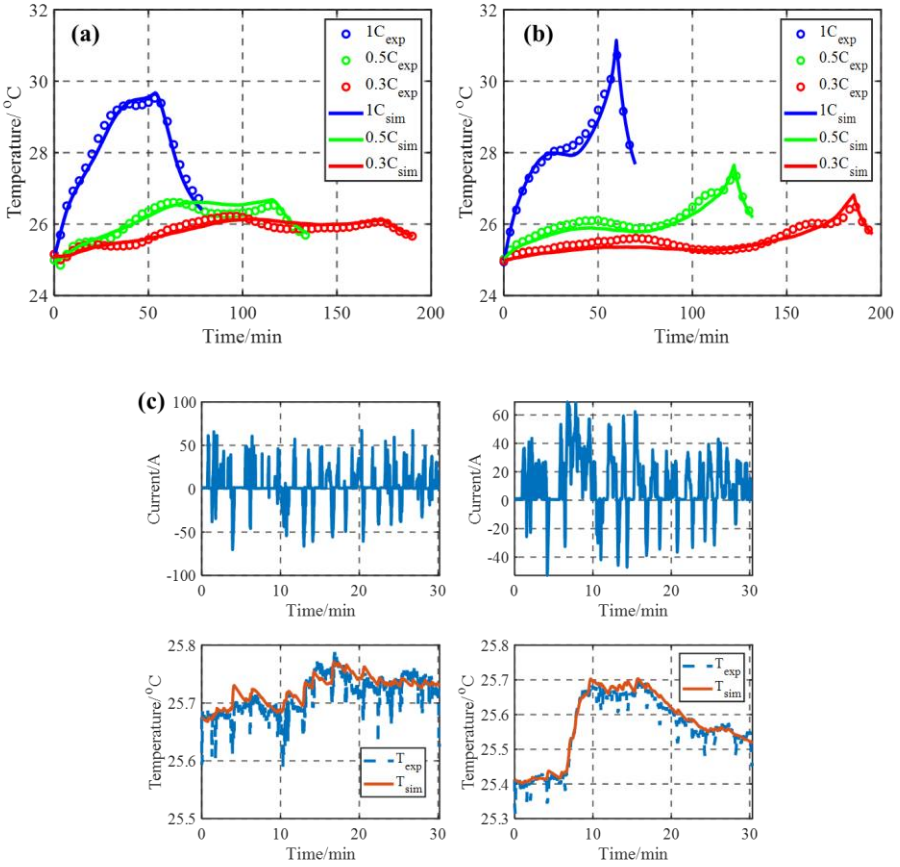

Figure 28. Comparison of simulation results with experiment; (a) Temperature profiles under 0.3C, 0.5C, and 1C CC/CV charge; (b) Temperature profiles under 0.3C, 0.5C, and 1C CC discharge and resting; (c) Current profile of driving cycles (upper) and corresponding temperature profile (lower).

Table 10. RMS error between simulation and experimental measurement.

| | **Charge** | | | **Discharge** | | |
|---|---|---|---|---|---|---|
| Current rate | **0.3C** | **0.5C** | **1C** | **0.3C** | **0.5C** | **1C** |
| 1st test | 0.12°C | 0.16°C | 0.19°C | 0.13°C | 0.17°C | 0.22°C |
| 2nd test | 0.11°C | 0.16°C | 0.18°C | 0.14°C | 0.14°C | 0.17°C |
| 3rd test | 0.11°C | 0.16°C | 0.19°C | 0.13°C | 0.18°C | 0.22°C |
| 4th test | 0.11°C | 0.16°C | 0.18°C | 0.13°C | 0.15°C | 0.18°C |

## 3.6 Summary

In this chapter, A thermal model is developed from the physics-based reduced-order electrochemical model to estimate the HGR of the battery, and the results are validated against experimental data. Then a detailed analysis of the HGR is conducted using the validated thermal model. The analysis has shown that the dominant heat sources of the battery are caused by the contact resistance, migration of the ions within the electrolyte phase, change of entropy, and the difference in the ion concentration within active material particles. Those sources vary with different operating conditions. Therefore, the effects of the C-rates and temperatures on the overall HGR are investigated. The entropic HGR is proportional to the C-rate, and its sign depends upon the charging or discharging process. Additionally, the irreversible HGR has a quadratic dependency with the C-rate. Consequently, the entropic heat is dominant at low C-rates, while the irreversible heat becomes dominant as the C-rate increases. In addition, at the same C-rate, the magnitude of total heat during discharging is always greater than that during charging due to the entropic heat and higher charge transfer resistance. It has also been shown that lowering temperature increases the irreversible HGR rapidly because of increased overpotentials. However, the entropic HGR is not affected significantly by the temperature. This paper demonstrates that a physics-based electrochemical-thermal model can be used to analyze the effects of operating conditions of various C-rates and temperatures on the HGR, which could be used to optimize thermal management systems with respect to cost and efficiency. In addition, the sensitivity of parameters to the battery heat generation rate is studied. Total 23 physical parameters that affect the thermal behaviors of lithium-ion batteries are selected, and their ranges are extracted from the literature. The calculated sensitivities have revealed various tendencies, where the four most sensitive parameters are the diffusion coefficient of active material and electrolyte, particle radius, and contact resistance. Especially, it is shown that the parameters related to the cathode materials are more sensitive than those related to the anode materials because of the equilibrium potential. After the analysis, the parameters are categorized with respect to dominant ranges of state of charge from the clustering method. Finally, a new parameter identification procedure is designed based on a three-stage stepwise identification procedure from the clustering results. The measured temperature profiles using a pouch-type large-format lithium-manganese-cobalt-oxide/ Graphite cell are used for the identification and experimental validation. The identification employs the genetic algorithm for optimization that minimizes the model error of the temperature. The results of the identification have shown that the parameters are converged within an optimal solution. The experimental validation of the model with the identified parameters is conducted against the measured temperature profiles at constant charge and discharge profiles obtained over the full range of the state of charge and the driving cycles. The results have shown an excellent agreement between simulation and experiment.

# Chapter 4. Design of fast and safe charging method at subzero temperature considering degradation and start-up strategy

In chapter 2, the charging algorithm considering the chemical degradation at room temperature is proposed. The limitations of the algorithm are that the battery heat generation is not considered, and it cannot be applied at subzero temperatures because of different mechanisms of degradation at low temperatures. Due to increased charge transfer and reduced ionic diffusivity at low temperatures, battery overpotentials become larger, and the lithium plating takes place much easier. In addition, due to sluggish parameters related to the charge transport such as SEI resistance, contact resistance, or diffusion coefficient, a steep ion concentration gradient inside the active material particle is developed, and much larger strain energy is developed, which leads to mechanical degradation. Therefore, it is important to warm up the battery at the beginning of charging, which is called a battery start-up strategy. In this chapter, an extended charging algorithm that can be applied at subzero temperatures is designed considering the start-up strategy based on the proposed model considering both chemical and mechanical degradation.

## 4.1 Modeling of mechanical degradation.

A literature review of mechanical degradation is summarized in Chapter 2.1. A schematic diagram of degradation of the active material particles on the anode and cathode electrodes is depicted in Figure 29, where arrows indicate the path of participating charges and EC. There are three different types of depositions on the surface of anode material particles as products of the chemical degradations that are the SEI layer, the plated lithium metal, and the secondary SEI layer.

On the other hand, no deposition is formed at the cathode active material particles, but cracks and fractures are generated because of the accumulation of the strain energy under DIS.

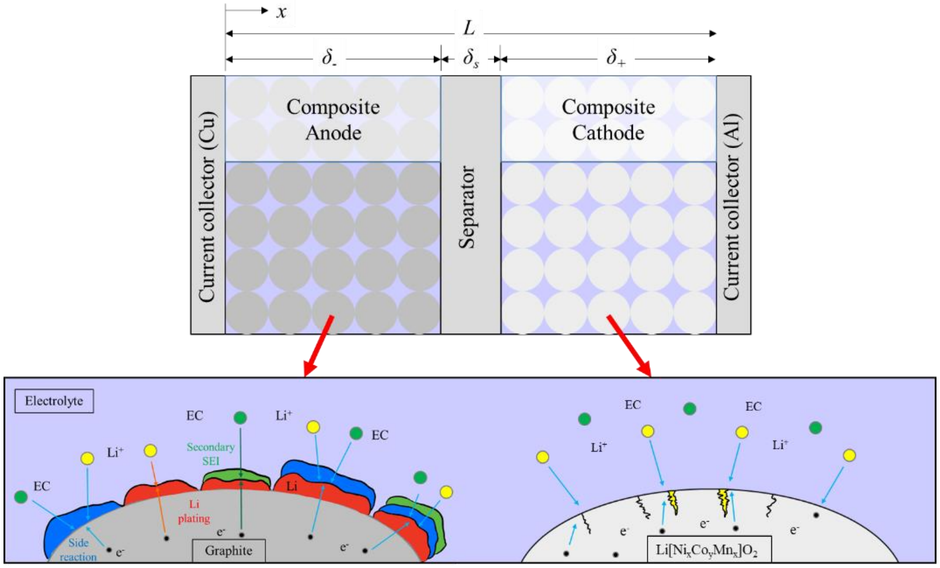

Figure 29. Schematic diagram of degradation on anode and cathode electrodes.

In order to model the mechanical degradation by the DIS, the electrode particles are approximated as isotropic linear elastic spheres with an identical radius. Stress-stain relationships in the spherical coordinate system can be transformed to one-dimensional polar forms as follows [102];

$$\varepsilon_r = \frac{1}{E}\left[\sigma_r - \nu(\sigma_t + \sigma_t)\right] + \frac{1}{3}c_s\Omega \qquad (62)$$

$$\varepsilon_t = \frac{1}{E}\left[\sigma_t - \nu(\sigma_t + \sigma_r)\right] + \frac{1}{3}c_s\Omega \qquad (63)$$

, where Ω is the Partial Molar Volume (PMV) of the lithium ions in the electrode that is defined as the volume change of the electrode when the lithium ions are intercalated. The PMV of each electrode is different because of the different structures of electrodes. $\sigma_r$, $\sigma_t$, $\varepsilon_r$, and $\varepsilon_t$ are stress and strain components in the radial and tangential direction.

The stress equilibrium for a differential volume is

$$\frac{d\sigma_r}{dr} + \frac{2}{r}(\sigma_r - \sigma_t) = 0 \tag{64}$$

The strain-displacement relations are

$$\varepsilon_r = \frac{du}{dr} \tag{65}$$

$$\varepsilon_t = \frac{u}{r} \tag{66}$$

, where $u$ denotes the displacement in a radial direction.

In order to solve the stress equilibrium equation, two boundary conditions are used, considering symmetric spheres and a free surface of the particles under the assumption that the reaction forces between particles are small and negligible. Accordingly, the radial displacement $u$ at the center of the sphere is zero because of the symmetricity, and the radial stress $\sigma_r$ at the particle surface is zero because of the free surface. Based on (62)-(66) and the boundary conditions, the stress and radial displacement can be solved as a function of $r$ and $c_s(r)$;

$$\sigma_r = \frac{2\Omega E}{3(1-\nu)}\left( \frac{1}{R_{s0}^3}\int_0^{r_{s0}} c_s r^2 dr - \frac{1}{r^3}\int_0^{r} c_s r^2 dr \right) \tag{67}$$

$$\sigma_t = \frac{\Omega E}{3(1-\nu)}\left( \frac{2}{R_{s0}^3}\int_0^{r_{s0}} c_s r^2 dr + \frac{1}{r^3}\int_0^{r} c_s r^2 dr - c_s \right) \tag{68}$$

$$u = \left[ \frac{2\Omega(1-2\nu)}{9(1-\nu)} \cdot \frac{3}{r_{s0}^3}\int_0^{r_{s0}} c_s r^2 dr + \frac{\Omega(1+\nu)}{9(1-\nu)} \cdot \frac{3}{r^3}\int_0^{r} c_s r^2 dr \right] \cdot r \tag{69}$$

The equations above require lithium-ion concentration as a function of the location of particles in the electrodes, the particle radius, and time, which requires solving Fick's second law. Due to the complexity of the solver, the cathode degradation has only been considered in the FOM. Therefore, a new formula is necessary to apply the cathode degradation in the ROM.

In order to reduce the complexity of solvers for Fick's second law, several reduction techniques have been proposed, such as polynomial approximation or Pade approximation. From the techniques, the ion concentration as a function of radius is replaced with new variables that are averaged ion concentration, the concentration at the surface of the particle, and averaged ion flux. Therefore, the equations for DIS can also be reduced by replacing the ion concentration with those variables. In this study, only the averaged and surface ion concentrations are used, considering the simplicity and the universality of various reduction methods. The averaged and surface ion concentrations are defined as follows;

$$c_{s,ave}\left(x,t\right)=\int_{r=0}^{R}\frac{3r^2}{R^3}c_s\left(x,r,t\right)dr \tag{70}$$

$$c_{s,surf}\left(x,t\right)=c_s\left(x,R,t\right) \tag{71}$$

Under the assumptions that the ion concentration can be expressed by quadratic formula as a function of radius, the equations (67) and (68) can be simplified by substituting simplified ion concentration into the equations as follows;

$$\sigma_r\left(r\right)=\frac{E\Omega\left(R^2-r^2\right)\left(c_{s,surf}-c_{s,ave}\right)}{3R^2\left(1-\nu\right)} \tag{72}$$

$$\sigma_\theta\left(r\right)=\frac{E\Omega\left(R^2-2r^2\right)\left(c_{s,surf}-c_{s,ave}\right)}{3R^2\left(1-\nu\right)} \tag{73}$$

Then, the mean stress can be expressed as follows;

$$\sigma_{mean}\left(r\right)=\frac{\sigma_r\left(r\right)+\sigma_\theta\left(r\right)}{3}=\frac{E\Omega\left(2R^2-3r^2\right)\left(c_{s,surf}-c_{s,ave}\right)}{9R^2\left(1-\nu\right)} \tag{74}$$

In addition, the redial displacement from insertion can be expressed as follows;

$$u\left(r\right)=\frac{r\Omega\left[R^2\left(3-\nu\right)c_{s,ave}-r^2\left(1+\nu\right)c_{s,ave}-\left(R^2-r^2\right)\left(1+\nu\right)c_{s,surf}\right]}{6R^2\left(1-\nu\right)} \tag{75}$$

Since the strain energy density is accumulated as a result of the elastic deformation, the strain energy density for the isotropically deformed sphere is expressed as [25];

$$e\left(r\right)=-\frac{E\Omega^2\left(c_{s,surf}-c_{s,ave}\right)^2\left[10r^2R^2\left(1-2\nu\right)+3R^4\left(-1+2\nu\right)+r^4\left(-9+16\nu\right)\right]}{18R^4\left(1-\nu\right)^2} \tag{76}$$

Then, the total strain energy stored in the sphere provides the driving force for fracture, which can be obtained by integrating the strain energy density over the entire volume of the spheres.

$$E_T=-\frac{4E\pi R^3\Omega^2\left(c_{s,surf}-c_{s,ave}\right)^2}{63\left(1-\nu\right)} \tag{77}$$

It has been reported that the cracks and fractures take place only in the circumstance when the amount of strain energy becomes larger than a critical limit [103]. Therefore, the loss of the active material can be obtained by calculating a ratio between the current exceeded strain energy and standard strain energy obtained by the average strain energy under the standard cycle [104].

$$\gamma\left(t\right)=\max\left(0,\frac{E_T\left(t\right)-E_{\lim}}{E_{stn}-E_{\lim}}\right) \tag{78}$$

, where $E_{lim}$ is critical strain energy, and it is assumed that the loss of the active material follows a linear relationship with the excessed strain energy. By integrating the above strain energy ratio, the loss of the active material can be represented as the change of the volume fraction of cathode active material;

$$\Delta\varepsilon_{s,mech}\left(\tau\right) = -k_{al}\varepsilon_{s}\int_{t=0}^{\tau}\gamma\left(t\right)dt \tag{79}$$

Therefore, the capacity loss caused by loss of active material can be expressed by the change of the volume fraction of the active material as follows;

$$q_{\mathrm{loss}}^{mech}\left(\tau\right) = \frac{c_{s,\max,pos}^{initial}\left(Stoi_{0,pos}^{initial} - Stoi_{100,pos}^{initial}\right)\delta_{pos}A\Delta\varepsilon_{s,mech}\left(\tau\right)F}{3600} \tag{80}$$

,where $c_{s,\max,pos}^{initial}$ is initial maximum ion concentration, $Stoi_{0,pos}^{initial}$ and $Stoi_{100,pos}^{initial}$ are initial stoichiometry number of the electrode at 0% and 100% of SOC, and $\delta_{pos}$ is the thickness of the cathode electrode.

## 4.2 Model validation at subzero temperatures

In order to experimentally validate the proposed model, additional cycling tests are conducted, where the battery is placed in a thermal chamber, and the ambient temperature is set as -10°C, where both chemical and mechanical degradations can be accelerated. The battery used for the experiment is a commercial large-format pouch-type NMC/graphite lithium-ion battery with a nominal capacity of 101.8Ah. The parameters used for the model are summarized in Table 11. Then, the measured data after cycling tests was used to estimate the parameters related to the degradation. For the parameter estimation, the automatic tuning method described in Chapter 4 was used based on GA. Among the parameters, some parameters that can be affected by operating temperature, such as diffusion coefficient, contact resistance, or SEI resistance, are fitted using the Arrhenius-type correlation;

$$\psi = \psi_{ref} \exp\left\{ \frac{E_{act}}{R} \left( \frac{1}{T_{ref}} - \frac{1}{T} \right) \right\} \tag{81}$$

, where $\psi$ represents a temperature-related parameter, $\psi_{ref}$ does the reference value of the parameter at 25°C. $E_{act}$ is the activation energy, $R$ is the universal gas constant, $T$ is the temperature of the battery, and $T_{ref}$ is the reference temperature that is 25°C.

Table 11. Cell information and model design parameters.

| Category | Parameter | Negative electrode | Separator | Positive electrode |
|---|---|---|---|---|
| Design specifications (geometry and volume fractions) | Thickness, $\delta$ (cm) | $129*10^{-4}$ | $12*10^{-4}$ | $85.9*10^{-4}$ |
| Lithium-ion concentration | Maximum solid phase concentration, $c_{s,\,max}$ (mol cm$^{-3}$) | $35.3*10^{-3}$ |  | $42.0*10^{-3}$ |
|  | Stoichiometry at 0% SOC: Stoi0 | 0.3236 |  | 0.8764 |
|  | Stoichiometry at 100% SOC: Stoi100 | 0.8729 |  | 0.3217 |
|  | Charge-transfer coefficient, $\alpha_a$, $\alpha_c$ | 0.5, 0.5 |  | 0.5, 0.5 |
|  | Solid phase conductivity, $\sigma$ (S cm$^{-1}$) | 1 |  | 0.01 |
|  | Electrolyte phase Li+ diffusion coefficient, $D_e$ (cm$^2$ s$^{-1}$) | $2.3*10^{-6}$ |  | $2.3*10^{-6}$ |
|  | Solid phase Li+ diffusion coefficient, $D_{s,0}$ (cm$^2$ s$^{-1}$) | $187.0*10^{-6}$ |  | $187.0*10^{-6}$ |
|  | Bruggeman's porosity exponent, p | 1.5 | 1.5 | 1.5 |
|  | Electrolyte phase ionic conductivity, $\kappa$ (S cm$^{-1}$) | $15.8c_e \exp(850c_e^{1.4})$ |  | $15.8c_e \exp(850c_e^{1.4})$ |
|  | Li+ transference number, t+0 | 0.363 | 0.363 | 0.363 |
| Equilibrium potential | Negative electrode (V) | $U\_(x) = 8.00229 + 5.647x - 12.578x^{1/2} - 8.6322*10^{-4}x^{-1} + 2.1765*10^{-5}x^{3/2} - 0.46016*\exp(15*(0.06-x)) - 0.55364*\exp(-2.4326*(x-0.92))$ , where $x = \bar{c}_{s,surf} / \bar{c}_{s,\max}$ |  |  |
|  | Positive electrode (V) | The difference between OCV and the equilibrium potential of the negative electrode |  |  |
| Side reaction | Equilibrium potential of side reaction, $U_{eq,\,side}$ (V) | 0.4 |  |  |
|  | Kinetic rate constant for side reaction, $k_{side}$ (A cm mol$^{-1}$) | $6.5*10^{-9}$ |  |  |
|  | Cathodic symmetric factor of side reaction, $\alpha_{c,side}$ | 0.7 |  |  |

| | | |
|---|---|---|
| Lithium plating, stripping | Equilibrium potential of lithium plating, $U_{eq,\,Li}$ (V) | 0 |
| | Exchange current density for lithium plating, $i_{0,Li}$ (A cm mol$^{-1}$) | $2.8*10^{-3}$ |
| | Cathodic factor of lithium plating, $\alpha_{c,Li}$ | 0.7 |
| | Anodic factor of lithium plating, $\alpha_{c,Li}$ | 0.3 |

For the model validation, the terminal voltage responses of the battery at charging and discharging under various C-rates are estimated by the model, and the results are plotted in Figure 30. In addition, RMS errors from each case are calculated and listed in Table 12. The voltage profiles estimated by the model show good agreement with the profile measured by the experiment.

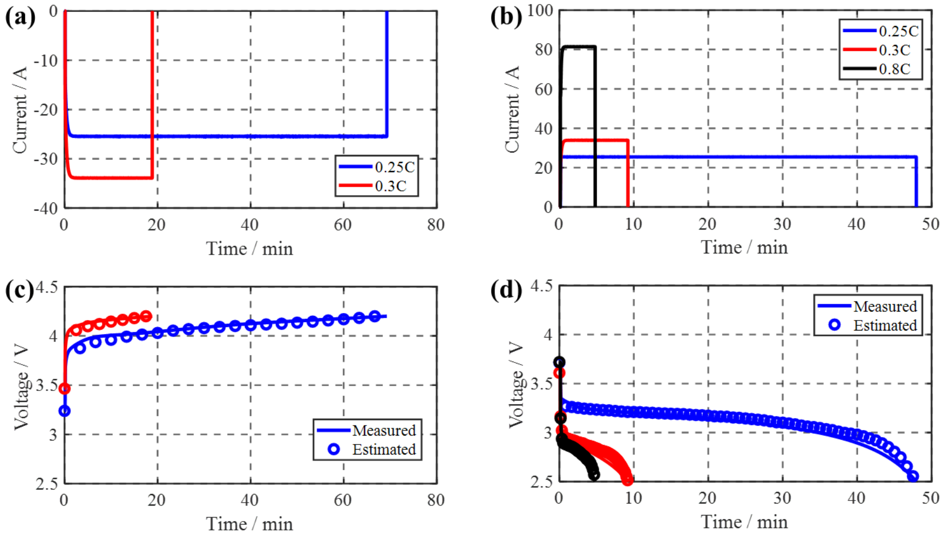

Figure 30. Current and voltage profiles at -10°C by experiment and simulation; (a) Current profiles during charging; (b) Current profiles during discharging; (c) Voltage profiles during discharging; and (d) Voltage profiles during discharging.

Table 12. RMS errors of terminal voltage at BoL.

| | Charge | | Discharge | | |
|---|---|---|---|---|---|
| | 0.25C | 0.3C | 0.25C | 0.3C | 0.8C |
| Error (mV) | 28 | 29 | 48 | 66 | 43 |

In order to observe the effect of the degradations under different charging and discharging conditions, three cycling tests were conducted. The batteries were cycled up to the cutoff voltage specified by the manufacturer with three different cases that are (0.25C CC charge / 0.25C CC discharge), (0.25C CC charge / 0.8C CC discharge), and (0.3C CC charge / 0.25CC discharge), respectively. The charging current of case 1 and case 2 is set as the same, and the discharging current of case 1 and case 3 is set for an accurate comparison. For case 2, considering the high overpotential during 0.8C CC discharge, after discharge, the battery was discharged again with 0.25C CC considering the accurate comparison. Similarly, for case 3, the battery was charged again with 0.25C CC. By considering temperature rise during cycling, the batteries were rested for 30 minutes between each charging or discharging to ensure that the battery temperature is always kept at -10°C. The batteries were initially cycled at room temperature to stabilize them. At every 20 cycles, the cycling was stopped, and the cell temperature was increased to room temperature to the change of voltage characteristics at the same condition.

The validation results of case 1 (0.25C CC charge / 0.25C CC discharge) are plotted in Figure 31. The voltage profiles under charging and discharging at -10°C measured by experiment and those estimated by the model are compared in Figure 31 (a) and (b), and the voltage profiles at 25°C are compared in Figure 31 (c), where solid lines and markers represent the results estimated by the model and those measured by the experiment, respectively. In addition, the capacity fade by the degradation sources calculated by the model is plotted with measured capacity fade in Figure 31 (d).

The results have shown that the model is able to estimate the change of voltage characteristics accurately until 18% of capacity fade. In addition, due to the sluggish kinetics of the battery, the effect of the degradations on the voltage characteristics is much larger at low temperatures, which causes the battery to reach the cutoff voltage earlier as the cycle proceeds. On the other hand, due to the reduced cycling time, the rate of degradation becomes reduced, as shown in Figure 31 (d). In this case, due to the low C-rate for the charging, the lithium plating did not take place, and the degradation is caused only by side reaction and mechanical stress, where the magnitude of the side reaction is dominant.

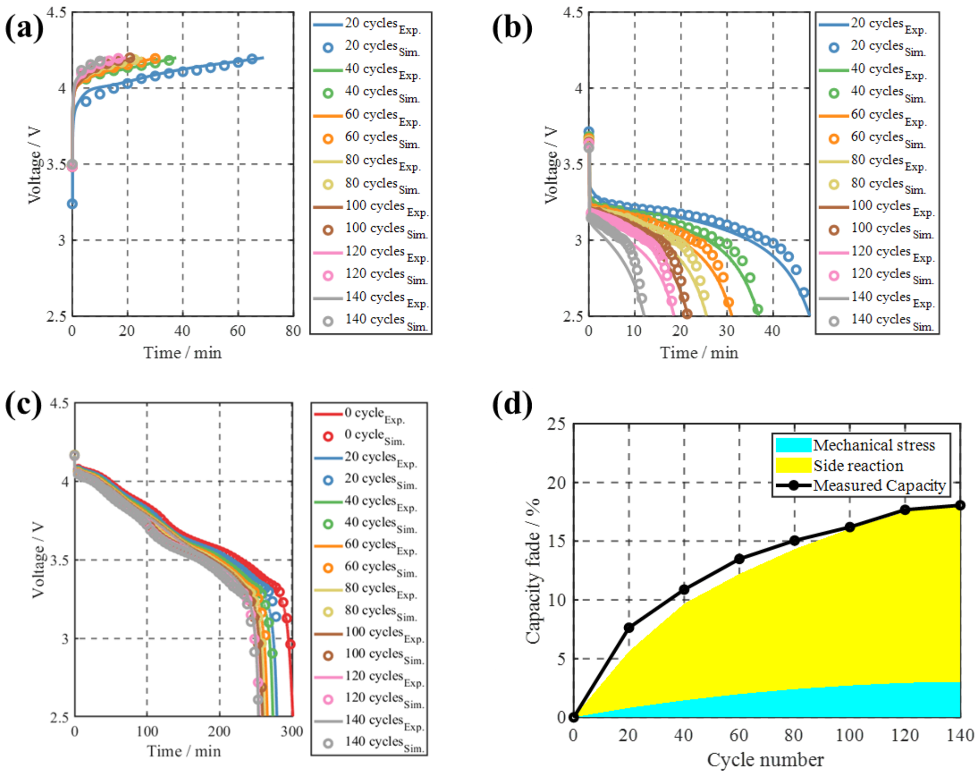

Figure 31. (a) Voltage characteristics under 0.25C CC charge at -10°C; (b) Voltage characteristics under 0.25C CC discharge at -10°C; (d) Voltage characteristics under 0.25C CC discharge at 25°C; and (d) Capacity fade by the model and experiment.

The results of case 2 (0.25C CC charge / 0.8C CC discharge) are plotted in Figure 32. The voltage profiles at -10°C are compared in Figure 32 (a) and (b), and the voltage profiles at 25°C are compared in Figure 32 (c). In addition, the capacity fade by the degradation sources calculated by the model is plotted with measured capacity fade in Figure 32 (d).

The results have shown that the lithium plating does not take place because of the same charging condition as the first case. In addition, at the first 20 cycles, the voltage characteristics and capacity fade by the side reaction are identical to those from the first case. However, since the discharging C-rate becomes much larger, the degradation caused by the mechanical stress becomes larger, which leads to different charging characteristics after 40 cycles. At 100 cycles, due to large degradation, especially at the cathode electrode, the terminal voltage decreases rapidly, and discharge time becomes less than 1 minute, and the capacity fade by the mechanical stress becomes almost zero.

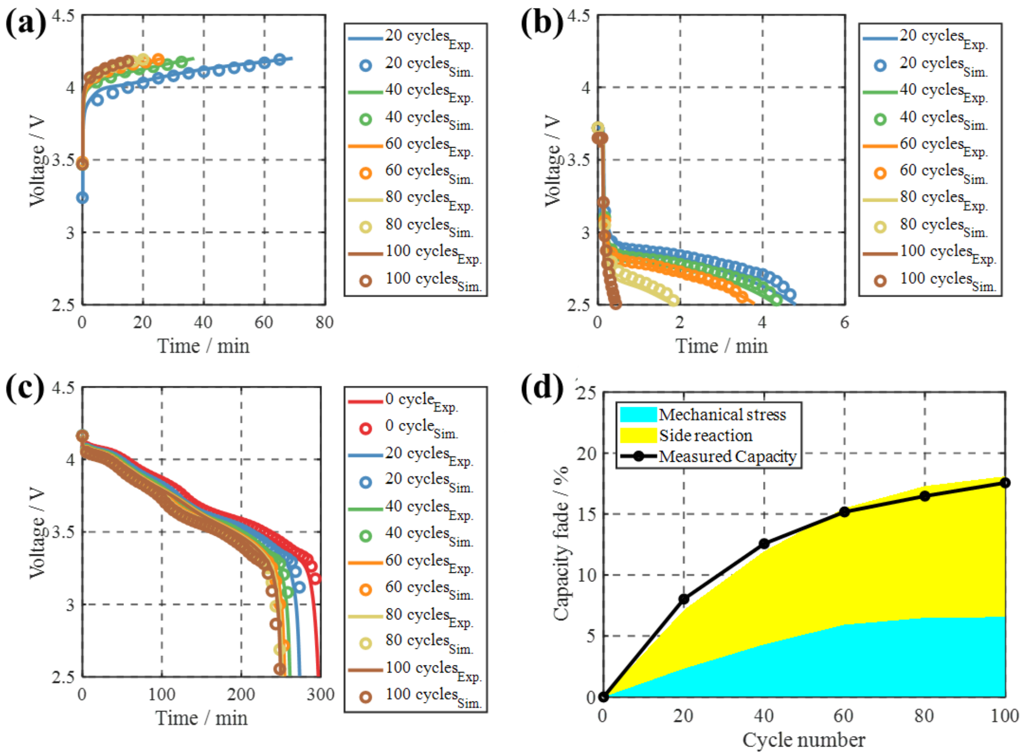

Figure 32. (a) Voltage characteristics under 0.25C CC charge at -10°C; (b) Voltage characteristics under 0.8C CC discharge at -10°C; (d) Voltage characteristics under 0.25C CC discharge at 25°C; and (d) Capacity fade by the model and experiment.

The results of case 3 (0.3C CC charge / 0.25C CC discharge) are plotted in Figure 33. In this case, due to the large C-rate for charging, the lithium plating takes place, and it becomes the most dominant degradation source. In addition, due to the same discharging condition as the first case, the voltage characteristics and capacity fade by the mechanical stress are identical to those from the first case at the first 20 cycles. However, due to the large chemical degradation, the discharge time becomes significantly reduced as the cycle proceeds, and the degradation by the mechanical stress is the smallest at the end of life.

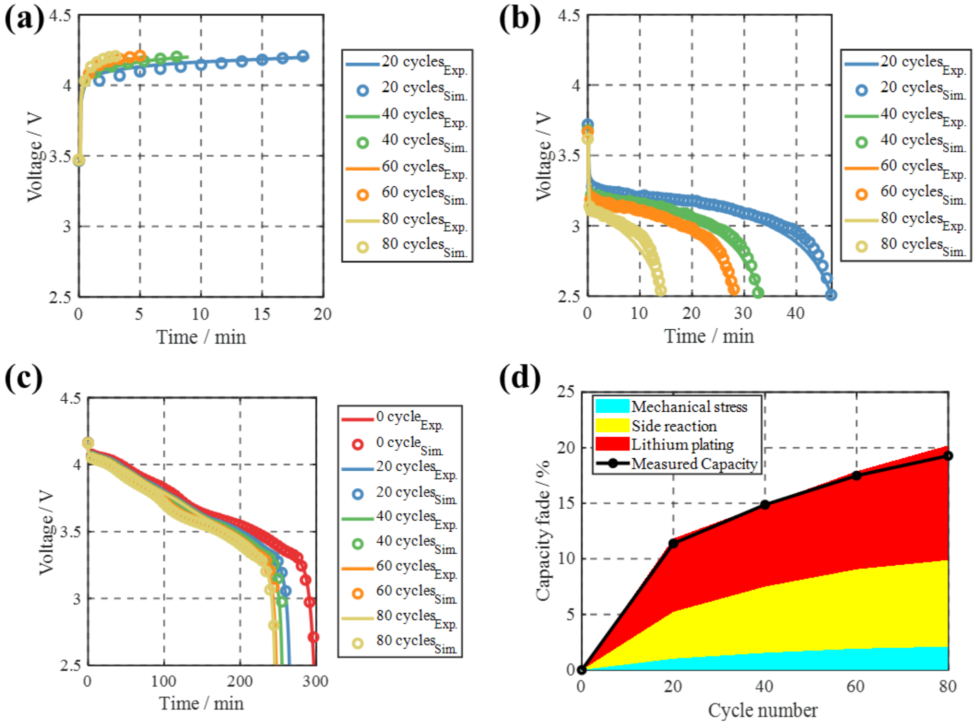

Figure 33. (a) Voltage characteristics under 0.3C CC charge at -10°C; (b) Voltage characteristics under 0.25C CC discharge at -10°C; (d) Voltage characteristics under 0.25C CC discharge at 25°C; and (d) Capacity fade by the model and experiment.

The capacity fade caused by each degradation source at different cases is compared in Figure 34 as a function of cycle numbers. The results have shown that due to the same charging current of case 1 and case 2, the amount of capacity fade by side reaction from the two cases are identical. However, since more degradation takes place at the cathode electrode from case 2 by the mechanical degradation, the amount of further side reaction from case 2 becomes smaller than that from case 1. On the other hand, in case 3, even though the charging C-rate is the largest, the capacity fade by the side reaction is less than the other two cases because of the short charging time. However, due to the lithium plating, the total capacity fade is the largest.

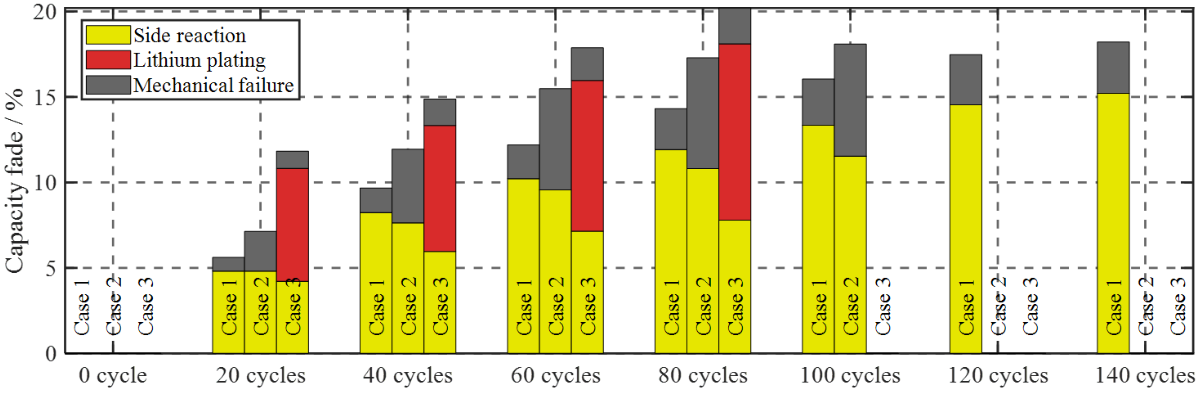

Figure 34. Capacity fade caused by each degradation source as a function of cycle numbers.

In addition, in order to compare the effect of temperature on the battery degradation, additional cycling tests at -10°C, -15°C, and -20°C are conducted under 0.25C CC/CV charging. The cycling results are summarized in Figure 35, where the current and voltage profiles are plotted in Figure 35 (a), and corresponding capacity fade by each temperature range is plotted in Figure 35 (b). The results have shown that as the temperature decreases, the overpotentials rapidly increase, which leads to a short CC charging period. Especially at -20°C, the CC charging finishes less than 1 minute, and the current rapidly decreases, and accordingly only 1/5 of capacity is charged at -20°C compared with that at -10°C. As a result, the lithium plating does not take place, and the effect of the mechanical stress also becomes smaller because of the short operating time. Therefore, the capacity fade at 10°C is the largest, as shown in Figure 35 (b).

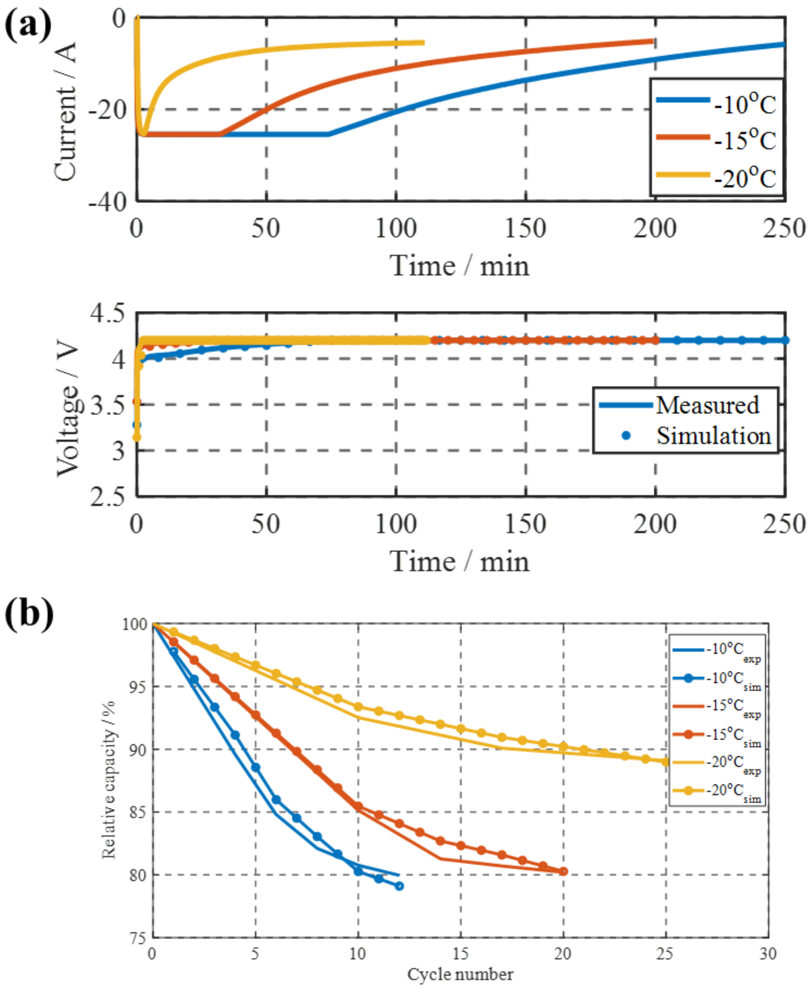

Figure 35. Cycling results at various subzero temperatures; (a) Current and voltage profiles; and (b) Capacity fade by measured by experiment and estimated by the model.

Even though the results have shown that the degradation is smaller at lower temperatures, the amount of charged capacity becomes significantly reduced. Therefore, an optimal charging algorithm needs to consider not only all degradation sources above but also a start-up strategy to increase the battery temperature so that more lithium ions can be stored in the anode electrode.

### 4.3 Design of optimal charging method considering degradation at subzero temperatures

In this chapter, based on the validated model, an optimal fast and safe charging methodconsidering an initial start-up strategy is developed that minimizes degradation. An objective function and constraints are derived from the internal variables given by the ROM, and a charging strategy is obtained by applying the nonlinear model predictive control (NMPC). In addition, the charging algorithm is combined with a method that maximizes heat generation rate, which is needed for the initial cold start-up.

The development procedure is divided into two steps. Firstly, the optimization of the charging profile is carried out by considering the degradation, where the objective function that should be minimized is the side reaction rate and the charging time, and the constraints are lithium plating overpotential and the terminal voltage. Two objective functions are traded-off by an optimal weighting factor obtained by the simulation results using the ROM. Thereafter, parameters for pulse profile are optimized by the GA that maximizes the total heat generation rate with a minimum discharging capacity, and the resulting pulse profile is combined with the charging profile.

#### 4.3.1 Optimal charging method considering side reaction and lithium plating

In this chapter, the charging profile is optimized using the NMPC based on the ROM. The NMPC is an iterative and finite optimization method, where an optimized state, the charging current, in this case, is calculated for a short time horizon in the future that is called a receding horizon. The main objective of the optimization is a reduction of charging time as well as degradation rate, and its function is expressed as follows;

$$J = \min_{I}\left[\alpha \cdot \int_{t=t_k}^{t_{k+N}} I dt + \beta \cdot \int_{x=0}^{\delta_-}\left\{\int_{t=t_k}^{t_{k+N}} j_{side}^{Li}\left(x,t\right)dt\right\} A dx\right] \tag{82}$$

, where *α* and *β* are the weighting factors determining the trade-off between the charging time and the degradation rate.

For example, *α=0* implies that the charging time is not considered for the optimization, and only the side reaction is considered, which will bring extremely slow charging speed. On the other hand, *β=0* implies the charging profile is aimed only at short charging time regardless of the amount of the side reaction, which causes a high rate of degradation. *k* and *N* represent a time step at a certain point and the receding horizon, respectively, where the receding horizon *N* is set as 10 considering calculation time. For the solver of the optimization control problem, Sequential Quadratic Programming (SQP) is applied because of its outstanding performance in robustness and constraint handling [43].

The first constraint considered is the lithium plating because of rapid increases of further reactions once taking place. The other constraint is the terminal voltage. They are expressed as follows;

$$\eta_{LiP} \le 0 \tag{83}$$

$$V_t \ge V_{t,cutoff} \tag{84}$$

Then, the optimal weighting factor was obtained by comparing the effects of the factor on the two objects. The results of the charging algorithm with different weighting factors, including current, voltage, and lithium plating overpotential, are plotted in Figure 36 (a), (b), and (c). The overall current profile is reduced as the ratio between *β* and *α* increases, which implies that the side reaction rate is more emphasized. However, even though the ratio becomes smaller, the current profile does not rapidly increase because of the lithium plating overpotential at low SOC and the terminal voltage at high SOC. As a result, the change of the current profile becomes minimum when the ratio is less than 700. The effect of the weighting factor on the side reaction and charging time is compared in Figure 36 (d), where no change is shown until the ratio becomes larger than 700. Above 700, the ion loss by the side reaction gets reduced as the ratio increases. However, the increase of the charging time is much larger than the reduction of the ion loss by the side reaction, and especially, the increase of the charging time becomes much larger as the SOC increases. Therefore, considering both the reduction of the side reaction and the increase of the charging time, the optimal weighting factors are set as $\beta/\alpha = 1000$.

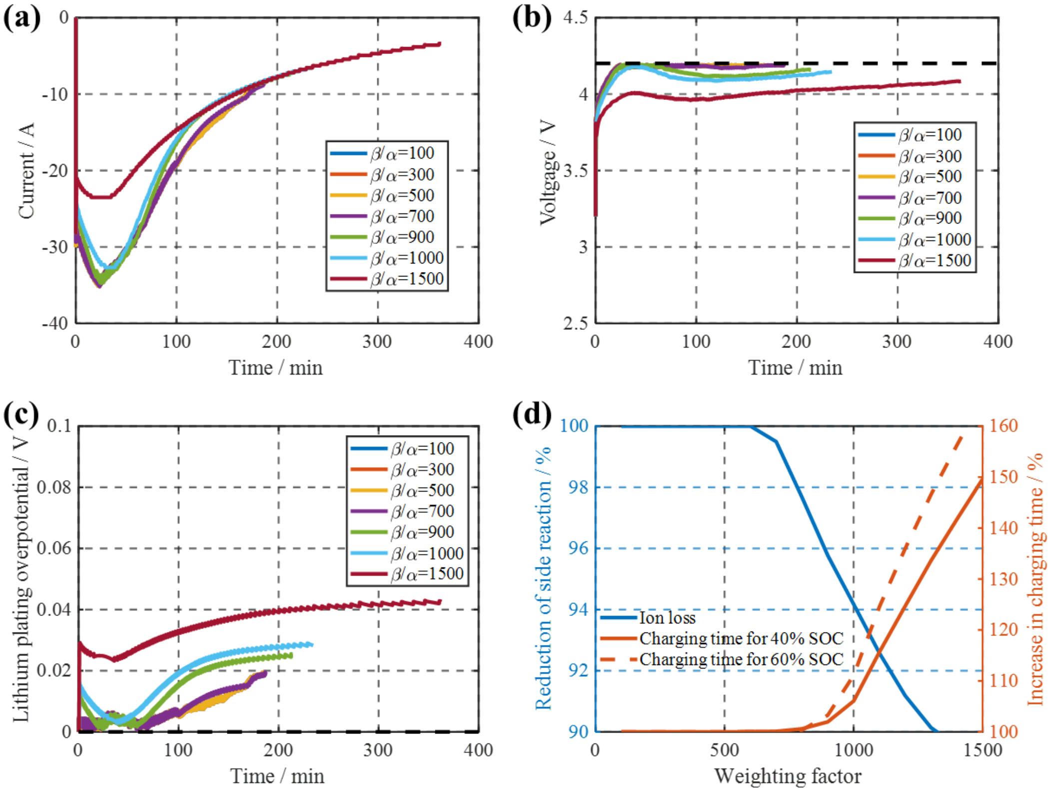

Figure 36. Simulation results of NMPC under different weighting factors; (a) Current profiles; (b) Voltage profiles; (c) Lithium plating overpotential profiles; (d) Comparison of reduction of side reaction and charging time as a function of the weighting factor.

### 4.3.2 Cold start charging profiles considering lithium stripping

Even with the optimization of the charging profile with respect to the lithium plating, there might be unexpected lithium plating, particularly at subzero temperature, due to the sluggish kinetics of charges. Accordingly, a start-up strategy at the beginning of the charging is important to minimize degradation, which can be accomplished by increasing the operating temperature from subzero temperature. This warming-up process is implemented by adding additional discharging pulses to the optimized charging profile to increase the heat generation rate and at the same time promote the lithium stripping.

The pulse profiles can be made of alternating current (AC), direct current (DC), or pulses combined as a function of frequency or duty cycle. Since a large RMS value of the DC is preferred for both high heat generation rate and lithium stripping, the DC pulse profile is selected, where the parameters for pulses are optimized, such as frequency, duty cycle, and the magnitude of the pulse. Since NMPC cannot optimize them with the charging profile simultaneously because of the limited receding horizon, the GA is used to optimize various parameters of the pulses.

The objective of the discharging pulse is to maximize the battery heat generation rate while the discharged capacity is being minimized. The objective function for this step is set by;

$$J = \min_{f,\gamma,I_{dis}} \left[ -\left( \alpha \cdot SOC\left(t_{end}\right) + \beta \cdot \int_0^{t_{end}} \dot{Q}_{total} dx \right) \right] \tag{85}$$

, where $f$, $\gamma$, *and* $I_{dis}$ are the frequency, duty cycle, and magnitude of the discharging pulse, respectively. Since there is another trade-off between discharging capacity and total heat generation, the weighting factor for this objective function $\alpha$ and $\beta$ are also considered. The constraints are the terminal voltage above the cutoff voltage and the maximum discharge current selected as 0.5C considering mechanical degradation during a high C-rate.

Firstly, the pulse profile is applied for 20 minutes, considering the total charging time and the overpotential of the lithium plating, and then becomes reduced by the charging profile from the NMPC, as shown in Figure 36. The results of the GA are summarized in Figure 37, where the increase of total heat generation and SOC after 20 minutes as a function of the weighting factor are compared. The dotted lines represent the results without applying pulse. The SOC after 20 minutes increases as the ratio of $\beta$ increases over $\alpha$, implying that more weight is placed on the total charging capacity. However, the increase of the total heat generation rate becomes minimum because of a small discharging pulse. On the other hand, as the ratio decreases, the total heat generation rate rapidly increases, while SOC decreases. As a result, $\beta/\alpha=30$ is selected as the optimal ratio considering high total heat generation and moderate decrease of SOC. Consequently, the optimized discharge pulse is combined with the NMPC charging method.

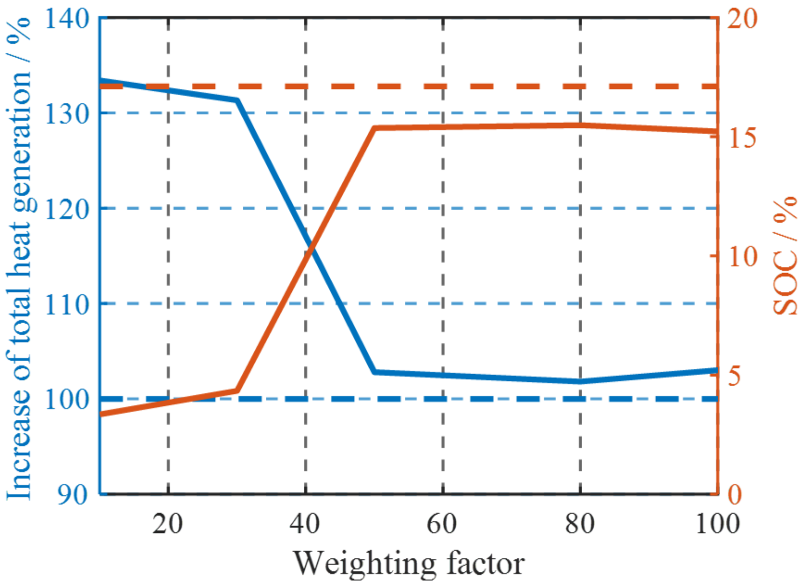

Figure 37. Comparison of increase of total heat generation and SOC after 20 minutes as a function of the weighting factor.

### 4.4 Experimental verification of the proposed charging algorithm

Based on the optimal charging algorithm with discharging pulses obtained by NMPC and GA, a battery is cycled at -10°C. In order to compare the effect of the charging algorithm, additional cycling tests under normal CC/CV charging are conducted at 0.25C and 0.3C. For all cycling tests, the batteries are charged until the current becomes smaller than the cutoff current that is C/20 and then discharged by 0.25C CC discharge. The results are summarized in Figure 38, where current and voltage profiles are compared in Figure 38 (a) and (b). The initial current of the proposed charging method is similar to the 0.25C. However, due to the negative pulses at the beginning of the charging, the battery temperature is increased, and accordingly, the maximum allowable current becomes larger. As a result, the charging current increases, and the battery can be charged faster. The battery temperature profiles during charging are plotted in Figure 38 (c). Due to discharging pulses at the beginning of the charging, the temperature of the battery charged by the proposed method increases faster than those by the other CC/CV charging methods, where the maximum temperature increase by the 0.3C CC/CV charging is smallest because of the short CC charging period. The charged capacity by each method for each method is compared and plotted in Figure 38 (d) to compare the charging speed, where the capacity is calculated by the Coulomb counting method. At the beginning of charging, the charging speed by 0.3C CC/CV is the fastest because of the largest charging current. However, because of the short CC charging period, the charging speed becomes slower. On the other hand, when the battery is charged by the proposed charging method, the charging speed at the beginning is slower by 0.3C. However, since the charging current becomes larger, the charging speed becomes faster after the middle of the charging. In addition, since the charging is finished when the current becomes smaller than C/20, the charging capacity by each method is different. For 0.25C CC/CV charging, because of the smallest CC charging current, the charged capacity is the smallest even though the total charging time is larger than that by 0.3C CC/CV charging. On the other hand, the charging capacity by the proposed charging method is the largest because of the high current, as well as the largest temperature rise. The charging time for 30Ah, 40Ah, and 50Ah capacity for each charging method is compared in Table 13. The proposed method is able to charge the battery 37%, 47.6% faster for

30Ah and 40Ah capacity than 0.25C CC/CV, respectively. Compared with 0.3C CC/CV, the charging time for 30Ah capacity is identical, but it becomes 6% and 13% faster to charge 40Ah and 50Ah capacity, respectively. Therefore, the proposed method has advantages of the capability of charging higher capacity, as well as fast charging speed.

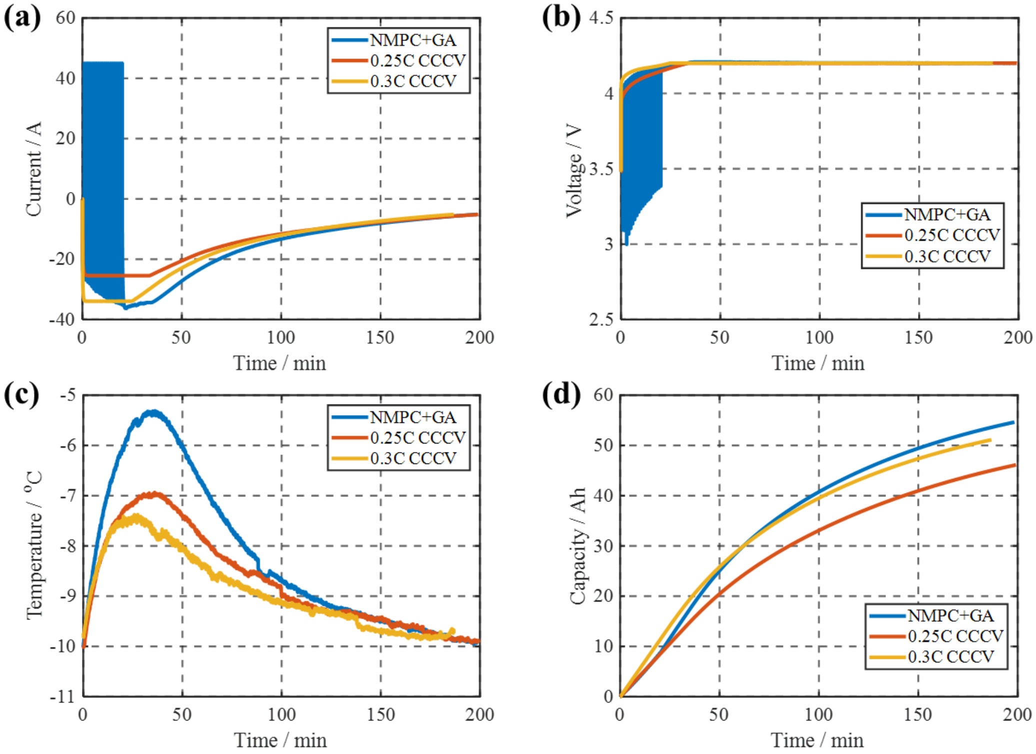

Figure 38. Results of charging by NMPC+GA, 0.25C, and 0.3C CC/CV charging; (a) Current profile; (b) Voltage profile; (c) Temperature profile; and (d) Charging capacity.

Table 13. Comparison of charging time for different capacities.

| | **30Ah** | **40Ah** | **50Ah** |
|---|---|---|---|
| 0.25C CC/CV (min) | 85.1 | 142.7 | - |

| | | | |
|---|---|---|---|
| 0.3C CC/CV (min) | 62.1 | 102.5 | 174.4 |
| NMPC + GA (min) | 62.0 | 96.7 | 154.5 |

Lastly, the capacity is measured after the cycling by each method. The capacity fade by three different charging methods is plotted in Figure 39. The results have shown that the capacity fade by the 0.3C CC/CV charging method is the largest because of a large amount of side reaction and lithium plating, as shown in Figure 33. On the other hand, since the current is optimized to reduce the side reaction rate and prohibit the lithium plating, in addition to the negative pulses, even though the charging speed by the proposed method is the fastest, the degradation rate is not the largest and comparable to that by the 0.25C CC/CV charging. Therefore, the proposed charging method is the optimal charging algorithm that can charge the battery with a reduced degradation rate as well as fast charging time.

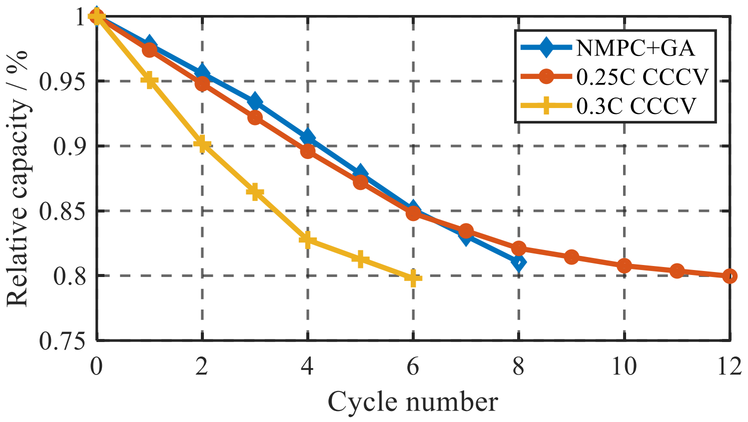

Figure 39. Comparison of capacity fade by NMPC+GA, 0.25C, and 0.3C CC/CV charging.

## 4.5 Summary

In this section, a new fast and safe charging method considering the degradation as well as the effect of temperature is designed at subzero temperature. Firstly, the degradation model is extended considering subzero temperature, where a mechanical model for the ROM is developed and experimentally validated. Further analysis has revealed that a steep ion concentration gradient can lead to an accumulation of the strain energy, which leads to mechanical degradation, and the capacity and the volume fraction of the cathode electrode are reduced due to cracks and fractures. Based on the model, an optimal charging algorithm is designed, where a nonlinear model predictive control method is applied with the objective function of minimization of charging time and the degradation caused by the side reaction. For the constraints, the lithium plating overpotential and the cutoff voltage are considered. In addition, in order to promote lithium stripping and maximize the heat generation rate, the discharging pulse profiles are applied at the beginning of the charging as a start-up strategy, where the pulse parameters are optimized by the genetic algorithm. Finally, an optimal charging algorithm at subzero temperature is designed by combining the charging algorithm with the pulse profile. The proposed charging algorithm is experimentally verified by comparing the results with the normal CC/CV charging methods. The results have shown that the proposed method is able to charge the largest capacity compared with 0.25C CC/CV and 0.3C CC/CV. In addition, the charging time by the proposed algorithm is 37% and 47.6% faster for 30Ah and 40Ah capacity than that by 0.25C CC/CV, respectively. Compared with 0.3C CC/CV, the charging time for 30Ah capacity is identical, but it becomes 6% and 13% faster to charge 40Ah and 50Ah capacity, respectively. In addition, the capacity fade by the proposed method is identical to that by 0.25C CC/CV. Therefore, the proposed method has advantages of the capability of charging higher capacity with fast charging speed, as well as less degradation rate.

# Chapter 5. Conclusion

## 5.1 Conclusion

This dissertation comprehensively studied and analyzed the characteristics of the lithium-ion battery under various environments using a reduced-order electrochemical-thermal life model that has been experimentally validated. Based on the model, charging algorithms for lithium-ion batteries operating at considering a wide range of temperatures are proposed. In this work, we:

- Developed a chemical degradation model by considering the side reaction, lithium plating, and lithium stripping. The model is further validated by various cycling profiles, where the model is able to accurately estimate the linear and nonlinear capacity fades. In addition, the effect of negative pulse on battery degradation is experimentally verified. Lastly, based on the model, a fast and safe charging algorithm considering side reaction and lithium plating at room temperatures is developed, where the negative pulse currents are applied to promote the lithium stripping. The proposed charging algorithm is compared with normal charging methods, which has shown that the charging time by the proposed algorithm is approximately 50% less than that by 2C CC/CV for the interval from 0% to 40% SOC and 43% for the interval 0% to 60% SOC, while 31% and 18% less than that by 3C CC/CV, respectively. In addition, the capacity loss by the proposed algorithm is comparable to that by 2C CC/CV, which is approximately 23% less than that by 3C CC/CV after 60 cycles

- Developed a reduced-order electrochemical-thermal model considering the internal processes of the battery. The model is validated with respect to the measured heat generation rate from -30°C to 45°C. Based on the validated model, a detailed analysis of the heat source terms is conducted, including the effect of current and temperatures on each heat source term. With the thermal model capable of estimating the heat generation rate at each component, the model is extended to one dimensional model for a single cell considering each component and thermal contact resistance. In addition, a detailed sensitivity analysis of design parameters with respect to the battery heat generation rate is conducted. The results have shown that the parameters affect different heat source terms and their sensitive SOC regions are different. Accordingly, the parameters are clustered into three groups, and a new parameter identification method is proposed based on the three-stage identification that only requires 20% of the SOC range for each stage. In addition, due to the reduced number of parameters for each stage, the searching space becomes smaller, which helps to find the optimal solution. The model with identified parameters are further validated with respect to temperature profiles, which has shown that the model is able to estimate the temperature with a maximum error of 0.2°C

- Further extended the degradation model by considering mechanical degradation. The degradation model is validated at -10°C considering both chemical and mechanical degradation, which has shown that a steep concentration gradient during discharge can lead to mechanical stress-induced degradation. Accordingly, a charging algorithm, as well as a start-up strategy, is designed based on the model, where the nonlinear model predictive control is used to design the charging profile, and the genetic algorithm is used to find the optimal pulse profile for start-up strategy. The proposed charging algorithm is compared with normal charging methods, which has shown that the charging time by the proposed algorithm is 47.6% faster than that by 0.25C CC/CV and 6% faster than that by 0.3C CC/CV. In addition, due to the increased heat generation rate, the battery can be charged more capacity by the proposed algorithm while maintaining comparable degradation speed.

## 5.2 Future work

The current charging algorithm is generated by using MPC or GA. The current limitation of the methods is the required trade-off between objective functions. In addition, even though the MPC can be applied in real-time applications, the receding horizontal should be short enough to ensure fast calculation. Since the overall performance of the MPC could be affected by the receding horizon as well, there is a need for the optimization of the method considering moderate calculation time and optimal solution.

# Reference

[1] Y. Hua, X. Liu, S. Zhou, Y. Huang, H. Ling, and S. Yang, “Toward Sustainable Reuse of Retired Lithium-ion Batteries from Electric Vehicles.” *Resources, Conservation and Recycling* 105249, 2020.

[2] M. Pagliaro, F. Meneguzzo, “Lithium battery reusing and recycling: a circular economy insight.” *Heliyon* 5 e1866, 2019.

[3] K. Ando, T. Matsuda, and D. Imamura. “Degradation diagnosis of lithium-ion batteries with a LiNi0. 5Co0. 2Mn0. 3O2 and LiMn2O4 blended cathode using dV/dQ curve analysis.” *Journal of Power Sources* 390: 278-285, 2018.

[4] X.G. Yang, Y. Leng, G. Zhang, S. Ge, C.Y. Wang, “Modeling of lithium plating induced aging of lithium-ion batteries: transition from linear to nonlinear aging.” *Journal of Power Sources* 360, 28-40, 2017.

[5] H. Ekstrom and G. Lindbergh, “A model for predicting capacity fade due to SEI formation in a commercial graphite/LiFePO4 cell.” *Journal of The Electrochemical Society* 162, no. 6: A1003. 2015.

[6] P. Arora, R.E. White, and M. Doyle, “Capacity fade mechanisms and side reactions in lithium-ion batteries.” *Journal of the Electrochemical Society*, 145(10), p.3647.1998.

[7] B. Wu and W. Lu, “A battery model that fully couples mechanics and electro- chemistry at both particle and electrode levels by incorporation of particle interaction.” *Journal of Power Sources,* 360, 360-372. 2017.

[8] B. Wu and W. Lu, “Mechanical-electrochemical modeling of agglomerate particles in lithium-ion battery electrodes.” *Journal of The Electrochemical Society,* 163(14), A3131, 2016.

[9] S. Wang, K. Rafiz, J. Liu, Y. Jin, and J.Y.S. Lin,:Effects of lithium dendrites on thermal runaway and gassing of LiFePO 4 batteries.” *Sustainable Energy & Fuels*, 4(5), 2342-2351, 2020.

[10] A. Jana, G.M. Shaver, and R.E. García, “Physical, on the fly, capacity degradation prediction of LiNiMnCoO2 -graphite cells. *Journal of Power Sources,* 422, 185-195, 2019.

[11] S. Zhang, “The effect of the charging algorithm on the cycle life of a Li-ion battery.” *Journal of power sources* 161.2, 1385-1391, 2006.

[12] A. J. Salkind, C. Fennie, P. Singh, T. Atwater, and D. E. Reisner. “Determination of state-of-charge and state-of-health of batteries by fuzzy logic methodology.” *Journal of Power sources*. Jul 1;80(1-2):293-300, 1999

[13] C. Mohammad, and F. Mohammad. “State-of-charge estimation for lithium-ion batteries using neural networks and EKF.” *IEEE transactions on industrial electronics* 57.12: 4178-4187, 2010.

[14] Y. Yin, Y. Hu, S.Y. Choe, H. Cho, and W.T. Joe "New fast charging method of lithium-ion batteries based on a reduced order electrochemical model considering side reaction." *Journal of Power Sources* 423: 367-379, 2019.

[15] P. Verma, P. Maire and P. Novák. "A review of the features and analyses of the solid electrolyte interphase in Li-ion batteries." *Electrochimica Acta* 55, Vol. 22, pp. 6332-6341, 2010.

[16] A, Victor, and J. Fergus. "Lithium-ion battery anode aging mechanisms." *Materials* 6.4: 1310-1325, 2013.

[17] M. Alipour, C. Ziebert, F.V. Conte, and R. Kizilel, "A Review on Temperature-Dependent Electrochemical Properties, Aging, and Performance of Lithium-Ion Cells.", *Batteries,* 6.3:35, 2020.

[18] E. Antolini, "LiCoO2: Formation, structure, lithium and oxygen nonstoichiometry, electrochemical behaviour and transport properties." *Solid State Ionics*, 170, 159–171, 2004.

[19] D. Goers, M.E. Spahr, A. Leone, W Märkle, and P. Novák, "The influence of the local current density on the electrochemical exfoliation of graphite in lithium-ion battery negative electrodes." *Electrochimica Acta*, 56, 3799–3808, 2011.

[20] M. Broussely, S. Herreyre, P. Biensan, P. Kasztejna, K. Nechev, and R.J. Staniewicz,"Aging mechanism in Li ion cells and calendar life predictions." *Journal of Power Sources*, 98, 13–21, 2001.

[21] A. Wang, S. Kadam, H. Li, S. Shi, and Y. Qi, "Review on modeling of the anode solid electrolyte interphase (SEI) for lithium-ion batteries." *npj Computational Materials*, 4(1), 1-26, 2018.

[22] M. Endo, C. Kim, K. Nishimura, T. Fujino, and K. Miyashita. "Recent development of carbon materials for Li ion batteries." *Carbon* 38, no. 2, 2000.

[23] B. Scrosati and J. Garche "Lithium batteries: status, prospects and future." *Journal of Power Sources,* 195(9), 2419-2430, 2010.

[24] T.F. Yi, L.J. Jiang, J. Shu, C.B. Yue, R.S. Zhu, and H.B. Qiao, "Recent development and application of Li4Ti5O12 as anode material of lithium-ion battery." *Journal of Physics and Chemistry of Solids*, 71(9), 1236-1242, 2010.

[25] D. Zhang, B.S. Haran, A. Durairajan, R.E. White, Y. Podrazhansky, and B.N. Popov, "Studies on capacity fade of lithium-ion batteries." *Journal of Power Sources,* 91(2), 122-129. 2000.

[26] S. Watanabe, M. Kinoshita, T. Hosokawa, K. Morigaki, and K. Nakura, "Capacity fade of LiAlyNi1-x-yCoxO2 cathode for lithium-ion batteries during accelerated calendar and cycle life tests (surface analysis of LiAlyNi1-x-yCoxO2 cathode after cycle tests in restricted depth of discharge ranges)." *Journal of Power Sources*, 258, 210-217, 2014.

[27] Y.K. Sun, Z. Chen, H.J. Noh, D.J. Lee, H.G. Jung, Y. Ren, S. Wang, C.S. Yoon, S.T. Myung, and K. Amine, "Nanostructured high-energy cathode materials for advanced lithium batteries." *Nature materials*, 11, 942-947, 2012.

[28] H.J. Noh, S. Youn, C.S. Yoon, Y.K. Sun "Comparison of the structural and electro- chemical properties of layered Li[NixCoyMnz]O2 (x ¼ 1/3, 0.5, 0.6, 0.7, 0.8 and 0.85) cathode material for lithium-ion batteries." *Journal of Power Sources*, 233, 121-130, 2013.

[29] N.Y. Kim, T. Yim, J.H. Song, J.S. Yu, and Z. Lee, "Microstructural study on degradation mechanism of layered LiNi0. 6Co0. 2Mn0. 2O2 cathode materials by analytical transmission electron microscopy." *Journal of power sources*, 307, 641-648, 2016.

[30] G. Sun, T. Sui, B. Song, H. Zheng, L. Lu, and A. M. Korsunsky, "On the fragmentation of active material secondary particles in lithium-ion battery cathodes induced by charge cycling." *Extreme Mechanics Letters*, 9, 449-458, 2016.

[31] R. Xu, L. S. Vasconcelos, J. Shi, J. Li, and K. Zhao, "Mechanical and structural degradation of LiNixMnyCozO2 cathode in Li-ion batteries: an experimental study." *Journal of The Electrochemical Society*, 164(13), A3333, 2017.

[32] D.D. MacNeil, D. Larcher, J.R. Dah "Comparison of the reactivity of various carbon electrode materials with electrolyte at elevated temperature." *Journal of The Electrochemical Society*, 146, 3596, 1999.

[33] C. Yuqin, L. Hong, W. Lie, and L. Tianhong, "Irreversible capacity loss of graphite electrode in lithium-ion batteries." *Journal of power sources,* 68, 187–190, 1997.

[34] J. Shim and K.A. Striebel, "The dependence of natural graphite anode performance on electrode density." *Journal of Power Sources*, 130, 247–253, 2004.

[35] D. Aurbach, M. D. Levi, E. Levi, and A. Schechter, "Failure and stabilization mechanisms of graphite electrodes." *The Journal of Physical Chemistry B* 101, no. 12: 2195-2206, 1997.

[36] P. Arora, M. Doyle, and R.E. White. "Mathematical Modeling of the Lithium Deposition Overcharge Reaction in Lithium - Ion Batteries Using Carbon - Based Negative Electrodes." *Journal of The Electrochemical Society*, 146(10), 3543-3553, 1999.

[37] S.F. Schuster, T. Bach, E. Fleder, J. Müller, M. Brand, G. Sextl, and A. Jossen. "Nonlinear aging characteristics of lithium-ion cells under different operational conditions." journal of Energy Storage, 1, 44-53, 2015.

[38] C.R. Birkl, M.R. Roberts, E. McTurk, and P.G. Bruce. "Degradation diagnostics for lithium ion cells." *Journal of Power Sources* 341: 373-386, 2017.

[39] J. Li, E. Murphy, J. Winnick, and P.A. Kohl. "The effects of pulse charging on cycling characteristics of commercial lithium-ion batteries." *Journal of Power Sources* 102.1-2: 302-309, 2001.

[40] K.A. Smith, C.D Rahn, and C.Y. Wang. "Control oriented 1D electrochemical model of lithium-ion battery." *Energy Conversion and Management*, 48(9), 2565-2578, 2007.

[41] H.P. Lin, D. Chua, M. Salomon, H.C. Shiao, M. Hendrickson, E. Plichta, and S. Slane. “Low-temperature behavior of Li-ion cells.” *Electrochemical and Solid-State Letters* 4.6: A71-A73, 2001.

[42] J. Li, E. Murphy, J. Winnick, and P.A. Kohl. “The effects of pulse charging on cycling characteristics of commercial lithium-ion batteries.” *Journal of Power Sources* 102.1-2: 302-309, 2001.

[43] Z. Xinchen, Y.L. Yin, Y. Hu, and S.Y. Choe “Electrochemical-thermal modeling of lithium plating/stripping of Li (Ni0. 6Mn0. 2Co0. 2) O2/Carbon lithium-ion batteries at subzero ambient temperatures.” *Journal of Power Sources* 418: 61-73, 2019.

[44] M.A. Monem, K. Trad, N. Omar, O. Hegazy, B. Mantels, G. Mulder. “Lithium-ion batteries: Evaluation study of different charging methodologies based on aging process.” *Applied Energy* 152: 143-155, 2015.

[45] A. Hales, L.B. Diaz, M.W. Marzook, Y. Zhao, Y. Patel, and G. Offer, “The cell cooling coefficient: a standard to define heat rejection from lithium-ion batteries.” *Journal of The Electrochemical Society*, 166(12), A2383, 2019.

[46] K. Kumaresan, G. Sikha, and R.E. White, “Thermal model for a Li-ion cell.” *Journal of the Electrochemical Society*, 155(2), A164, 2007.

[47] W.B. Gu and C.Y. Wang, “Thermal-electrochemical modeling of battery systems.” *Journal of The Electrochemical Society*, 147(8), 2910, 2000.

[48] W. Van Schalkwijk, B. Scrosati, “Advances in lithium ion batteries introduction.” *Advances in lithium-ion batteries*. (pp. 1-5). Springer, Boston, MA, 2002.

[49] Y. Ye, L.H. Saw, Y. Shi, K. Somasundaram, and A. A. Tay, “Effect of thermal contact resistances on fast charging of large format lithium ion batteries.” *Electrochimica Acta*, 134, 327-337, 2014.

[50] K.E. Thomas, and J. Newman, “Heats of mixing and of entropy in porous insertion electrodes.” *Journal of power sources*, 119, 844-849, 2003.

[51] X. Zhang, A.M. Sastry, and W. Shyy, “Intercalation-induced stress and heat generation within single lithium-ion battery cathode particles.” *Journal of The Electrochemical Society*, 155(7), A542, 2008.

[52] K.E. Thomas, C. Bogatu, and J. Newman, “Measurement of the entropy of reaction as a function of state of charge in doped and undoped lithium manganese oxide.” *Journal of the Electrochemical Society*, 148(6), A570, 2001.

[53] D. Bernardi, E. Pawlikowski, and J. Newman, “A general energy balance for battery systems.” *Journal of the electrochemical society*, 132(1), 5, 1985.

[54] W. Lu and J. Prakash, “In situ measurements of heat generation in a Li/mesocarbon microbead half-cell. Journal of the Electrochemical Society, 150(3), A262, 2003.

[55] J.S. Hong, H. Maleki, S. AI Hallaj, L. Redey, J.R. Selman, “Electrochemical ‐ calorimetric studies of lithium ‐ ion cells.” *Journal of the Electrochemical Society*, 145(5), 1489, 1998

[56] S. Al Hallaj, R. Venkatachalapathy, J. Prakash, J.R. Selman, “Entropy changes due to structural transformation in the graphite anode and phase change of the LiCoO2 cathode.” *Journal of the Electrochemical Society*, 147(7), 2432, 2000.

[57] A. Eddahech, O. Briat, and J.M. Vinassa, “Thermal characterization of a high-power lithium-ion battery: Potentiometric and calorimetric measurement of entropy changes. Energy, 61, 432-439, 2013.

[58] M. Xiao and S. Y. Choe, “Theoretical and experimental analysis of heat generations of a pouch-type LiMn2O4/carbon high power Li-polymer battery.” *Journal of power sources*, 241, 46-55, 2013.

[59] S.S. Zhang, K. Xu, and T. R. Jow, “Electrochemical impedance study on the low temperature of Li-ion batteries.” *Electrochimica Acta*, 49(7), 1057-1061, 2004.

[60] G. Liu, M. Ouyang, L. Lu, J. Li, X. Han, “Analysis of the heat generation of lithium-ion battery during charging and discharging considering different influencing factors.” *Journal of Thermal Analysis and Calorimetry*, 116(2), 1001-1010, 2014.

[61] S. Gross, “Heat generation in sealed batteries.” *Energy Conversion*, 9(2), 55-62, 1969.

[62] E. Yoshida and T. Furukawa, “Nuclear Corrosion Science and Engineering.” *Elsevier*, 773-806, (2012).

[63] V. Vishwakarma, C. Waghela, Z. Wei, R. Prasher, S. C. Nagpure, J. Li, F. Liu, C. Daniel, and A. Jain, “Heat transfer enhancement in a lithium-ion cell through improved material-level thermal transport.” *Journal of Power Sources* 300, 123-131, 2015.

[64] S.D. Lubner, S. Kaur, Y. Fu, V. Battaglia, and R.S. Prasher, “Identification and characterization of the dominant thermal resistance in lithium-ion batteries using operando 3-omega sensors.” *Journal of Applied Physics*, 127(10), 105104, 2020.

[65] D.J. Pereira M.A. Fernandez, K.C. Streng, X.X. Hou, X. Gao, J.W Weidner, and T.R. Garrick “Accounting for Non-Ideal, Lithiation-Based Active Material Volume Change in Mechano-Electrochemical Pouch Cell Simulation. Journal of The Electrochemical Society, 167(8), 080515, 2020.

[66] C. Huber. “Phase Change Material in Battery Thermal Management Applications.” PhD diss., Technische Universität München (2017).

[67] A.A. Pesaran, “Battery thermal management in EV and HEVs: issues and solutions.” *Battery Man*, 43(5), 34-49, 2001.

[68] L. Zhang, C. Lyu, G. Hinds, L. Wang, W. Luo, J. Zheng, and K. Ma, “Parameter sensitivity analysis of cylindrical LiFePO4 battery performance using multi-physics modeling.” *Journal of The Electrochemical Society*. 161(5): A762, 20014.

[69] M. Ecker, T.K. Tran, P. Dechent, S. Käbitz, A. Warnecke, and D.U. Sauer, “Parameterisation of a Physico-Chemical Model of a Lithium-Ion Battery Part I: Determination of Parameters.” *Journal of The Electrochemical Society* 162(9): A1836-48, 2015.

[70] J. Schmalstieg, C. Rahe, M. Ecker, and D.U. Sauer. “Full cell parameterization of a high-power lithium-ion battery for a physico-chemical model: Part I. Physical and electrochemical parameters.” *Journal of The Electrochemical Society* 165(16): A3799, 2016.

[71] S. Tang, Z. Wang, H. Guo, J. Wang, X. Li, and G. Yan, “Systematic parameter acquisition method for electrochemical model of 4.35 V LiCoO2 batteries.” *Solid State Ionics* 343:115083, 2019.

[72] M. Ecker, S. Käbitz, I. Laresgoiti, and D.U. Sauer DU. “Parameterization of a physico-chemical model of a lithium-ion battery: II. Model validation.” *Journal of The Electrochemical Society* 162(9):A1849, 2015.

[73] A.P. Schmidt, M. Bitzer, ÁW. Imre, and L. Guzzella, “Experiment-driven electrochemical modeling and systematic parameterization for a lithium-ion battery cell.” *Journal of Power Sources*, 195(15):5071-80, 2010.

[74] J.C. Forman, S.J. Moura, J.L. Stein, and H.K. Fathy, “Genetic identification and fisher identifiability analysis of the Doyle–Fuller–Newman model from experimental cycling of a LiFePO4 cell.” *Journal of Power Sources* 210:263-75, 2012.

[75] S. Park, D. Kato, Z. Gima, R. Klein, and S. Moura, “Optimal experimental design for parameterization of an electrochemical lithium-ion battery model.” *Journal of The Electrochemical Society* 165(7): A1309, 2018.

[76] X. Lai, S. Wang, S. Ma, J. Xie, and Y. Zheng, “Parameter sensitivity analysis and simplification of equivalent circuit model for the state of charge of lithium-ion batteries.” *Electrochimica Acta* 330:135239, 2020.

[77] W. Li, D. Cao, D. Jöst, F. Ringbeck, M. Kuipers, F. Frie, and D.U. Sauer, “Parameter sensitivity analysis of electrochemical model-based battery management systems for lithium-ion batteries.” *Applied Energy* 269:115104, 2020.

[78] N. Lin, X. Xie, R. Schenkendorf, and U. Krewer. “Efficient global sensitivity analysis of 3D multiphysics model for Li-ion batteries.” *Journal of The Electrochemical Society* 165(7): A1169, 2018.

[79] F. Guo, G. Hu, P. Zhou, T. Huang, X. Chen, M. Ye, and J. He, “The equivalent circuit battery model parameter sensitivity analysis for lithium-ion batteries by Monte Carlo simulation.” *International Journal of Energy Research* (15):9013-24, 2019.

[80] W. Tang and M. Jia, "Global sensitivity analysis of a large agent-based model of spatial opinion exchange: A heterogeneous multi-GPU acceleration approach." *Annals of the Association of American Geographers* 104(3): 485-509, 2014.

[81] C. Edouard, M. Petit, J. Bernard, C. Forgez, and R. Revel. "Sensitivity Analysis of an Electrochemical Model of Li-ion Batteries and Consequences on the Modeled Aging Mechanisms." *ECS Transactions* 66(9):37, 2015.

[82] C. Edouard, M. Petit, C. Forgez, J. Bernard, and R. Revel. "Parameter sensitivity analysis of a simplified electrochemical and thermal model for Li-ion batteries aging." *Journal of Power Sources* 325:482-94, 2016.

[83] D. Danilov and P.H. Notten, "Mathematical modelling of ionic transport in the electrolyte of Li-ion batteries." *Electrochimica Acta* 53(17):5569-78, 2008.

[84] B. Suthar, P.W. Northrop, D. Rife, and V.R. Subramanian, "Effect of porosity, thickness and tortuosity on capacity fade of anode." *Journal of The Electrochemical Society* 162(9): A1708, 2015.

[85] Y. Bi and S.Y. Choe, "Automatic Estimation of Parameters of a Reduced Order Electrochemical Model for Lithium-Ion Batteries at the Beginning-of-Life." *IEEE Vehicle Power and Propulsion Conference (VPPC)* (pp. 1-6). IEEE, 2018.

[86] P.R. Nileshwar, A. McGordon, T.R. Ashwin, and D. Greenwood, "Parametric Optimization Study of a Lithium-ion Cell." *Energy Procedia* 138:829-34, 2017.

[87] S.V. Erhard, P.J. Osswald, P. Keil, E. Höffer, M. Haug, A. Noel, J. Wilhelm, B. Rieger, K. Schmidt, S. Kosch, and F.M. Kindermann, "Simulation and measurement of the current density distribution in lithium-ion batteries by a multi-tab cell approach." Journal of The Electrochemical Society 164(1): A6324, 2017.

[88] S. Panchal, M. Mathew, R. Fraser, and M. Fowler, "Electrochemical thermal modeling and experimental measurements of 18650 cylindrical lithium-ion battery during discharge cycle for an EV." *Applied Thermal Engineering* 135:123-32, 2018.

[89] A. Rheinfeld, J. Sturm, A. Noel, J. Wilhelm, A. Kriston, A. Pfrang, and A. Jossen. "Quasi-Isothermal External Short Circuit Tests Applied to Lithium-Ion Cells: Part II. Modeling and Simulation." Journal of The Electrochemical Society 166(2): A151, 2019.

[90] S.G. Stewart, V. Srinivasan, and J. Newman, "Modeling the performance of lithium-ion batteries and capacitors during hybrid-electric-vehicle operation." *Journal of The Electrochemical Society* 155(9): A664, 2008.

[91] W. Fang, O.J. Kwon, and C.Y. Wang, "Electrochemical–thermal modeling of automotive Li-ion batteries and experimental validation using a three-electrode cell." International journal of energy research 34(2):107-15, 2010.

[92] Y. Ji, Y. Zhang, and C.Y. Wang, "Li-ion cell operation at low temperatures." *Journal of The Electrochemical Society* 160(4): A636, 2013.

[93] J. Smekens, J. Paulsen, W. Yang, N. Omar, J. Deconinck, A. Hubin, and J. Van Mierlo, "A Modified Multiphysics model for Lithium-Ion batteries with a LixNi1/3Mn1/3Co1/3O2 electrode." *Electrochimica Acta* 174:615-24, 2015.

[94] K.H. Kwon, C.B. Shin, T.H. Kang, and C.S. Kim. "A two-dimensional modeling of a lithium-polymer battery." *Journal of Power Sources* 163(1):151-7, 2006.

[95] R. Fu, X. Xiao, and S.Y. Choe, "Modeling, validation and analysis of mechanical stress generation and dimension changes of a pouch-type high power Li-ion battery." Journal of Power Sources 224:211-24, 2013.

[96] A. Awarke, S. Pischinger, and J. Ogrzewalla, "Pseudo 3D modeling and analysis of the SEI growth distribution in large format Li-ion polymer pouch cells." Journal of the Electrochemical Society 160(1): A172, 2012.

[97] Y. Zhao "A highly efficient reduced order model considering aging effects for lithium ion polymer batteries." [dissertation]. Auburn University; 2017.

[98] Y. Bi "Online State and Parameter Estimation for Lithium-ion Batteries Based on a Reduced-order Electrochemical Life Model." [dissertation]. Auburn University; 2020.

[99] C. Capiglia, Y. Saito, H. Kageyama, P. Mustarelli, T. Iwamoto, T. Tabuchi, and H. Tukamoto, "7Li and 19F diffusion coefficients and thermal properties of non-aqueous electrolyte solutions for rechargeable lithium batteries." *Journal of power sources* 81:859-62, 1999.

[100] Y. Bi and S.Y. Choe, "An adaptive sigma-point Kalman filter with state equality constraints for online state-of-charge estimation of a Li (NiMnCo) O2/Carbon battery using a reduced-order electrochemical model." *Applied Energy* 258:113925, 2020.

[101] Y. Hu, Y. Yin, and S.Y. Choe, "Accelerated equilibration for lithium-ion battery using optimal time control with electrochemical model." *Journal of Power Sources* 480:228623, 2020.

[102] R. Fu, M. Xiao, and S. Y. Choe, "Modeling, validation and analysis of mechanical stress generation and dimension changes of a pouch type high power Li-ion battery," *Journal Power Sources*, vol. 224, pp. 211–224, 2013.

[103] S. Kalnaus, K. Rhodes, and C. Daniel, "A study of lithium ion intercalation induced fracture of silicon particles used as anode material in Li-ion battery." *Journal Power Sources* 196(19), 8116-8124, 2011.

[104] S.C. Yang, Y. Hua, D. Qiao, Y.B. Lian, Y.W. Pan, and Y.L. He. "A coupled electrochemical-thermal-mechanical degradation modelling approach for lifetime assessment of lithium-ion batteries." *Electrochimica Acta* 326:134928, 2019.

[105] X.H. Liu, J.W. Wang, S. Huang, F. Fan, X. Huang, Y. Liu, S. Krylyuk, J. Yoo, S.A. Dayeh, A.V. Davydov, and S.X. Mao, “In situ atomic-scale imaging of electrochemical lithiation in silicon.” *Nature Nanotechnology* 7, 749–756, 2012.

[106] S. Xie, X. Hu, S. Qi, and K. Lang, “An artificial neural network-enhanced energy management strategy for plug-in hybrid electric vehicles,” *Energy*, vol. 163, 837–848, 2018.